



| | |
|------------------|---|
| Title | Study on Oxygen Separation Membrane based on Mixed Oxide Ionic-Electronic Conductor |
| Author(s) | 石井, 健斗 |
| Citation | 北海道大学. 博士(工学) 甲第14014号 |
| Issue Date | 2020-03-25 |
| DOI | 10.14943/doctoral.k14014 |
| Doc URL | http://hdl.handle.net/2115/78154 |
| Type | theses (doctoral) |
| File Information | Kento_ISHII.pdf |



[Instructions for use](#)

Doctoral Thesis



Study on Oxygen Separation Membrane based on Mixed Oxide Ionic-Electronic Conductor

酸化物イオン - 電子混合伝導性酸化物を用いた

酸素分離膜に関する研究

Kento Ishii

石井 健斗

March, 2020

Materials Chemistry and Engineering Course

Graduate School of Chemical Sciences and Engineering

Hokkaido University

Contents

| | |
|---|-----|
| Chapter 1 Introduction | 3 |
| 1.1. Global environment and energy issues | 3 |
| 1.2. Industrial gases use | 6 |
| 1.3. Air separation gas | 8 |
| 1.4. Manufacturing technology of air separation gas | 10 |
| 1.5. Oxygen separation membrane using Mixed Oxide Ionic-Electronic Conductor (MIEC)..... | 16 |
| 1.6. Ceramics Processing | 36 |
| 1.7. Purpose of this study | 56 |
| References | 58 |
| Chapter 2 Application of electrophoretic deposition process to BSCF asymmetric membrane..... | 82 |
| Preface..... | 82 |
| 1. Introduction | 82 |
| 2. Experimental methods..... | 85 |
| 3. Results and discussion..... | 90 |
| 4. Conclusions | 96 |
| References | 98 |
| Chapter 3 Fabrication of BSCF multi-layered oxygen separation membrane using sequential electrophoretic deposition process..... | 102 |
| Preface..... | 102 |
| 1. Introduction | 102 |
| 2. Experimental methods..... | 103 |

| | |
|---|-----|
| 3. Results and Discussion | 106 |
| 4. Conclusions | 110 |
| References | 112 |
| Chapter 4 Fabrication of BSCF porous body with excellent pore connectivity .. | 115 |
| Preface..... | 115 |
| 1. Introduction..... | 115 |
| 2. Materials and methods | 119 |
| 3. Results and discussion | 120 |
| 4. Conclusions..... | 129 |
| References | 130 |
| Chapter 5 Development of novel materials for dual-phase membrane | 136 |
| Preface..... | 136 |
| 1. Introduction | 137 |
| 2. Experimental procedure | 140 |
| 3. Results and discussion..... | 142 |
| 4. Conclusions | 156 |
| References | 158 |
| Chapter 6 Summary | 168 |
| Appendix..... | 172 |
| Acknowledgments..... | 175 |

Chapter 1 | Introduction

1.1. Global environment and energy issues

Since the industrial revolution at the beginning of the 19th century, global industrial activity has continued to increase, and energy consumption has been increasing year by year [1–9]. As shown in Fig1-1-1 (a), the demand for electricity and energy is expected to increase further in the future due to rapid economic growth and population growth in emerging countries. Until now, human beings have mainly used fossil fuels such as coal, oil, and natural gas as energy sources. Accordingly, the emission of air pollutants, such as nitrogen oxides, sulfur oxides, and carbon dioxide, has become a serious social issue. NO_x and SO_x are causative agents of acid rain, which acidify rivers and soils, adversely affect ecosystems and degrade buildings and structures [10–14]. In addition, CO₂ is called a greenhouse gas and has a great impact on climate change on a global scale [14–19]. Continuing reliance on fossil fuels is likely to lead to greater pollution and climate change in the future.

At the 3rd Session of the Conference of the Parties to the United Nations Framework Convention on Climate Change (COP3) in 1997, the world's first international target for greenhouse gas reduction (Kyoto Protocol) was adopted. At COP21 in 2015, the Paris Agreement was adopted, and the greenhouse gas emission reduction target was expanded to include not only developed countries but also emerging countries [20–27]. These environmental issues are spreading globally toward the realization of a carbon-recycling society. Additionally, changes in fossil fuel prices due to fossil fuel depletion and political factors, such as a oil crisis are also important issues, therefore methods which enable the stable supply of energy are being sought.

In order to solve these problems, attempts have been made to reduce fuel consumption and save energy by improving the efficiency of conventional power generation methods, such as thermal power generation. As an alternative energy source, the introduction of solar, geothermal and wind power generation methods using renewable energy that is clean and has little impact on the environment is being promoted. In addition, hydrogen produces only water even when it burns, so in recent years, efforts have been actively made to establish a hydrogen energy-based society. Fuel cells, which are power generation devices using hydrogen, have been put into practical use in homes, in-vehicle use, and emergency use, and are being installed in large power generation facilities. Research is ongoing, not just in the power generation, but also in the development of power storage devices such as Li-ion batteries. In recent years, the concept of a “Smart Grid” that comprehensively manages all these power generation and storage methods by using information technology has been proposed [28–32]. In order to achieve a high efficiency of energy resources, technological development has been actively conducted in various fields as already described.

As shown in Fig1-1-1 (b), thermal power generation (e.g., using coal, natural gas, oil) currently accounts to 60% of the world's power generation, and is the most widely used power generation method. The improving efficiency of thermal power generation greatly contributes to the reduction of NO_x, SO_x, and greenhouse gas emissions. In recent years, thermal power generation has shifted from use of a simple steam turbine to an Integrated Coal Gasification Combined Cycle (IGCC) that uses a steam turbine and a gas turbine, resulting in large gains in efficiency [33–41]. The integrated Coal Gasification Fuel Cell Combined Cycle (IGFC), which incorporates fuel cells into IGCC facilities, is also in the demonstration stage [42–45]. Particularly, in recent years, oxyfuel

combustion technology using pure oxygen or oxygen-enriched gas as a combustion-supporting gas instead of air has also attracted attention to further improve power generation efficiency and environmental performance [46–50]. In the general air combustion method, oxygen (approximately 21% of the atmosphere) contributes to combustion, but the remaining nitrogen does not. Therefore, when pure oxygen is used, the combustion efficiency can be improved, the amount of exhaust gas can be reduced, and nitrogen oxides can be reduced, which enables Carbon dioxide Capture and Storage (CCS). CCS is a technology for underground storage of exhausted high-purity carbon dioxide because the gas discharged by the pure oxygen combustion method is only carbon dioxide and water vapor.

In recent years, there has been a strong demand for the development of oxyfuel combustion technology to realize the CCS [51]. In particular, technologies for producing high-purity oxygen and separating and storing carbon dioxide in an exhaust gas are being developed. Industrially, pure oxygen has been produced by cryogenic air separation units (ASU). This method requires a large amount of energy in the process of creating a high pressure and extremely low temperature. For this reason, alternative oxygen separation methods are attracting attention as they can significantly reduce the amount of energy used than the current ASU technology and can effectively use the exhaust heat from the facility [52–60].

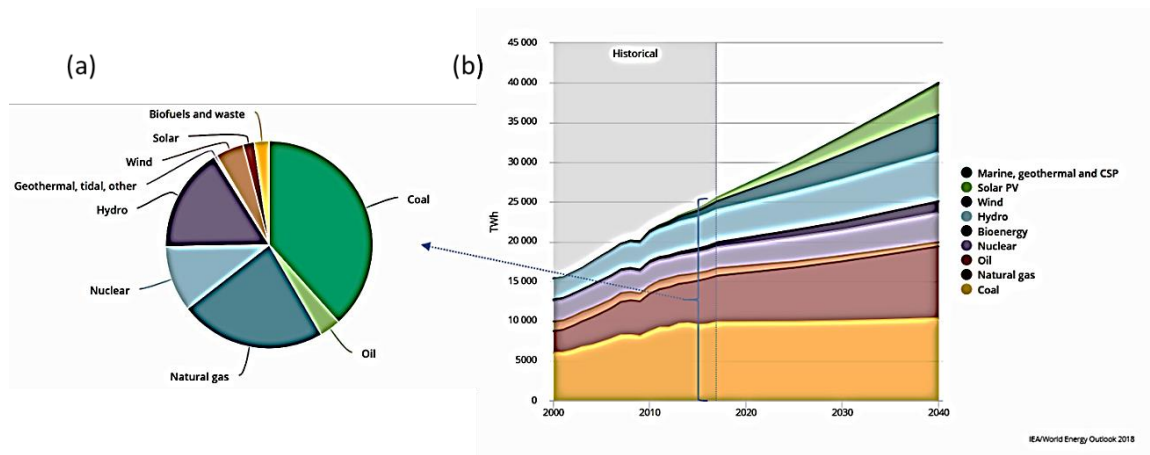


Fig. 1-1-1 World gross electricity production, by source, 2017 (a) and 2000-2040 (b) [2]

1.2. Industrial gases use

Many types of atmospheric gases and source gases have been used in various industrial fields such as steel, chemical, glass, electronics, shipbuilding, automobiles, pulp, energy, food, aviation and space, agriculture and biotechnology, and medicine [61–63]. Typical industrial gases are classified by application as shown in Table 1-2-1. In addition to these gases listed in Table 1-2-1, the following gases are likewise used only in their respective specific fields.

- (1) Industrial single gas: Oxygen (O_2), Nitrogen (N_2), Argon (Ar), Neon (Ne), Krypton (Kr), Xenon (Xe), Helium (He), Carbon dioxide (CO_2), Hydrogen (H_2), Acetylene (C_2H_2), Liquefied Petroleum (LP) Gas
- (2) Industrial gas mixture: Shielding gas for welding, Laser oscillation gas
- (3) Special gas for semiconductors (high-purity gas): O_2 , N_2 , Ar, Monosilane (SiH_4), Arsine (AsH_3), Phosphine (PH_3), Diborane (B_2H_6), Monogerman (GeH_4), etc.
- (4) Medical gas: O_2 , Synthetic air, Nitrous oxide (N_2O)

Table 1-2-1 Industrial gas application [64]

| Industry | Oxygen (O ₂) | Nitrogen (N ₂) | Argon (Ar) | Helium (He) | Carbon dioxide (CO ₂) | Hydrogen (H ₂) |
|----------------------------------|--------------------------|----------------------------|------------|-------------|-----------------------------------|----------------------------|
| Steel / Nonferrous | ◎ | ○ | ◎ | - | ○ | ○ |
| Machine / Metal processing | ◎ | ◎ | ◎ | ○ | ◎ | ◎ |
| Automobile / Ship | ◎ | ○ | ◎ | - | ◎ | - |
| Civil engineering / Construction | ○ | ○ | ○ | - | ○ | - |
| Chemical / Medicine | ◎ | ◎ | ○ | ○ | ○ | ◎ |
| Nuclear | - | ○ | ○ | ○ | - | - |
| Superconductivity | - | ○ | - | ◎ | - | - |
| Aerospace | ○ | ○ | - | ○ | - | ○ |
| Marine | ○ | ○ | - | ○ | - | - |
| Glass / Ceramic | ◎ | ○ | - | ◎ | - | ◎ |
| Pulp | ◎ | ○ | - | - | - | - |
| Electronics | ○ | ◎ | ○ | ○ | - | ○ |
| Food | | ◎ | - | - | ◎ | - |
| Medical | ◎ | ○ | - | ◎ | ○ | - |
| Agriculture / Bio | | ○ | - | - | ○ | - |
| Environment | ○ | ○ | - | - | ○ | - |

Among these, oxygen, nitrogen, and argon are manufactured by separation from air. The characteristics of each gas are shown below.

(1) Oxygen

Oxygen is extremely chemically active; it has a strong ability to oxidize other things (combustion-supporting property) and combines with many elements. When pure oxygen is used instead of air, high-temperature combustion is possible, so it is widely used for combustion-related applications. Oxygen is an indispensable gas for removing impurities such as desulfurization and dephosphorization in the steel industry, and for plasma and laser cutting in metal processing. A large amount of oxygen is used for glass melting and pulp bleaching. Oxygen is an important gas even in the medical field. In recent years, due to the population aging in Japan, home medical care has been popularized, and pure oxygen has been used for home oxygen therapy. In addition, ozone produced from oxygen has effects such as sterilization, deodorization, bleaching and purification.

(2) Nitrogen

Nitrogen gas is the most used industrial gas. It is an inert gas, widely used for controlling the heat treatment and sintering of semiconductors and metal compounds, for purging and preventing oxidation in the petroleum field, and as a purge and carrier gas in the semiconductor field. Nitrogen is also inert in liquids, and is used for the freeze processing of foods and freeze preservation of special substances.

(3) Argon

Argon is very chemically inert and does not combine with other elements even at high temperatures and pressures. It is used as an atmosphere gas during stainless steel refining and silicon single crystal production, and as a seal gas during welding.

1.3. Air separation gas

Industrial gases are widely used for raw materials and atmosphere control. In particular, nitrogen, oxygen and argon, produced by separating air, are called air separation gases [65–69]. They account for the top three gas productions in the world. As shown in [Figures 1-3-1 and 1-3-2](#), the production volume is increasing year by year in Japan, contributing significantly to worldwide production. The production volume of these gases will continue to increase in the future as industrial activities become more active. Efficient separation and production methods for these gases are roughly divided into three processes: cryogenic separation, pressure swing adsorption, and membrane separation. The principle of the separation method is described below.

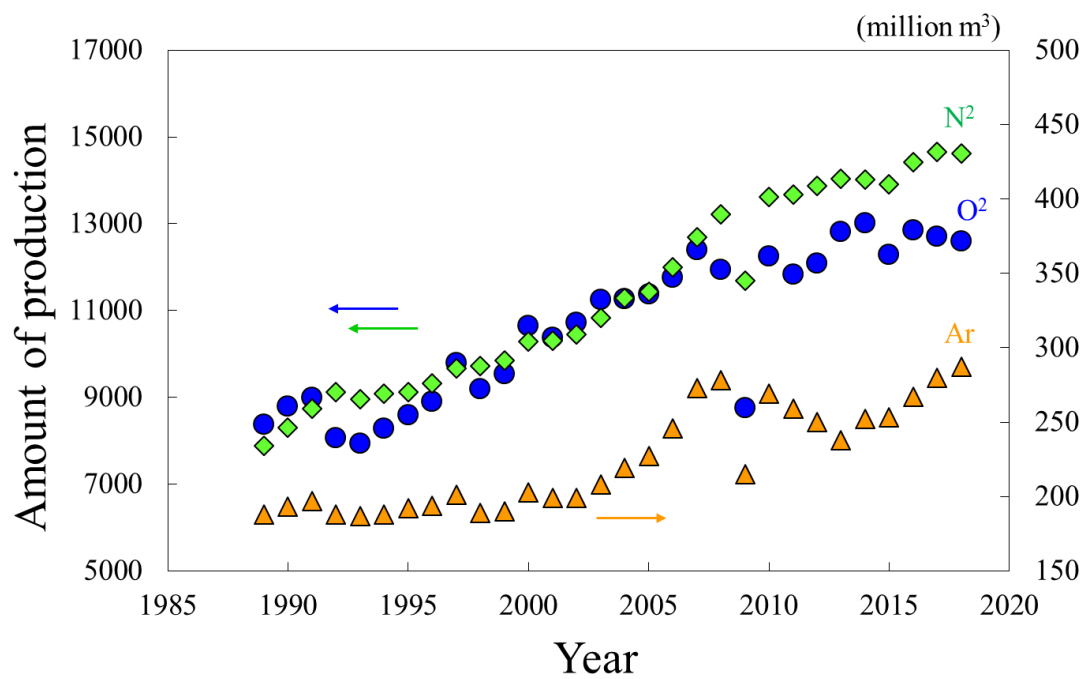


Fig.1-3-1 Production of air separation gas in Japan [70]

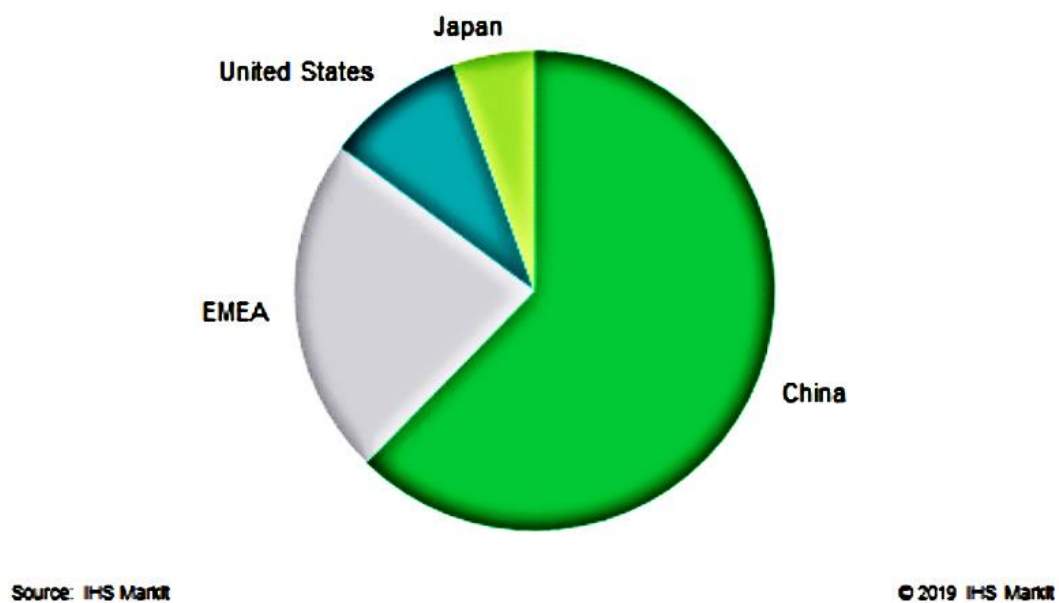


Fig. 1-3-2 Production of oxygen by major region in 2018 [71]

1.4. Manufacturing technology of air separation gas [72–77]

1.4.1. Cryogenic separation

Cryogenic separation is a technology in which air is compressed, purified, cooled, and liquefied, then nitrogen, oxygen, and argon are separated from the liquefied air using the difference in boiling points. In this method, each component can be separated and concentrated by continuously distilling the liquefied air under the gas-liquid equilibrium condition of the gas composition ratio of the liquefied air containing a plurality of components.

In a general cryogenic air separation device, air can be divided into nitrogen, oxygen and other gases; therefore, nitrogen and oxygen can be simultaneously produced. By adding a distillation apparatus for separating argon to this, oxygen, nitrogen and argon can be simultaneously produced. There are four types of cryogenic air separation devices; i.e., oxygen production device, nitrogen production device, the device that simultaneously produces oxygen and nitrogen, and the device that simultaneously produces oxygen, nitrogen, and argon, with the latter called an air separation unit (ASU).

1.4.2. Pressure swing adsorption

A system in which adsorption separation is repeated is called a pressure swing adsorption (PSA) method. In the adsorption separation method, the adsorbent is reused by driving out adsorbed gas molecules. If the adsorption is performed at high pressure and the desorption is performed at low pressure, the adsorbent can be repeatedly used. In the PSA method, a specific gas is concentrated by repeated adsorption and desorption

using the difference in the adsorption rate, not the difference in the equilibrium adsorption amount of each gas component.

1.4.3. Membrane separation

Membrane separation is a method capable of concentrating a single component gas by using the difference in the partial pressure between the gas components on the upstream side and downstream side across a separation membrane and the difference in the membrane permeation speed of each component. Membrane separation is characterized by a low energy consumption because it can continuously separate gases and has a relatively high separation performance. The efficiency of this method depends on the gas partial pressure difference, and when the upstream partial pressure approaches the downstream partial pressure, further separation is impossible. Therefore, there are limitations on the yield and product purity. While gas produced by the cryogenic separation method is a high-pressure gas, and its handling is subject to legal regulations in Japan, the gas produced by the membrane separation method is not regulated because it is not a high-pressure gas. In addition, the membrane separation method requires a simpler apparatus than the PSA method, and gas separation can be easily performed.

Gas separation by a membrane is classified into two methods; i.e., using a porous membrane and using a nonporous membrane. In the case of a porous membrane, gas molecules are physically separated by Knudsen diffusion and the molecular sieving mechanisms by using a microporous material having a pore diameter similar to the size of gas molecules as shown in [Table1-4-1](#). On the other hand, in the case of a nonporous

membrane, specific gas molecules are separated by a dissolution-diffusion mechanism. This gas separation characteristic is based not on the size of the gas molecule but on the difference between the affinity between the gas molecule and the membrane surface and the difference in the permeation rate of the gas molecule in the membrane.

The membrane separation materials in practical use are shown in [Table 1-4-2](#). Many of the gas separation membrane materials that have been practically used are polymer materials. In particular, a hollow fiber-structured polymer membrane is used for air separation. In the case of the hollow fiber membrane, untreated air is circulated inside the hollow fiber. Moisture, carbon dioxide, and oxygen are permeated out of the membrane and discharged through the membrane, so that nitrogen is concentrated toward the outlet side. Gas separation by a hollow fiber membrane is not 100% gas selective and the method is difficult to separate argon, methane, carbon monoxide, etc., so it is used for the production of relatively low purity nitrogen (95-99.9%). Therefore, an air separation membrane having a high selectivity and high separation efficiency is required. In addition, the development of inorganic gas separation membranes for chemical manufacturing processes using zeolite, silica, and carbon with an excellent heat resistance and chemical resistance has been actively conducted.

Table1-4-1 Types of membrane separation and separation range

| Size | 10 ⁻⁷ mm | 10 ⁻⁶ mm | 10 ⁻⁵ mm | 10 ⁻⁴ mm | 10 ⁻³ mm | 10 ⁻² mm |
|---------------------------|---------------------|---------------------|---------------------|---------------------|------------------------|---------------------|
| | 1Å | 1nm | 0.01µm | 0.1µm | 1µm | 10µm |
| Approx. Molecular Weight | 50 | 100 | 200 | 1000 | 10,000 | 100,000 |
| Range | Gas and Ionic | | Molecular | | Macro molecular | |
| Process for Separation | Reverse osmosis | | Dialysis | | Microfiltration | |
| | Nanofiltration | | Ultrafiltration | | Particulate filtration | |
| | Gas separation | | Ion exchange | | | |
| | Microporous | | Mesoporous | | Macroporous | |
| Types of Membrane | Non-porous | | | | | |
| Relative Size of Material | Water | Acid | Colloid | | Visible Particles | |
| | Air | Aqueous salts | Hemoglobin | | Silt | |
| | Metal ion | | Carbon black | | Paint pigments | |
| | Atomic radii | Glucose | Colloidal silica | | Bacteria | |
| | | | Viruses | | Red blood cell | |
| | | | | | Pollen | |
| | | | | | Fine sand | |

Table1-4-2 Examples of practical use of gas separation membranes [78]

| Application | Materials | Membrane structure | Separation layer | Mechanism |
|---|--|-----------------------|------------------|------------------------|
| Inorganic gas separation H ₂ , He, O ₂ , N ₂ , CO ₂ etc. | Polyimide, cellulose acetate, Polysulfone, polyamide, polyetherimide, etc. | Hollow fiber | Non-porous | Solution-diffusion |
| High purity H ₂ production | Palladium metal | Thick film, composite | Non-porous | Solution-diffusion |
| Dehumidification | Polyimide, cellulose acetate, Fluorine resin, etc. | Hollow fiber | Non-porous | Solution-diffusion |
| Volatile organic substances | Silicon rubber | Composite | Non-porous | Solution-diffusion |
| H ₂ separation from Hydrocarbon, H ₂ S, H ₂ | Carbon | Composite | Microporous | Selective surface flow |
| Separation of hydrocarbon, inorganic gas etc. | Carbon | Hollow fiber | Microporous | Molecular-sieving |
| Concentration of uranium | Porous alumina | Tubular | Porous | Molecular flow |

1.4.4. Comparison of manufacturing technology

The characteristics of each separation method are shown in [Table 1-4-3](#). As already described, the cryogenic separation method can simultaneously produce high-purity oxygen, nitrogen, and argon from the atmosphere, and can produce a liquefied gas. The cryogenic separation method requires enormous energy for gas liquefaction and distillation of the liquefied mixed gas. The PSA method and the membrane separation method can separate only one specific component from the atmosphere, but the scale of the equipment is small compared to the cryogenic separation method. Similarly, the PSA method requires high energy because the gas is adsorbed and desorbed by the pressure change and thermal energy. On the other hand, the membrane separation method is a low energy gas separation technique in which gas separation is performed at a relatively low pressure, but the purity of the produced gas is relatively low. Membrane separation technology has been commercialized for nitrogen gas, but not yet commercialized for oxygen. As shown in [Fig. 1-4-1](#), the membrane separation technology is still developing compared to the other methods.

Table 1-4-3 Industrial air separation method [79,80]

| Product | Oxygen | Nitrogen | Argon | Purity | Scale | Energy intensity | Technical status |
|---|--------|----------|-------|---|--------|------------------|------------------|
| Cryogenic separation (Air separation unit : ASU) | ○ | | | High >99.8% O ₂ >99.999% N ₂ | Large | High | Established |
| | | ○ | | | | | |
| | ○ | ○ | | | | | |
| | ○ | ○ | ○ | | | | |
| Pressure swing adsorption (PSA) | ○ | | | Medium 90-93% O ₂ 99-99.99% N ₂ | Medium | Medium | Established |
| | | ○ | | | | | |
| Membrane separation | ○ | | | Low 95-99% N ₂ | Small | Small | Emerging |
| | | ○ | | | | | |

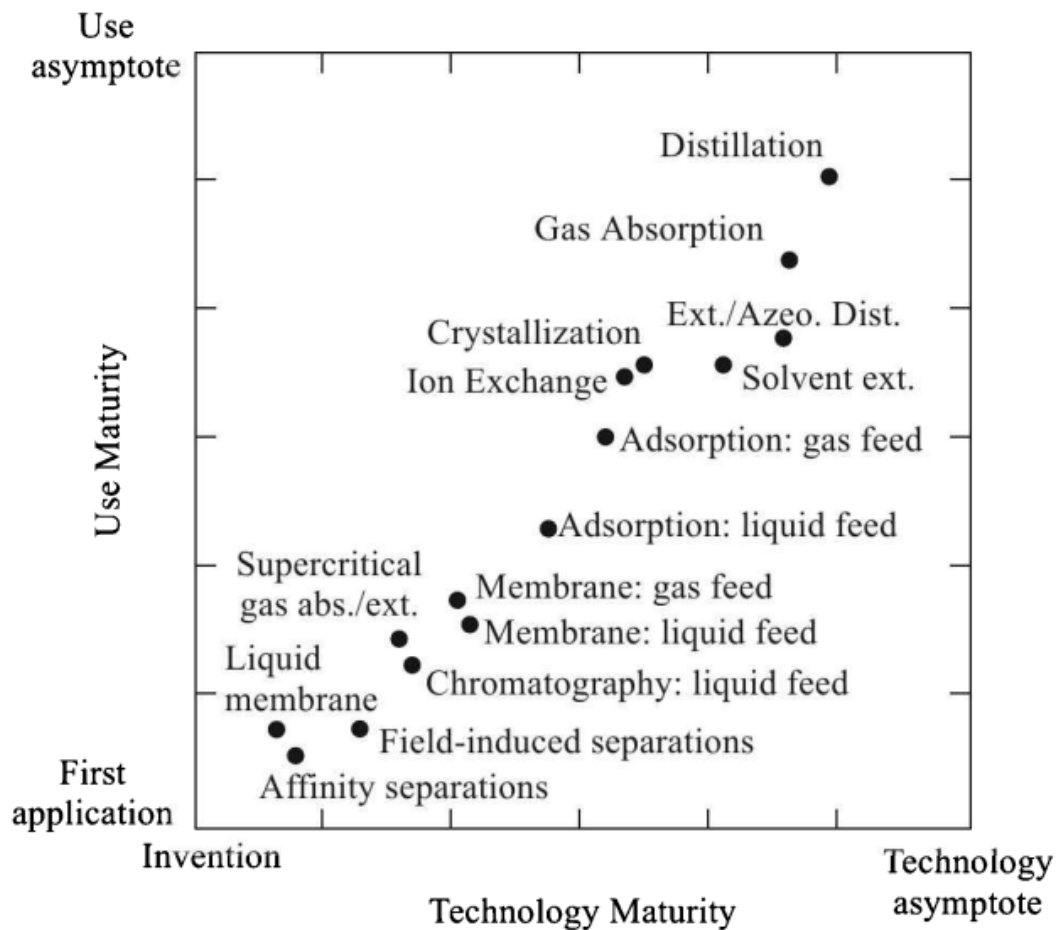


Fig1-4-1. Technologies and use maturities of separation techniques [81]

1.5. Oxygen separation membrane using Mixed Oxide Ionic-Electronic Conductor (MIEC)

1.5.1. Principle and features of MIEC-based oxygen separation membrane

An oxygen separation membrane using MIECs having both oxide ion conduction and electron conduction is an electrochemical device that can selectively separate only oxygen [82–88]. The operation principle of the MIEC oxygen separation membrane is shown in Fig. 1-5-1. The operating principle is as follows: when an oxygen partial pressure difference is applied to both sides of a dense MIEC film, a chemical potential gradient of oxygen would be formed across the membrane. On the surface of the membrane on the high oxygen partial pressure side, oxygen gas adsorbs and dissociates to generate oxide ions. The generated oxide ions diffuse in the lattice of the membrane driven by a concentration gradient. As a result, oxide ions re-associate into oxygen gas on the film surface on the low oxygen partial pressure side. Finally, to maintain the overall charge neutrality in the membrane, electrons separated from the oxide ions diffuse in the opposite direction of the oxide ions. The electrons returning to the high oxygen partial pressure side contribute again to the oxygen dissociation reaction.

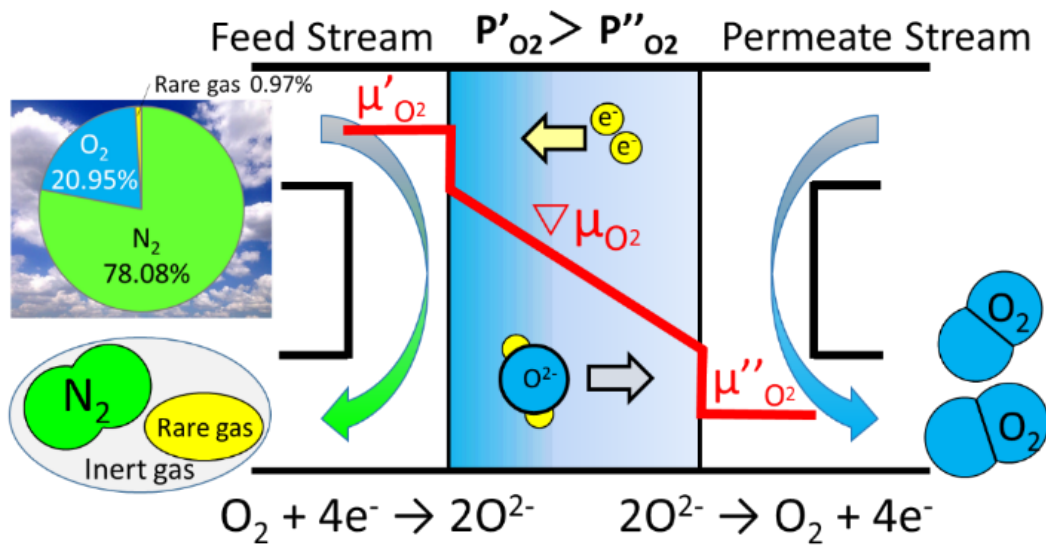


Fig. 1-5-1 Oxygen separation mechanism of dense MIEC membrane

The requirements for the operation of the oxygen separation membrane are as follows: a temperature of 600-1000°C at which oxide ions can sufficiently move, a dense, gas-tight membrane structure, and a sufficient high oxygen partial pressure difference. This membrane does not require an external circuit like a zirconia oxygen pump as shown in Fig. 1-5-2. It is a simple mechanism and the device can be scaled down. Theoretically, oxygen with 100% purity can be obtained with a single film. Such an oxygen separation membrane is expected to be applied to a high-temperature gasification melting furnace, an iron manufacturing process, an oxygen-enriched incinerator, etc. By supplying separated pure oxygen to these furnaces, it is possible to improve the combustion efficiency, reduce NO_x emissions, and increase the purity of the emitted carbon dioxide for CCS technology. At this time, the heat energy necessary for the operation of the oxygen separation membrane can utilize the exhaust heat from these facilities. In

addition, as shown in [Figure1-5-3](#), it is expected to be applied as a membrane reactor that generates synthesis gas by reacting oxygen and reactants immediately after separation.

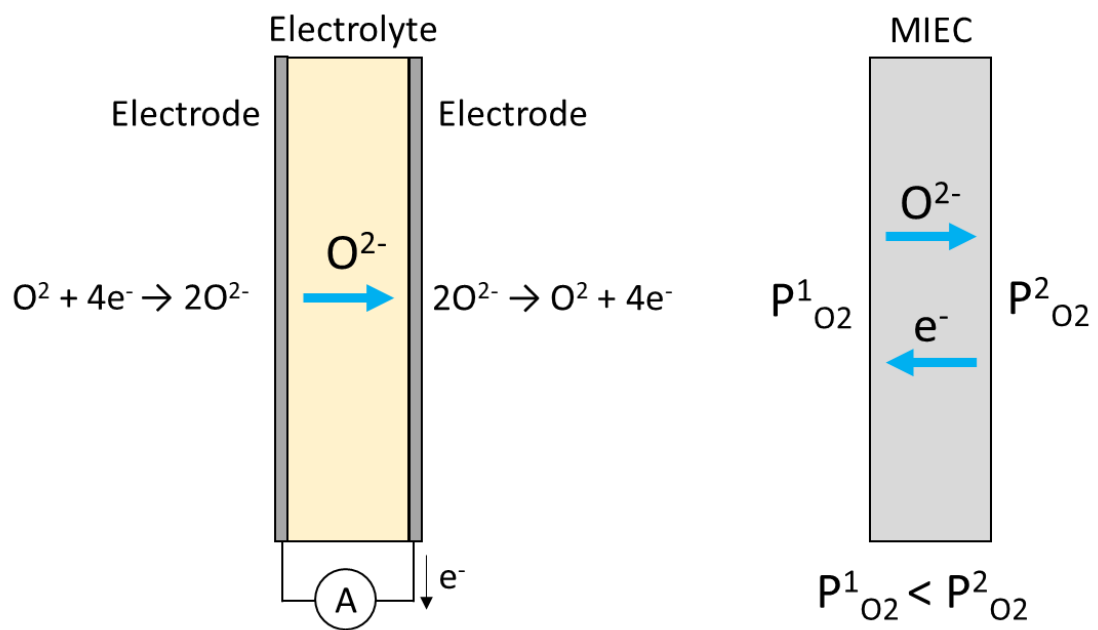


Fig. 1-5-2 Zirconia type oxygen pump (a) and MIEC oxygen separation membrane (b)

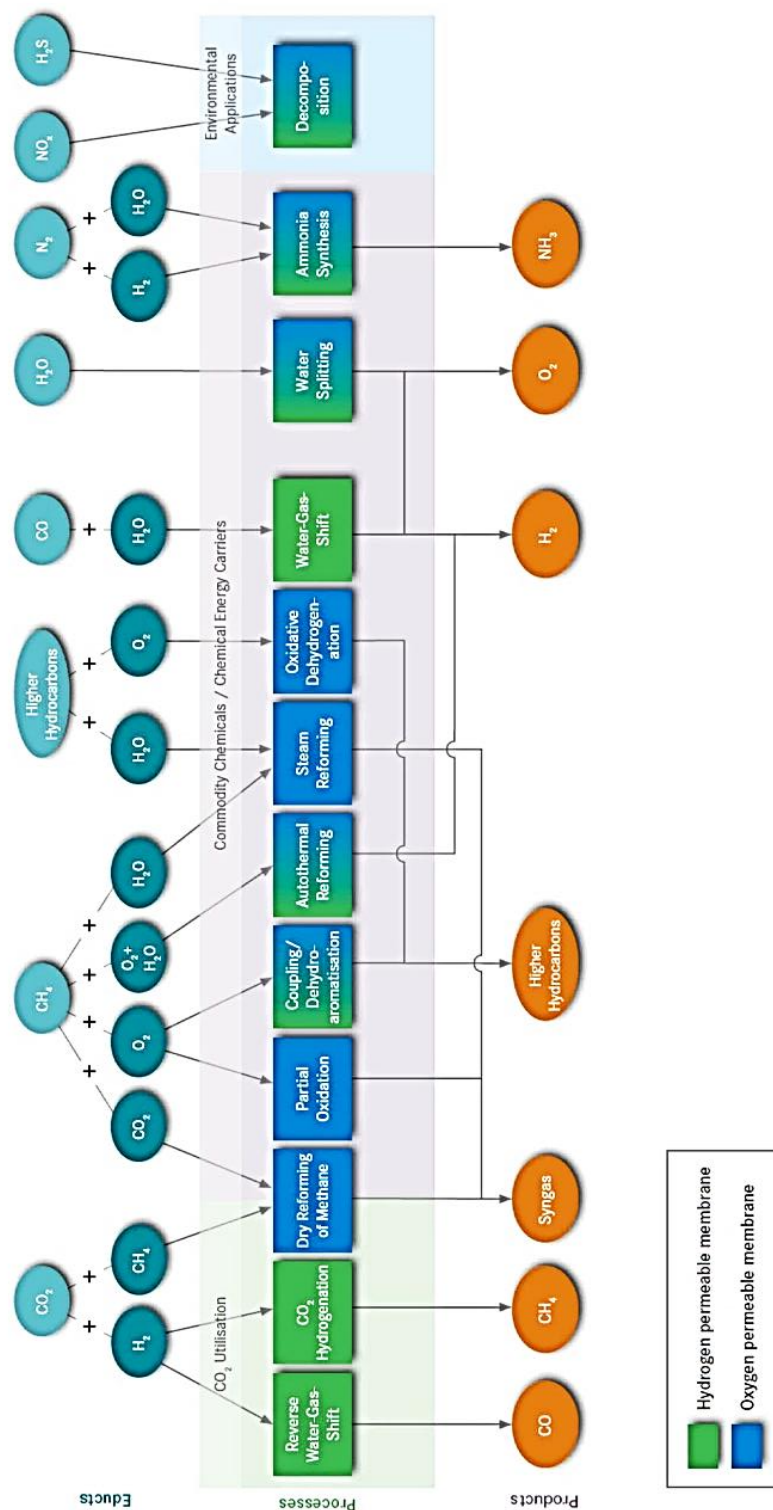


Fig. 1-5-3 Summary of selected processes where oxygen- and hydrogen-permeable membrane are applicable [89]

The theoretical electrochemical oxygen permeation flux j_{O_2} ($\text{mol} \cdot \text{cm}^{-2} \cdot \text{s}^{-1}$) of a mixed oxide ionic-electronic conductor is derived from the Wagner's equation (1-1) [90].

$$j_{O_2} = -\frac{RT}{16F^2L} \int_{\ln P(O_2)'}^{\ln P(O_2)''} \frac{\sigma_i \sigma_e}{\sigma_i + \sigma_e} d \ln P(O_2) \quad (1-1)$$

where σ_i is the oxide ion conductivity (S/cm), σ_e is the electronic conductivity (S/cm), R is the gas constant (8.314 J/mol·K), F is the Faraday constant (96485 C/mol), T is the temperature (K), L is the film thickness (cm), and P_{O_2} is the oxygen partial pressure (atm). Fig. 1-5-4 shows oxygen partial pressure dependence of the electrical conductivity and oxygen permeation flux of MIEC. The oxide ion conductivity σ_i and the electron conductivity σ_e are determined by the lower value of the two, and these values should be similar. Therefore, to improve the oxygen permeation flux, it is required to improve the mixed conductivity, to reduce the film thickness, and to have a large difference in the oxygen partial pressure between both sides of the membrane. Furthermore, the surface exchange reaction concerning the adsorption dissociation between oxygen and oxide ions on both surfaces of the membrane is also an important factor for improving the oxygen separation efficiency.

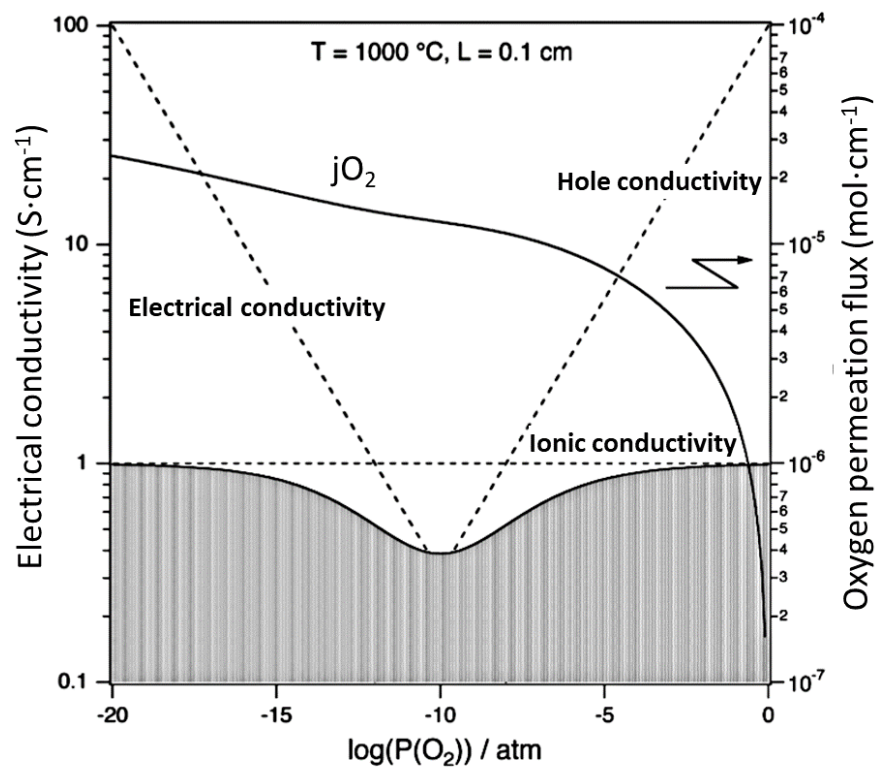


Fig. 1-5-4 Oxygen partial pressure dependence of electrical conductivity and oxygen permeation flux of MIEC [91]

1.5.2. Mixed oxide Ionic-Electronic Conductors (MIEC)

In general, oxide ion conductors are used as electrolyte materials in solid oxide fuel cells, oxygen pumps, and oxygen sensors. In order for oxide ions to move in a solid, it is necessary to have vacancies in which the oxygen atoms do not exist at the lattice points. When oxide ions at the lattice points move and diffuse while exchanging positions with neighboring lattice defects, such as oxygen vacancies, oxide ion conductivity occurs. There are substances in which the electronic conductivity increases due to the occurrence of defects. On the other hand, many substances having a fluorite-type structure or a perovskite-type structure that can stably exist exhibit an oxide ion conductivity, even when lattice defects are generated.

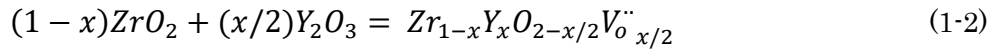
Electronic conductors are used as electrode materials in solid oxide fuel cells, exhaust gas catalysts, various gas sensors, spintronics fields, etc. Mixed conductors are materials having properties of both oxide ionic conduction and electronic conduction [82,84,88,92–94]. The composite materials of the oxide ion conductors and the electronic conductors are also mixed conductors.

1.5.2.1. Crystal structure

1.5.2.1.1. Fluorite-type crystal structure

The structure of the fluorite face-centered cubic is shown in Fig. 1-5-5. The fluorite-type crystal structure, the general formula of which is given by MO_2 , is derived from the mineral fluorite (CaF_2). Ca^{2+} is surrounded by 8 F^- (8-coordinate), and F^- is surrounded by 4 Ca^{2+} . The coordination number of cations and anions is 8: 4, and the condition that

must be met for a material to exist as a fluorite structure is that the radius ratio of cations and anions is $r^+ / R^- > 0.732$. When alkaline earth elements or rare earth elements with different valences are substituted at the cation sites of the fluorite-type oxide, oxygen corresponding to the lack of valences is released and oxygen vacancies are formed in order to maintain electrical neutrality. Oxide ion conductivity develops when the oxide ions move while exchanging positions with the oxygen vacancies. As an example, the reactions in which Y_2O_3 is dissolved in ZrO_2 and oxygen vacancies are generated are shown by equations (1-2) and (1-3).



Here, V_o'' is oxide ion deficiency. According to the Kröger-Vink notation:



The properties of the fluorite-type structure include a stable crystal structure and no phase transition, a high melting point, thermodynamic stability at high temperatures, cation substitution, and the generation of oxygen vacancies. ZrO_2 -based and CeO_2 -based oxides having a fluorite structure are well-known as oxide ion conductors. In particular, CeO_2 -based oxides have been studied as fluorite-type mixed conductors because they exhibit an electronic conduction when part of Ce^{4+} is reduced to Ce^{3+} in the low oxygen partial pressure region above 700°C.

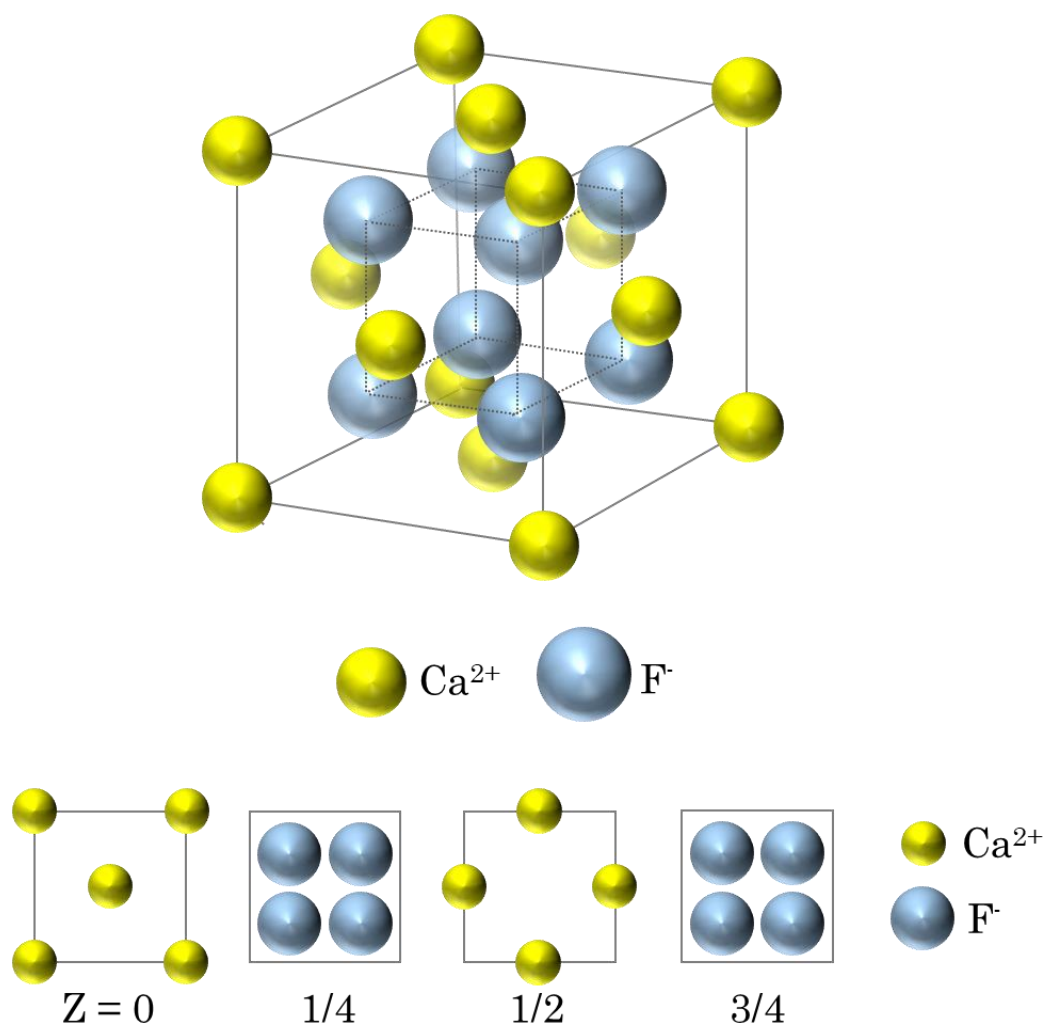


Fig. 1-5-5 Crystal structure of fluorite face-centered cubic

1.5.3.1.2. Perovskite-type crystal structure

The perovskite crystal structure, the general formula of which is given by ABO_3 , is derived from the calcium titanate ($CaTiO_3$) mineral (perovskite). Its ideal structure is a simple cubic. As shown in [Fig. 1-5-6 \(B-type unit cell\)](#), the B-site element is located at the body center position, oxygen (or anion) is coordinated at the face center position, and the B-site element is located at the center of the oxygen octahedron structure. The A-site element is located at the apex of a simple cubic lattice. The A-site has a 12-coordinate structure of the oxygen as shown in [Fig. 1-5-6 \(A-site unit cell\)](#). By substituting the elements at the A site and B site with other elements, the symmetry of the crystal structure decreases and rhombohedral, hexagonal and orthorhombic crystal structures are formed. The crystal structure of the perovskite-type oxides is stable even when the composition becomes non-stoichiometric due to the lack of A-site elements and oxygen. In addition, both an A-site element and B-site element can be substituted with other elements. In general, it is known that an oxide having a perovskite structure changes its electrical and dielectric properties depending on the valences of the A and B cations. There are three combinations of A and B cations: $1+:5+$, $2+:4+$ and $3+:3+$. Since the ionic radius of the A element should be larger than that of the B element, the alkali metal and alkaline earth metal are structurally substituted by the A-site, and the transition metal and group VIII metal are substituted by the B-site. In general, an oxide having an A: B ratio of 1: 5 or 2: 4 is an electrically insulating material, and an oxide having a 3: 3 ratio has a high conductivity. Substituting another ion with a different valence from the original ion at the A site or B site of the perovskite oxide causes defects at the oxide ion site, resulting in an oxide ion conductor or mixed ionic-electronic (or hole) conductor.

Typical perovskite-type oxide ion conductors include those based on CaTiO_3 and LaGaO_3 . Typical electron conductors include those based on LaMnO_3 , LaCoO_3 , LaFeO_3 , and LaCrO_3 . In particular, perovskite oxides in which both the A-site and B-site are substituted, such as $(\text{LaSr})(\text{CoFe})\text{O}_3$, and $(\text{BaSr})(\text{CoFe})\text{O}_3$, are known as typical mixed oxide ionic-electronic conductors.

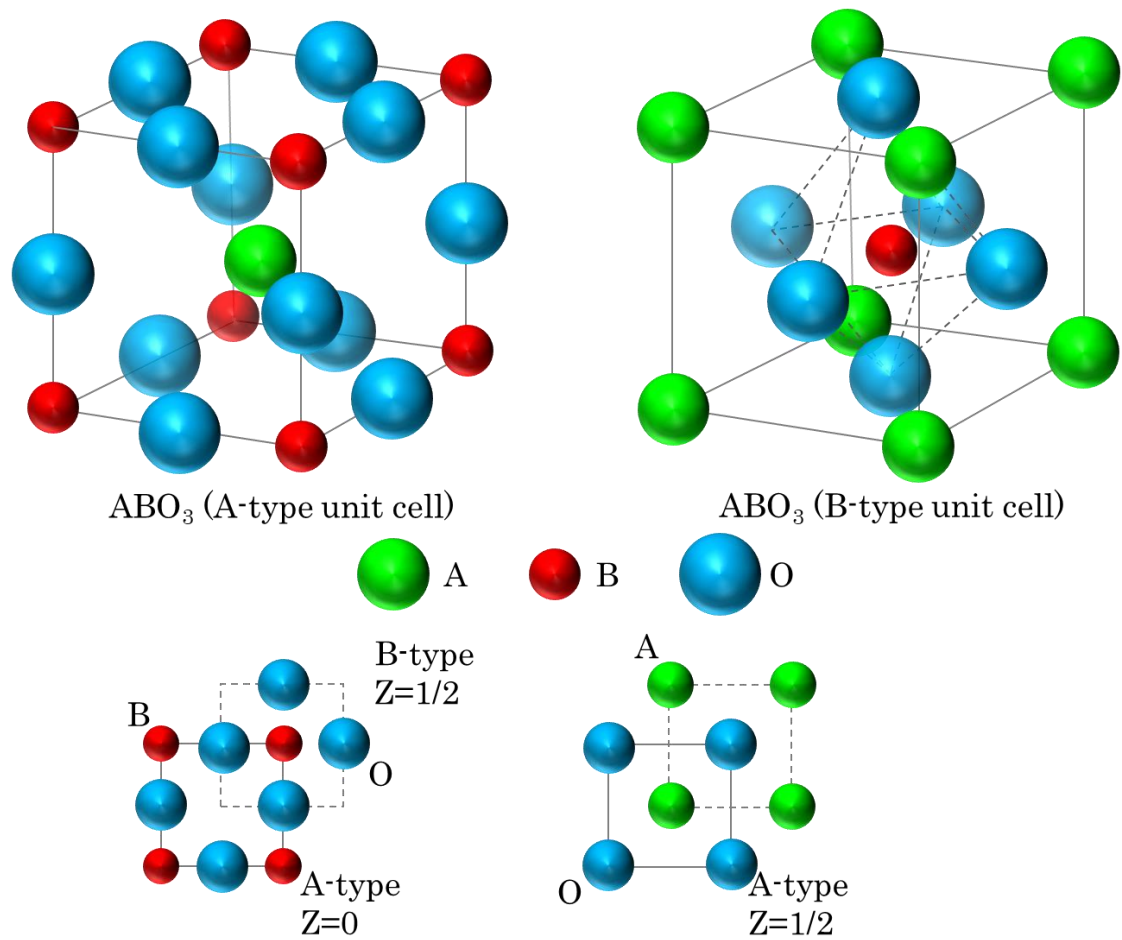


Fig. 1-5-6 Crystal structure of perovskite oxide

1.5.2.3. Composite dual-phase material

A schematic diagram of the oxygen separation mechanism of the two-phase membrane is shown in [Fig. 1-5-7](#). A dual-phase membrane is a film having an oxide ion conduction phase and an electron conduction phase composed of two different composite materials such as an ion conductor-electron conductor or an ion conductor-mixed conductor[[84,94–96](#)]. An oxide phase is used for the oxide ion conductor, and a metal or an oxide phase is used for the electronic conductor. In the dual-phase film, it is required that no reaction layer is formed at the interface and that the film is not damaged due to the difference in the thermal expansion coefficients between the two phases. In particular, it has been reported that each phase must be connected to both ends of the membrane, and in the case of [Fig. 1-5-7\(a\)](#), at least 40 vol% of the electronic conductor must be added to the oxide ion conductor. Since the oxide ionic conduction rate-controls the oxygen separation performance than the electronic conduction, it is preferable to add the oxide ionic conductive phase as much as possible. When the electronic conductor phase can be formed into a fibrous structure in the tissue structure, the amount of the electronic conductor phase can be reduced to 20 vol% as shown in [Fig. 1-5-7\(b\)](#).

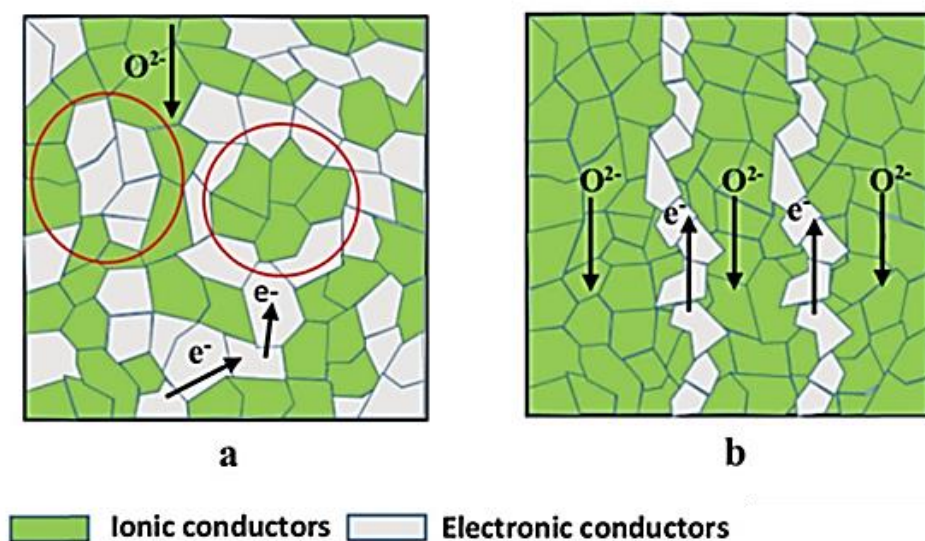


Fig. 1-5-7 Cross-sectional schematic diagram of (a) a dual-phase membrane and (b) a dual-phase membrane with a minimum electronic conducting phase (internal short-circuit). Isolated areas (referred to as an “island”) which would not contribute to the dual-phase membrane are marked by red rings in Fig. 1-5-7(a) [95].

1.5.3. Oxygen separation performances of MIEC materials

Various MIEC materials and their oxygen permeation flux are shown in Fig.1-5-8. MIEC materials include perovskite oxides, fluorite oxides, oxide-metal or oxide-oxide composites. In order to put the MIEC-based oxygen permeable membrane into practical use, MIEC materials having a high oxygen permeability are required. Among the MIEC materials, perovskite-type MIEC has been actively developed because of its high oxygen permeability as shown in Fig. 1-5-9. The high mixed conductivity of $\text{La}_{1-x}\text{Sr}_x\text{CoO}_{3-\delta}$ -based perovskite oxide ceramics was reported in Japanese Patent Application Laid-Open No. 56-92103 in 1979. Later, in 1985, Teraoka et al. reported that $\text{La}_{0.8}\text{Sr}_{0.2}\text{Co}_{0.8}\text{Fe}_{0.2}\text{O}_{3-\delta}$ and $\text{SrCo}_{0.8}\text{Fe}_{0.2}\text{O}_{3-\delta}$ show excellent oxygen permeabilities. In particular, it has been reported

that the oxygen permeation flux of the perovskite-type MIEC is 1 or 2 orders of magnitude higher than that of YSZ (yttria-stabilized zirconia)/LaCrO₃ at 500-900°C. In this study, we selected Ba_{0.5}Sr_{0.5}Co_{0.8}Fe_{0.2}O_{3-δ} (BSCF), which has the highest oxygen permeability among all the MIEC ceramic materials. BSCF is a perovskite complex oxide having Ba and Sr at the A-site and Co and Fe at the B-site. However, in general, MIEC materials with high oxygen permeability have many defects in the crystal structure, and cracks tend to occur in the membrane, and this remains a problem for practical use.

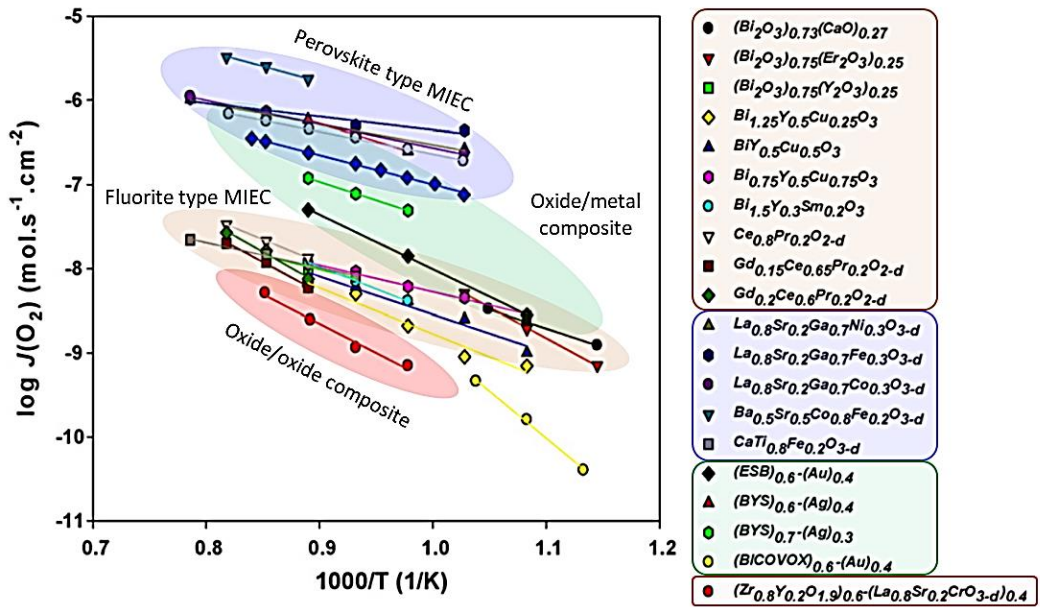


Fig. 1-5-8 Temperature dependence of oxygen flux [85]

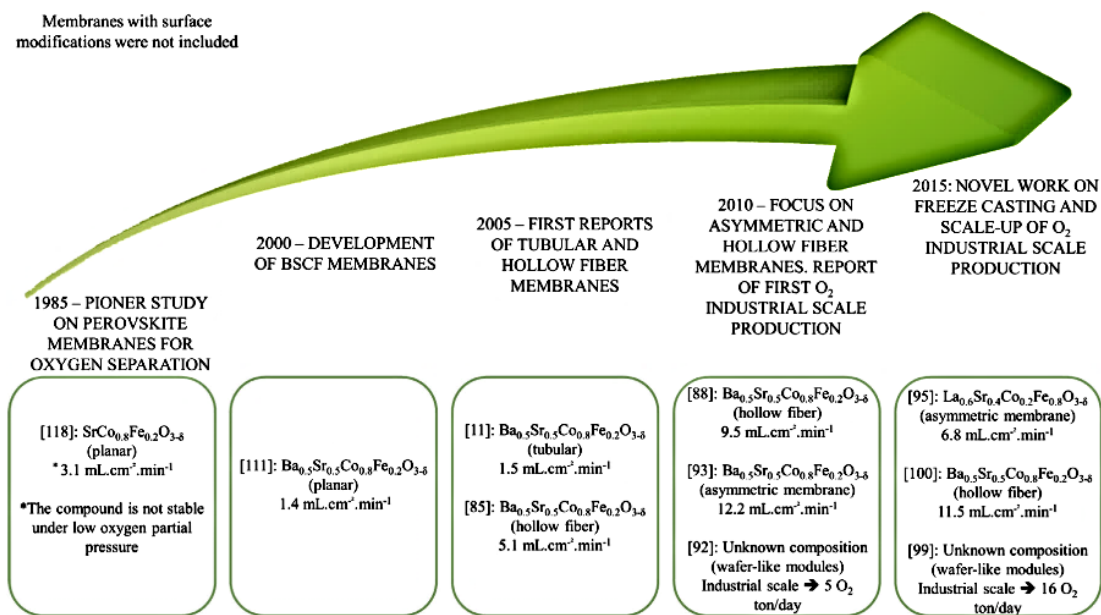


Fig. 1-5-9 Evolution of oxygen fluxed exhibited by perovskite membranes over the past decades [97]

1.5.4. Membrane structure

The general membrane classification is shown in Fig. 1-5-10. Various types of separation membranes have been devised in terms of materials, membrane structure, module, and separation mechanism. Figure 1-5-11 shows a schematic diagram of different membrane morphologies. The simplest membrane structures are a homogeneous, dense (nonporous), porous, or structure composed of a single material. These membranes are called symmetrical membranes because they have symmetrical structures as seen from the gas feed side and the gas sweep side. The symmetric structure is the most common membrane structure used as a self-standing membrane. In order to make the membrane self-supporting, it is necessary to ensure the mechanical

strength of the membrane, with a thickness of at least 0.5 mm is preferable. The asymmetric-structured membrane is composed of two layers, a thin dense layer and a porous support layer, with a single material. Composite membranes also consist of two layers, a thin dense layer, and a porous support layer, but the material of each layer is different. In the MIEC-based oxygen separation membrane, as can be seen from the Wagner equation (1-1), the oxygen permeation flux is inversely proportional to the film thickness. Therefore, in order to improve the oxygen permeation flux, it is necessary to reduce the thickness of the dense membrane to 0.5 mm or less [98,99]. Moreover, since the surface of the dense film is smooth, there are also problems, such as a small specific surface area and low surface exchange reactivity [100–102].

Asymmetric structured membranes were devised to solve the problem of reducing the thickness without any loss of mechanical strength. These membranes have an asymmetric structure as viewed from the feed side and the sweep side. Asymmetric membranes generally consist of two layers; i.e., a thin dense layer and a thick porous support layer made of the same material. Since the porous support bears the mechanical strength of the entire membrane, the dense layer formed on the porous support can be thin. In addition, asymmetric-structured membranes show a greatly improved surface exchange reactivity due to the high specific surface area of the porous support [103–108]. The requirements of this porous support are to control the porosity, gas permeability and morphology so that the feed gas can reach the surface of the dense layer while ensuring the mechanical strength of the porous support [109–112]. In particular, it is necessary to form a dense layer on the complex surface of the porous body with a high adhesion.

There are many other membrane structures, such as multi-layered structure have been reported. The types of the structures include membrane in which a catalyst layer

is modified on a self-supporting membrane. Membranes in which a porous oxygen evolution layer is formed on a dense layer having an asymmetric film structure, and membrane with a catalyst layer inserted at the layer interface between porous support and dense layer have been reported to contribute to the improvement of oxygen separation performance [105,106,113–121].

There are three module types of membranes; i.e., plate type, cylindrical type, and hollow fiber type [82,85,122–124]. Since the flat plate type has a simple structure, its production is relatively easy and its production cost is low. Another feature is that many manufacturing methods are applicable. In the plate type modules, it is important to control the stress distribution by designing the temperature distribution and gas flow path. In the cylindrical type, gas sealing is relatively easy, and a sealless structure in which one end of the cylinder is closed can be manufactured. Since a single hollow fiber membrane has a small amount of permeated gas, it is necessary to bundle multiple fibers into a module.

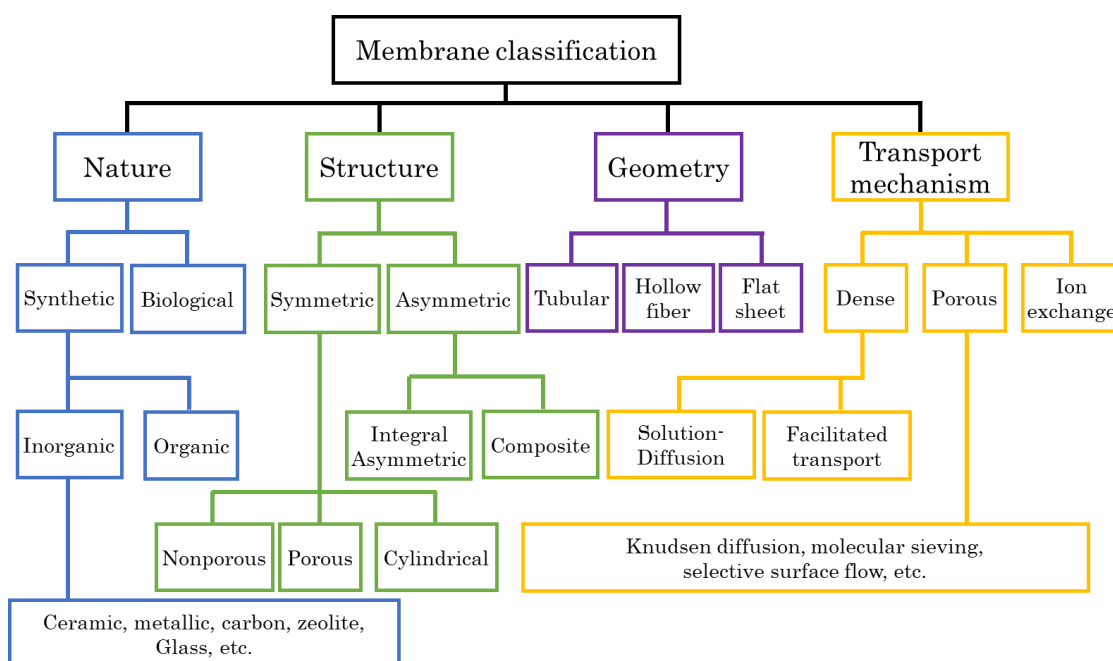


Fig. 1-5-10 Membrane classification [125]

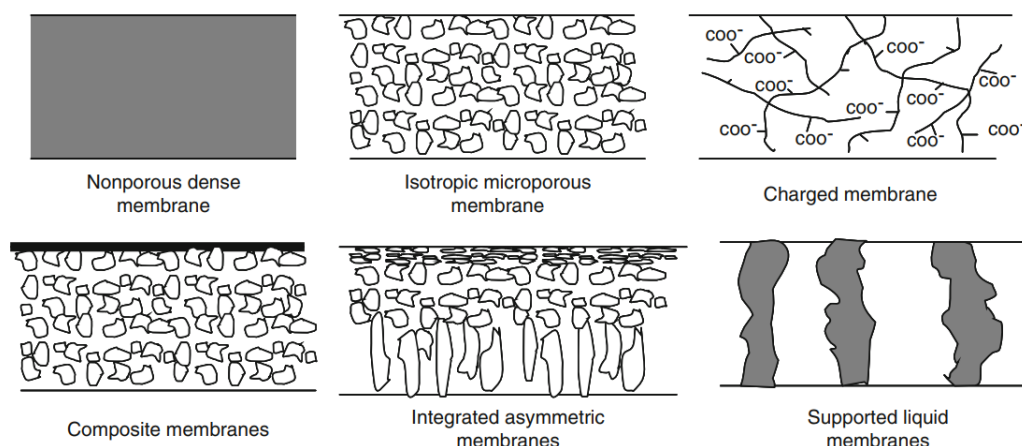


Fig. 1-5-11 Schematic diagram of different membrane morphologies [126]

1.5.5. Trends of MIEC-based oxygen separation membrane

In order to obtain a high gas separation performance, it is desirable to optimize each process from the three viewpoints of material selection, module design, and system construction as shown in Fig.1-5-12. Polymer membranes are already widely used at the industrial level, but the purity and quantity of the separation gas is not high enough. Therefore, an alternative membrane that can separate a single gas of high purity and has a high gas permeation rate is required. In a general MIEC oxygen separation membrane, the oxygen permeability depends on the temperature and shows the maximum performance at the maximum operating temperature of 900 °C. However, to use metal parts, it is desirable to reduce the operating temperature to below 700 °C [127–129]. The oxygen permeation rate is improved by reducing the thickness of the bulk diffusion-control step rather than the surface exchange reaction-control step of the membrane.

In a typical asymmetric-structured membrane fabrication process, a porous substrate with a sufficiently high mechanical strength is first prepared, and then a thin dense layer is formed on it. The thin dense layer can be formed by sol-gel, sputtering (ion beam, pulsed laser deposition: PLD), spray deposition, chemical vapor deposition (CVD), slip casting, screen printing, tape casting, dip coating, and plasma spraying method [104,130–138]. Recently, the immersion induced phase inversion method has been reported as capable of forming an asymmetric structure in a single step, which is quite efficient in terms of cost and time [139–146]. However, in the asymmetric membrane, thermal stress is generated at the interface between the porous support and thin dense layer during the co-sintering process. Thermal stress often causes cracking and peeling-off of the membrane. Therefore, matching the thermal expansion coefficients of the two layers is an important factor. The easiest and most effective way to estimate the problem is to use the same material for the thin dense layer and the porous support. Another advantage of this method is that the interfacial reaction between the two layers can be completely eliminated.

When the film thickness is small to some extent, the rate-control step of the surface exchange reaction cannot be ignored. The oxygen surface exchange reactions tend to be the rate control step due to the smooth surface of the dense free-standing membranes and insufficient reaction area. By simply roughening the surface of the free-standing membrane or forming a porous layer, the specific surface area used for the oxygen surface exchange process (adsorption, dissociation, oxidation) can be increased. In the case of the above-mentioned asymmetric structure membrane, the surface exchange reaction can be promoted by a porous layer having a large specific surface area [100–102]. Attempts have also been made to improve the surface exchange reactivity by applying a noble metal or

oxide nanoparticles having a high catalytic activity to the porous layer by the impregnation method.

In order to improve the oxygen permeability, it is necessary to improve the mixed conductivity. However, a single-component MIEC material has a limit in improving the oxide ion conductivity. One solution to improve the oxide ion conductivity is a dual-phase membrane that uses an oxygen conductor phase and an electron conductor phase material in combination as a MIEC material [84,85,93,147]. Many dual-phase membranes in which materials used metals and oxides as the electron conductor phase have been developed. In particular, it has been suggested that two-phase films using a precious metal as the electron conductor phase have a high surface activity.

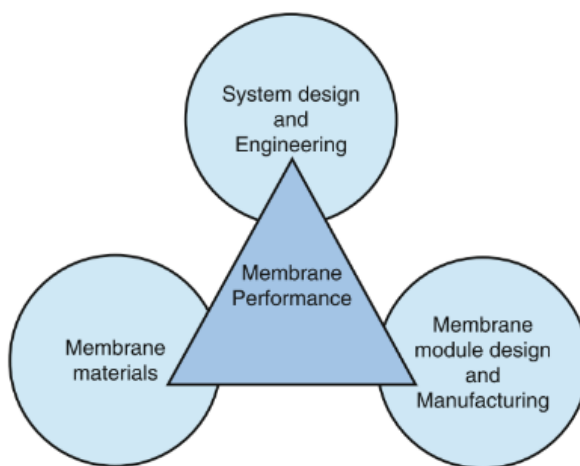


Fig.1-5-12 Three viewpoints for improvement of membrane performance [148]

1.6. Ceramics Processing

1.6.1 Importance of ceramics processing

Ceramics have a long history and ceramic products have progressed from traditional ceramic technology to fine ceramics in recent years. Globally, fine ceramics were systematically developed in Japan, the United States, and Europe just half a century ago, and the industrial history is shorter than that. However, fine ceramics have various functions and are an essential material that supports modern advanced industries such as electronics, semiconductors, information and communications, aviation and space, environment and energy, automobiles, medicine, and biotechnology. Ceramics have very excellent properties, such as high strength, high corrosion resistance, wear resistance, and heat resistance, and various functional ceramic materials have attracted attention. In ceramic processing to form such materials, various processes, such as mixing, molding, firing, and processing, are performed from raw materials to products. The processing of fine ceramics has a number of important factors to optimize related to the materials, shapes, applications, and manufacturing methods. In recent years, the demands for ceramic products having a small size and a complicated shape due to technological progress have been increasing. Ceramic sintered bodies are extremely difficult to finish, such as polishing and cutting, and a high-precision molding method that can produce near net shapes that can produce final products by light finishing close to the final product at the molding stage is required. In addition, in order to improve the product reliability and maximize the functionality of materials, it is necessary to design an organizational structure suitable for each application, select a process to realize it and optimize the process parameters [149–158].

1.6.2 Colloid processing

In the ceramic manufacturing process, a product is completed through various processes such as powder synthesis, pulverization, mixing, molding, firing and finishing. Regarding the mixing and forming process after the synthesis of the powder, in general, nonhomogeneous portions in the sample, such as density gradients and cracks, at the time of forming are factors that cause defect structures, and deformations and cracks at the time of firing. As a result, the various properties of the material are impacted, and the reliability and reproducibility are reduced during the production of ceramics. Therefore, in order to obtain a homogeneous ceramic compact from the powder, it is necessary to establish a process that has better control of the structure than conventional powder processes. In addition, it is difficult to process hard and brittle ceramic samples after sintering, and there is a need to establish a near-net shaping method that can produce compacts close to the target shape. Ceramic forming methods are roughly classified into two types; i.e., colloidal and dry. In the dry process, the main forming method is to fill a mold with the synthesized and milled powder and press it to produce a compact. A feature of this method is that a green compact can be obtained simply by filling powder into a mold, and mass production is possible. However, it is difficult to uniformly fill the powder. When the filling rate of the powder is not uniform, a defect structure is introduced into the sample. It also requires a sufficient film thickness [153,158–160].

The colloid process is a method to perform solidifying and shaping from a colloidal suspension. By controlling the interaction between particles and then solidifying the dispersed particles in the liquid, it is possible to produce compacts with a controlled

microstructure. Compared to the dry method, the colloidal method can control the microstructure and produce a homogeneous and high-density compact body. In order to ensure high dispersibility and fluidity of the particles in the liquid, it is necessary to select a solvent, dispersant, binder, and optimize the ionic strength, i.e., the pH. Furthermore, the colloid process has a problem that it takes more time to solidify particles in a suspension and is not suitable for mass production as compared to the conventional dry process [161–166].

Figure1-6-1 and Table1-6-1 show a typical solidification method using a colloid process. The slip casting method is the most widely-used method among the colloidal processes. In this method, a solidified body can be produced by pouring the suspension into a porous mold having a hygroscopicity, such as gypsum, and allowing the mold to absorb the solvent by capillary force. In centrifugal molding, a centrifugal force is applied to the slurry, and then particles in the liquid are deposited in the direction of the centrifugal force. Tape casting is a method in which the suspension flows out from the knife edge of a doctor blade, and the carrier film with the suspension is moved while receiving it on the blade to form a tape. It is often applied to the production of a laminated film. Electrophoretic deposition (EPD) is a method in which charged particles in a liquid are electrophoresed on an electrode substrate immersed in an electric field and deposited onto the substrate. In this method, the solidification rate does not depend on the particle size, and a high-density deposited layer can be obtained. Furthermore, the EPD method is easy to control the film thickness and has an excellent laminated film-forming property. Moreover, by applying an external field, such as a magnetic field, the particle arrangement can be controlled, which is suitable for the production of ceramic higher-order structures.

Table 1-6-1 Classification of solidification methods in colloidal processes [167]

| Method | Acting force | Material | |
|--|--|----------------------------|---------------------|
| | | Stationary object | Moving object |
| Slip casting | Capillary force | Particle Ion | Solvent |
| Filtration under pressurization or decompression | Compression force Suction force | Particle Ion | Solvent |
| Centrifugal molding | Centrifugal force | Ion | Solvent Particle |
| Tape casting | Blade shear force Crosslinking power of polymer | Solvent Particle Ion | - |
| Electrophoretic deposition | Electrohydrodynamics Electrochemical | Solvent | Particle Ion |

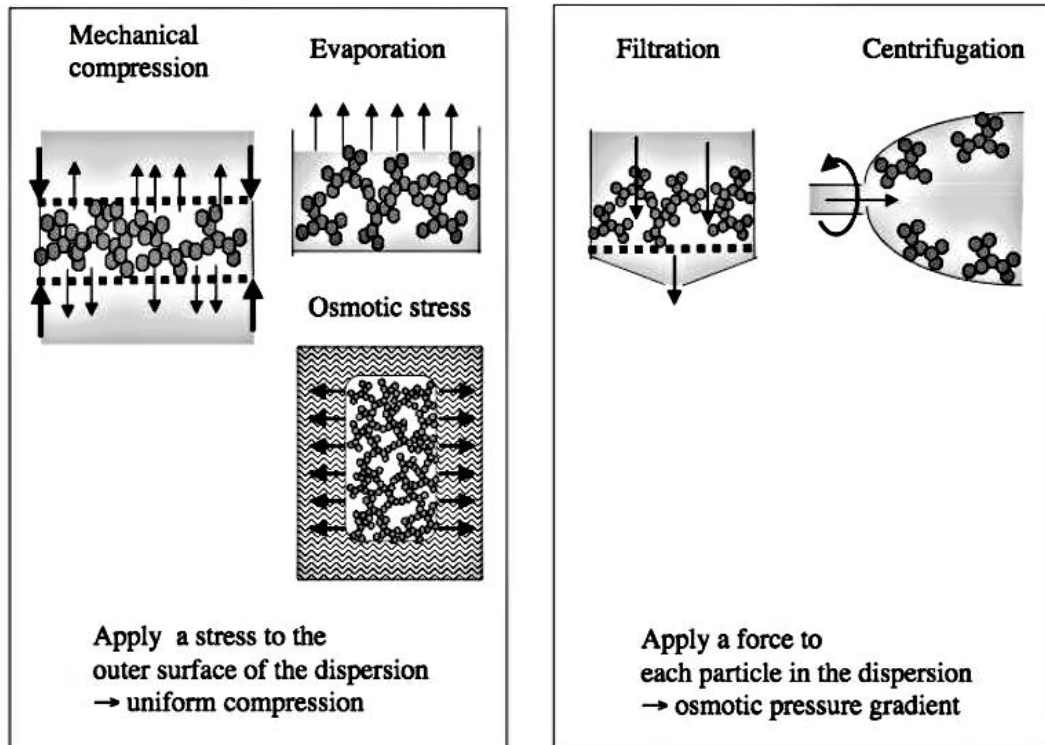


Fig. 1-6-1 Solid-liquid separation technique [168]

1.6.3. Colloid dispersion system

A colloidal dispersion system is a state in which colloidal particles are uniformly suspended in a dispersion medium. Colloidal particles are fine particles having a scale of about $1\text{nm}(10^{-9}\text{m})$ - $1\mu\text{m}(10^{-6}\text{m})$, which is larger than atoms and low molecular weight molecules and small enough not to immediately settle due to gravity. As shown in [Table 1-6-2](#), the colloidal system has various names depending on the combination because the dispersoid and the dispersion medium can be any of gas, liquid, and solid. When a solid is the dispersoid and a liquid is the dispersion medium, such a colloidal system is called a suspension or a slurry.

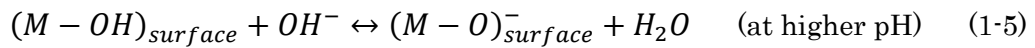
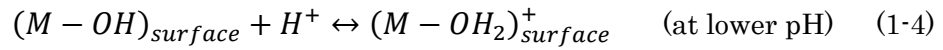
Table 1-6-2 Classification of colloids

| Dispersion phase | Dispersion medium | Colloidal type | Example |
|------------------|-------------------|----------------|-------------------------|
| Gas | Gas | - | - |
| Liquid | Gas | Liquid aerosol | Mist, Clouds, Fog |
| Solid | Gas | Aerosol | Dust, Smoke |
| Gas | Liquid | Foam | Suds, Whipped cream |
| Liquid | Liquid | Emulsion | Cream, Milk, Mayo |
| Solid | Liquid | Sol | Paints, Jellies, Sewage |
| Gas | Solid | Solid foam | Marshmallow, Cake |
| Liquid | Solid | Solid emulsion | Butter, Cheese |
| Solid | Solid | Solid sol | Colored Glass, Opal |

Dispersion colloids are systems in which particles of an insoluble material are dispersed in a medium, and are clearly distinguished from solutions of soluble materials. For example, crystalline and powdered sodium chloride (NaCl) and sucrose ($\text{C}_{12}\text{H}_{22}\text{O}_{11}$) are not colloidal particles because they dissociate and dissolve into Na^+ and Cl^- ions and glucose and fructose in water. A solution is a state in which crystals are dissolved in a solvent and dissociated to the level of atoms and molecules that are constituent units of the substance. A colloid, on the other hand, is a state in which a large number of atoms and molecules are gathered to form one particle, which is dispersed in a medium. Thus, in the colloidal dispersion system, since the dispersion medium and the dispersed phase are distinct phases, an interface is formed in the system. When the dispersed particles are very small, the ratio of the specific surface area of the dispersed particles to the total volume becomes very large. At that time, the properties of the interface become dominant over the properties of the whole material system. In general, the surface of the particles has a high energy, and the particles tend to aggregate in order to stabilize the entire system. The movement of coarse particles, such as bulk particles, in the solvent is determined by the sedimentation velocity (Stokes viscosity) due to the balance between gravity and floating power. On the other hand, colloidal particles are constantly moving due to Brownian motion caused by the collision between particles and solvent molecules due to thermal motion. In particular, when the particles in the liquid are sufficiently small, any thermal disturbance inhibits the sedimentation of the particles, so that the particles are always suspended in the liquid without sedimentation [169–171].

1.6.4. Electric double layer of colloidal particles in aqueous system

Factors that determine the dispersibility of the suspension include the surface condition of the powder and the interaction between the particles. [Figure1-6-2](#) shows the charged state of an oxide particle surface in an aqueous solvent. Generally, when colloidal particles, such as oxide particles, are added to an aqueous dispersion medium, hydroxyl groups are formed on the surface by a hydration reaction as expressed by the following equations [\[172\]](#).



The surface of the oxide particle is positively or negatively charged by the adsorption/dissociation of protons to the hydroxyl group. For this reason, the charged state of the oxide particles significantly depends on the pH of the solvent. On the acidic side, the surface is positively charged due to the addition of protons to the surface hydroxyl groups. On the other hand, when the pH is basic, protons are extracted from the surface hydroxyl groups, and the surface is negatively charged. When the particle surface is not charged either positively or negatively, the pH is called the point of zero charge (PZC). If the surface is partially positively or negatively charged but the overall particle balance is the same at both sites and the surface is apparently not charged; this state is called the isoelectric point (IEP). The IEP varies not only with the pH but also with the materials and additives [\[165,173–175\]](#).

In the vicinity of the surface of the charged particles in the solvent, there are many

counter ions having a charge opposite to the surface charge compared to the co-ions having the same polarity. This is because a repulsive or attractive Coulomb force acts between the surface-charged particles and ions in the solvent. At absolute zero (0 K), counter ions are adsorbed on the particle surface to neutralize the particle charge. However, at temperatures higher than absolute zero, the electrostatic attraction is hindered by the thermal motion of the ions, so that the counter ions form a broad distribution. This space in which ions are distributed is called the electric double layer. The types of counter ions and co-ions and their degree of dispersion depend on the solvent, additives and electrolyte, such as an acid and base, used for pH adjustment. The degree of diffusion of the electrolyte, such as the counter ions and co-ions, is expressed by $1/\kappa$ (Debye length) indicating the thickness of the electric double layer. This thickness is the distance at which the attractive force between the surface charge and the counter ion balances the thermal motion that prevents it. κ is called Debye-Hückel parameter and is expressed by the following equation.

$$\kappa = \sqrt{\frac{(2\pi n z^2 e^2)}{\epsilon_0 \epsilon_r k T}} \quad (1-6)$$

where z is the valence of the symmetric electrolyte, k is the Boltzmann constant, ϵ_0 is the dielectric constant of the vacuum, ϵ_r is the relative permittivity of the solvent, T is the absolute temperature, e is the unit charge, and n is the number density of the electrolyte. κ^{-1} plays a crucial role in the zeta potential and the stability of distributed systems. This will be described later.

Figure1-6-3 shows a schematic diagram of the structure of the electric double layer when the particle surface is positively charged and the corresponding potential

distribution [176–180]. In the first layer on the particle surface, there is a Stern layer in which counter ions are strongly attracted and fixed. On the outside, there is a diffusion layer in which counter ions and co-ions are mixed. When an external electric field is applied, the charged particles move with the Stern layer and some diffusion layers. At this time, the boundary surface on which particles can move with ions is called a slipping plane. When the potential of the electrically neutral region far from the particle is 0, the potential at the slipping plane is called the zeta potential. In many cases, the zeta potential, which is the potential at the slipping plane, is treated as an approximate value of the potential (ψ_o) at the Stern plane. The zeta potential is an important factor for evaluating the dispersion stability of particles.

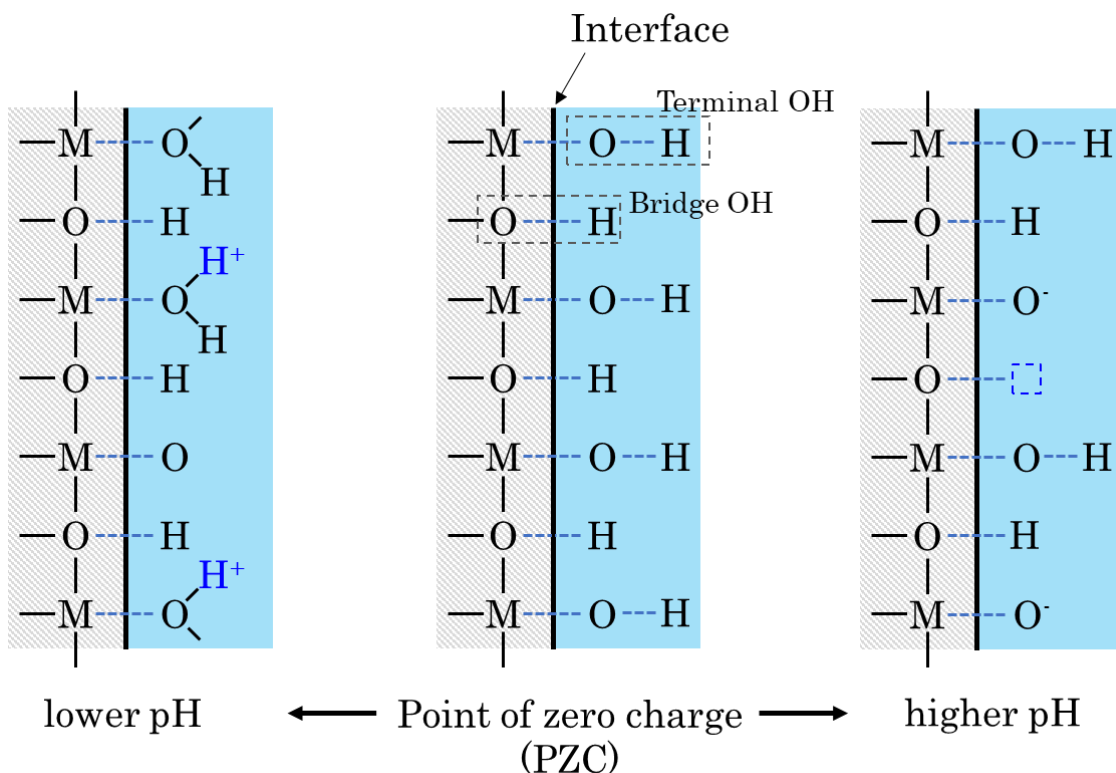


Fig1-6-2 pH dependence of the surface of metal oxide in water

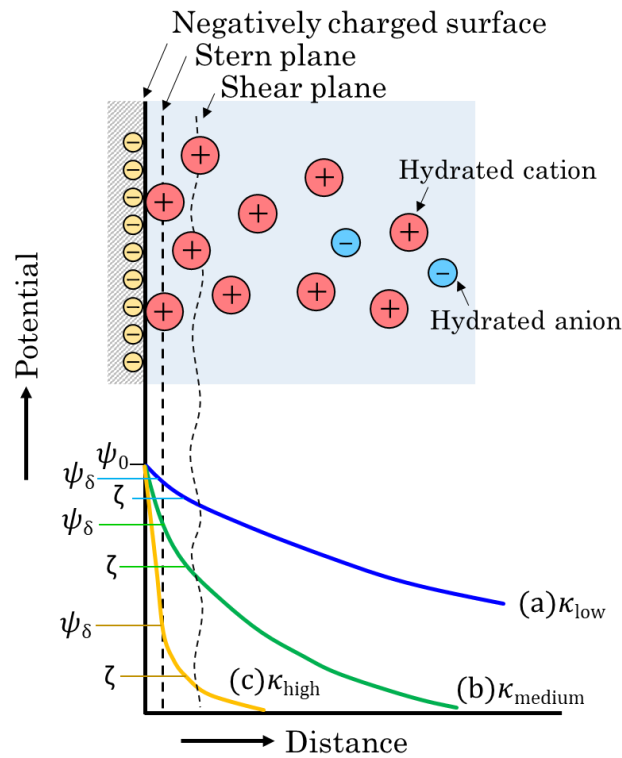


Fig. 1-6-3 Electric double layer of water system by Stern model

1.6.5. Nonaqueous system

In aqueous systems, even if deionized water is used, water is dissociated and protons and hydroxide ions are generated, so the ionic strength cannot be completely reduced to 0 (10^{-7} or less). The dielectric constant of a nonaqueous solvent is generally small, and the ionic strength is also low. In the above-described equation (1-6) representing the Debye parameter κ , n and ϵ_r are the factors that differentiate between the aqueous system and the nonaqueous system. The change in n is generally different in number of digits compared to the change in ϵ_r , and as a result, κ is very low in nonaqueous systems. In other words, the electric double layer considerably spreads in the solvent. Therefore, the change of the electric double layer in the nonaqueous system is often as shown in a

and b in Fig.1-6-3. When the ionic strength is high, the curve becomes (c). As described above, in the electrophoresis process, it is necessary to charge the particle surface positively or negatively, and it is difficult to prepare a stable suspension having a high zeta potential by simply putting particles in a solvent and stirring them. Therefore, generally, after the powder is put into a solvent, an appropriate amount of acid, alkali or polymer electrolyte is added to charge the particles. The acidity dependence of the zeta potential is one of the very important evaluation factors as a suspension evaluation method [161]. In general, the acidity in an aqueous solvent is represented by the hydrogen ion concentration index $\text{pH} = -\log[\text{H}^+]$. In nonaqueous solvents, lower alcohols and ketones that are readily miscible with water can be easily evaluated using a normal pH electrode. The acidity of the nonaqueous solvent is defined by the following equation in which the hydrogen ion concentration is replaced by the activity of proton a_H .

$$\text{p}a_H = -\log a_H \quad (1-7)$$

$$\mu_H = \mu_H^\circ + RT \ln a_H \quad (1-8)$$

when the acidity of the nonaqueous solvent is measured with a normal pH electrode (KCl electrolyte) calibrated for aqueous solvents, the following relational expression holds between the pH meter reading pH_{op} (operational pH) and a_H :

$$\text{pH}_{op} - \text{p}a_H = \frac{\Delta E_j}{\left(\frac{RT \ln 10}{F}\right)} \quad (1-9)$$

or

$$\text{pH}_{op} - \text{p}a_H = \frac{\Delta E_j}{(0.05916)} \text{ at } 25^\circ\text{C} \quad (1-10)$$

Here, ΔE_j is a residual liquid junction potential, R is the gas constant, and F is the Faraday constant. When the solvent is ethanol, it is represented by the following formula.

$$pH_{op} = pa_H + 1.23 \quad (1-11)$$

Since the pH measurement is useful data for suspension evaluation, it should be measured regardless of whether it is aqueous or nonaqueous. However, it should be noted that a completely anhydrous solvent cannot obtain an accurate value because the glass membrane of the measurement electrode is dehydrated and the impedance increases.

1.6.6. Dispersion and aggregation mechanism of colloidal particles in aqueous solvents (DLVO theory)

The DLVO (Derjaguin-Landau-Verwey-Overbeek) theory is about theory on the stability of colloidal dispersion systems based on the interaction of the electric double layer when two particles approach in a liquid [181,182]. Figure1-6-4 shows the relationship between the distance between two particles in the suspension and the interaction potential of the electric double layer. When one particle surface is at the origin and the other particle approaches from infinity, the repulsive force due to the overlapping of the electric double layer is V_R , and the van der Waals attractive force, which is the sum of the intermolecular attractive forces, is V_A . The energy of van der Waals attraction V_A between two homogeneous spherical particles of radius a is expressed by the following equation as a function of the interparticle distance D . ($D \ll a$)

$$V_A(D) = -\frac{Aa}{12D} \quad (1-12)$$

Here, A is the Hamaker constant, which macroscopically determines the van der Waals force between materials. The electrostatic repulsive force acting between two particles is expressed by the following equation using the Derjaguin approximation.

$$V_R(D) = \frac{64\pi\epsilon_0 k T \gamma^2}{\kappa^2} \exp(-\kappa D) \quad (1-13)$$

The interaction energy V_T acting between particles is the sum of the attractive force and repulsive force and is expressed by the following equation:

$$V_T = V_R + V_A \quad (1-14)$$

A typical V_T potential curve given by this equation is shown in [Figure1-6-4](#). In the V_T curve, there is a potential barrier (E_B) that prevents particles from approaching. In a system with a low E_B , the thermal motion energy of particles is higher than that of E_B , resulting in the aggregation of adjacent particles by the van der Waals attractive force. Therefore, in order to improve the dispersibility, it is necessary to increase V_{max} , that is, the surface potential.

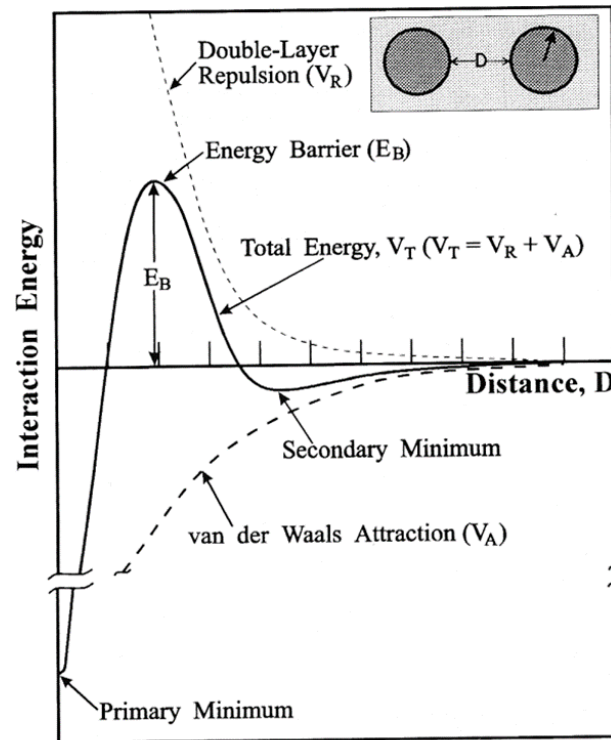


Fig. 1-6-4 Schematic of the interaction energy as a function of separation between two particles in a suspension. [183]

1.6.7. Theory of electrophoresis phenomenon

Electrophoresis is generally known as one of the properties of colloidal particles. The electrophoresis is a phenomenon of the movement of charged particles in a solvent by an applied electric field [179,184–187]. It is assumed that there is an electric double layer on the solvent side of the solid/liquid interface, and a DC electric field E is applied in a direction parallel to the interface. At that time, since the solid surface is stationary and laminar flow is generated on the solvent side, a velocity distribution is formed from the interface to the solvent side. Furthermore, assuming a microcube in the solvent, the electric attractive force and the viscous resistance acting on the cube must be balanced

in a steady state. When the average charge density in the cube is ρ , the electric force is ρE , which is balanced by the viscous force ($\eta d^2u/dx^2$) in the steady-state as shown by the following equation.

$$\rho E = \eta \frac{d^2u}{dx^2} \quad (1-15)$$

where u is the relative velocity between the interface or particle and the solvent and is the mobility of electrophoresis. Substituting Poisson's equation into this relation and integrating both sides twice, the following equation is obtained.

$$V = \left(\frac{\varepsilon_0 \varepsilon_r}{\eta} \right) \phi_0 E \quad (1-16)$$

Therefore, the electrophoretic mobility $u = V / E$ is expressed by the following equation.

$$u = \left(\frac{\varepsilon_0 \varepsilon_r}{\eta} \right) \zeta \quad (1-17)$$

Here, η is the viscosity. Furthermore, the surface charge ϕ_0 is replaced with the zeta potential ζ . This equation is called Smoluchowski's equation and is the most widely used electrophoresis equation. Smoluchowski's equation is derived for a flat plate, but this equation can apply to cylindrical particles with a large radius and spherical particles with a particle radius (a) larger than the electric double layer thickness ($1/\kappa$): $a \gg 1/\kappa$. It is an extremely useful formula because it can be applied to relatively large particles of any shape. Furthermore, the equation when the external electric field acts on the point

charge is expressed by the following equation, it is called the Hückel's equation. The Hückel's equation can be applied to the case where the particle radius a is small and the limit of the electric double layer is $a \ll 1/\kappa$.

$$u = \frac{2\varepsilon_0\varepsilon_r\zeta}{3\eta} \quad (1-18)$$

Here, the unit of u is $[\mu m V^{-1} s^{-1} cm]$. The Hückel's equation differs from the Smoluchowski's equation in that it has a factor of $2/3$. Therefore, the zeta potential calculated by the Hückel's equation is 1.5 times higher than that calculated by the Smoluchowski's equation. The difference between these equations is that the Smoluchowski's equation takes into account the distortion of the electric field due to the presence of particles, whereas the Hückel's equation ignores the distortion of the external electric field due to its very small particles. Henry defined this electric field distortion as a function of κa . Henry also took into account the effect of moving in the liquid (delay effect) and derived the following equation:

$$u = \left(\frac{\varepsilon_0\varepsilon_r}{\eta} \right) \zeta \cdot f(\kappa a) \quad (1-19)$$

Here, the function $f(\kappa a)$ is called the Henry coefficient and represents the degree of distortion of the external electric field due to the presence of particles. The Henry's coefficient is $f = 2/3$ when $\kappa a \rightarrow 0$, and the Hückel equation is explained using the Henry equation. On the contrary, the Henry coefficient is $f = 1$ from $\kappa a \rightarrow \infty$, and Smoluchowski's equation is explained by the Henry equation. In this limit, the external

electric field is completely distorted. The zeta potential, which is an important factor for evaluating the dispersion/aggregation state of colloidal particles, is calculated by applying an electric field in the solvent and measuring the electrophoretic mobility u of the particles migrating in the electric field.

1.6.8. Electrophoretic Deposition Process (EPD)

Electrophoresis is known as one of the characteristics of colloids. Electrophoresis is a phenomenon in which a charged substance in a solvent moves due to an electric field [172,188–194]. Electrophoresis can detect a difference in the molecular weight of DNA or a protein as a difference in mobility, and is often used as an analysis method in molecular biology and biochemistry. On the other hand, the electrophoretic deposition (EPD) method is a processing technique in which charged particles in a solvent are electrophoresed and then directly deposited on an electrode substrate as shown in Fig1-6-5. The EPD method is classified as colloid processing, and its feature is that it is easy to produce a dense film with a uniform thickness controlled even on a complex-shaped electrode substrate. In the industrial field, the EPD method has been applied to a method for the understanding of a vehicle body and has been frequently used as a method for forming a ceramic film in various products as shown in Table1-6-3. The particle deposition process by EPD mainly consists of the following two steps: Electrophoresis of charged particles onto a substrate by an electric field and particle deposition on the substrate. The rate-controlling step of EPD is not the electrophoresis but the process of depositing particles on the electrode. The accumulation of particles reaching the substrate means that the particles aggregate on the substrate, and the charge of the

particles themselves and the repulsive force between the particles must be lost. De and Nicholson et al. performed the EPD of alumina particles dispersed in an acidic ethanol solvent. The concentration of protons as charge carriers locally decreases around the negative electrode substrate. Since the pH in the vicinity of the electrode is close to that of the alumina IEP, particles that migrate to the vicinity of the electrode substrate rapidly lose their electrostatic repulsion. As a result, migrating particles are aggregated and deposited by van der Waals attraction beyond the potential barrier. For such a mechanism, a pH localization model has been proposed as shown in Fig.1-6-6.

In a general colloid process, an aqueous system is often used as the solvent because of its low cost, low environmental burden, and ease of dispersion control. Although an aqueous solvent can be used in the electrophoresis process, a nonaqueous solvent is often used in order to avoid the porous formation of deposits due to gas generated by electrolysis of water at the electrode.

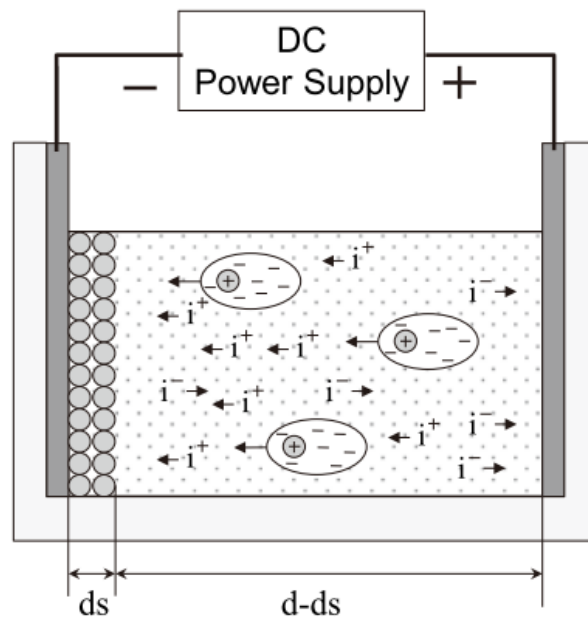


Fig.1-6-5 Electrophoresis and deposition of ions and particles in a suspension [195]

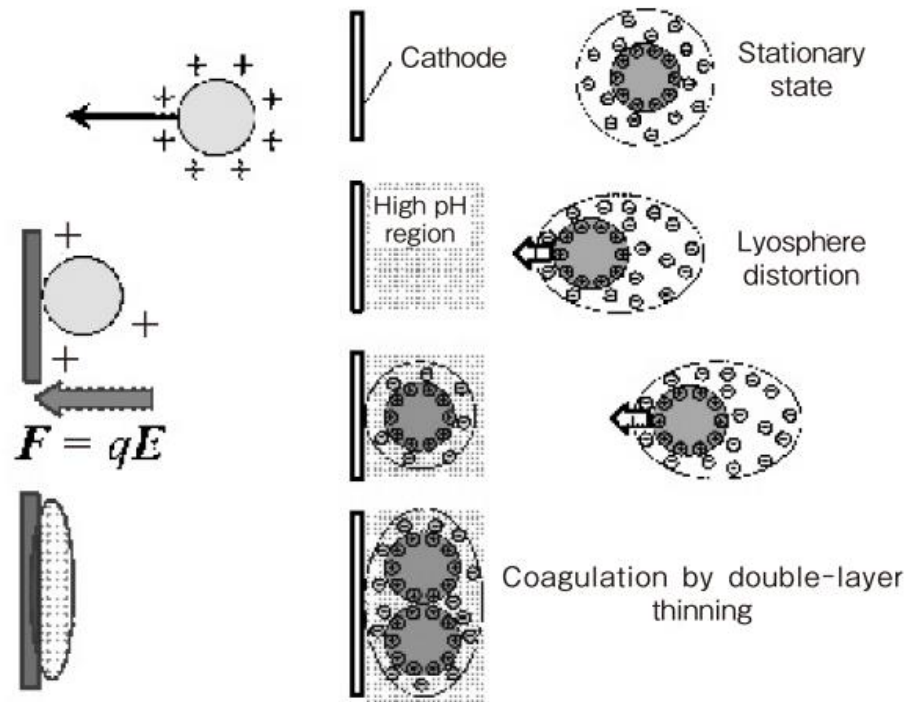


Fig.1-6-6 Schematic diagram of particle solidification by three effects by electric field and pH localization model [183]

As shown in Table1-6-4, the electrophoretic deposition method can obtain the desired deposit by optimizing the EPD conditions according to various parameters. In addition, as shown in Fig.1-6-7, one of the features of EPD is that the applicable film thickness is wider than other film forming methods.

Table1-6-3 Advantages and disadvantages of EPD [196]

| Advantages |
|--|
| <ul style="list-style-type: none"> • Low manufacturing cost (Simple equipment and instruments) • Rapid film formation of uniform and high quality particle layers • Easy film thickness control (Applied voltage or current, Deposition time, Suspension concentration) • Capable of film formation on conductive substrates with complex shapes • Easy to scale up to manufacturing industry • Green process using aqueous solution |
| Disadvantages |
| <ul style="list-style-type: none"> • Electronic conductivity is required for electrode substrate • Heat treatment is required to densify the deposit |

Table1-6-4 Operating factors of electrophoresis [196]

| | Object | Operating Factors |
|------------------------|-----------|---|
| Suspension | Powder | Material: Metal, Ceramics, Polymer Particle property: Shape, Size, Distribution Amount |
| | Solvent | Type: water, Nonaqueous pH value: Acidic, Alkalinity, Neutral Type and amount of dispersant |
| Electrophoresis | Electrode | Material, Size, Shape, Surface condition, Geometric arrangement, Electrode distance |
| | Condition | Constant voltage or Constant current, Deposition time, Stirring, Temperature, Surface charge of power |

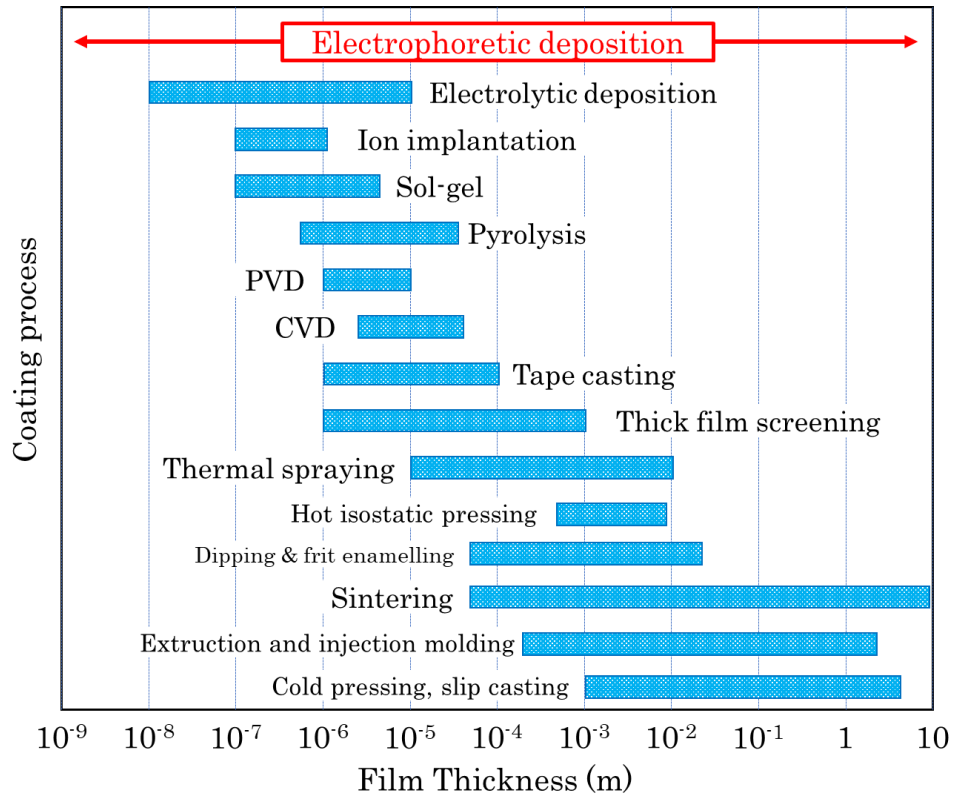


Fig.1-6-7 Typical thickness of coatings applied by different processes [195,197]

1.7. Purpose of this study

An oxygen separation membrane using a mixed oxide ionic-electronic conductor (MIEC) is an electrochemical device that can selectively separate only oxygen from air by the permeation of oxide ions due to the partial pressure difference of oxygen. In order to improve the oxygen separation efficiency, it is necessary to improve the surface exchange reactivity in which oxygen molecules dissociate into oxide ions and the oxide ions associate into oxygen molecules, and the bulk diffusivity through which the oxide ions permeate in the membrane. In designing an MIEC oxygen separation membrane, it is necessary to select the membrane structure, geometric shape, film formation method, etc., according to the application. In particular, progress has been made to improve the

oxygen separation efficiency from simple dense self-supporting membranes to multi-layered membranes composed of a porous layer / dense layer / porous support. Also, the same material is used for all layers in order to minimize the reaction between each layer, and thermal stress during co-firing. In the film formation technique, various types of membranes have been produced by many film formation methods according to applications. The problem with coating methods, such as tape casting, which is most commonly used for lamination and film formation, is that many binders are required, and structural defects are likely to form in the dense layer after sintering. Also, with this method, it is difficult to form a good adhesion at the interface between the dense layer and the porous layer, and the applicable module target is limited to a flat-plate type.

In this study, we focused on electrophoretic deposition (EPD), a colloidal deposition method in liquids. There are not many cases where the EPD method is applied to electrochemical cells, such as oxygen separation membranes, compared to other film forming methods. Since the MIEC has a high electron conductivity at room temperature, the pre-made porous support layer can be directly used as an electrode for the EPD film formation. Therefore, when the EPD method is applied to the fabrication of the MIEC oxygen separation membrane, it is considered that an EPD layer having a good adhesion can be formed on the surface of the porous support having a complicated shape. Furthermore, when the porous layer is formed by the EPD method, the porous layer may be formed by co-depositing and firing the base material particles and the pore former particles. However, there are very few examples of EPD using a two-component slurry. The purpose of this study was to investigate the process parameters in order to form a dense layer and a porous layer on a porous support by the EPD method and to apply the EPD process to the multi-layered oxygen separation membrane.

References

- [1] BP p.l.c. 2019, BP Energy Outlook: 2019 edition, 2019.
- [2] International Energy Agency, World Energy Outlook 2019 The gold standard of energy analysis, (2019). <https://www.iea.org/weo2019/> (accessed November 4, 2019).
- [3] International Energy Agency, Key world energy statistics, 2019.
- [4] International Renewable Energy Agency, Global Energy Transformation. A Roadmap to 2050, 2019.
- [5] U.S. department of E. U.S. Energy Information Administration, Office of Energy Analysis, International Energy Outlook 2019with projection to 2050, 2019. <https://doi.org/https://www.eia.gov/outlooks/ieo/pdf/ieo2019.pdf>.
- [6] J. The Institute of Energy Economics, 2017 International Energy Situation Survey (Investigation projects on energy policy trends and international energy statistics in other countries) Research report on energy policy trends in other countries - Survey commissioned by the Agency for Natural R, 2018.
- [7] United Nations Development Programme, World Energy Assessment, energy and the challenge of sustainability, 2000.
- [8] T.B. Johanson, A. Patwardhan, N. Nakicenovic, L. Gomez-Echeverri, Global Energy Assessment Toward a Sustainable Future, 2012.
- [9] Statkraft AS, 2019 Global energy trends, Statkraft's low Emissions Scenerio, 2019.
- [10] J.N. CAPE, Air Pollution, in: M. Campbell (Ed.), Sens. Syst. Environmetal Monit., Chapman & Hall, n.d.: pp. 107–143.

- [11] L.K. Wang, N.C. Pereira, Y.-T. Hung, eds., *Air Pollution Control Engineering*, Human Press, 2013. <https://doi.org/10.1017/CBO9781107415324.004>.
- [12] K.B. Schnelle, R.F. Dunn, M.E. Ternes, eds., *Air pollution control technology handbook*, Second Edi, CRC Press, 2016. [https://doi.org/10.1016/s0304-3894\(02\)00253-4](https://doi.org/10.1016/s0304-3894(02)00253-4).
- [13] S. Mosley, *Environmental History of Air Pollution and Protection*, in: M. Agnoletti, S.N. Seneri (Eds.), *Basic Environ. Histry, Environ. Histary 4*, Springer, Switzerland, 2014: pp. 143–169. https://doi.org/10.1007/978-3-319-09180-8_5.
- [14] J. Puhe, B. Ulrich, *4 Sources and Sinks of Greenhouse Gases and Air Pollutants*, Springer-Verlag Berlin Heidelberg, 2001.
- [15] R.M. Macky, M.A.K. Khalil, *Greenhouse Gases and Global Warming*, in: S.N. Sigh (Ed.), *Mak. Technol. Work*, Kluwer Academic Publishers, 2000: pp. 1–28. <https://doi.org/10.1017/cbo9780511616358.007>.
- [16] K. Chatterjee, *Causes of Greenhouse Gas Emissions*, in: P. Martens (Ed.), *Clim. Chang. An Integr. Perspect.*, Kluwer Academic Publishers, 1999: pp. 143–200. https://doi.org/10.1007/0-306-47982-6_5.
- [17] Z. Zhang, J. Qu, J. Zeng, *A quantitative comparison and analysis on the assessment indicators of greenhouse gases emission*, *J. Geogr. Sci.* 18 (2008) 387–399. <https://doi.org/10.1007/s11442-008-0387-8>.
- [18] P. Krugman, *Othter Greenhouse gases*, in: W.W. Hay (Ed.), *Exp. a Small Planet*, Springer, 2016. <https://doi.org/10.1007/978-3-319-27404-1>.
- [19] C. Bessou, F. Ferchaud, B. Gabrielle, B. Mary, *Biofuel, Greenhouse Gases and Climate Change*, *Sustain. Agric.* 2 (2011) 365–468. <https://doi.org/10.1051/agro>.

- [20] V.F. Krapivin, C.A. Varotsos, V.Y. Soldatov, Ecoinformatics Problems of Global Climate Change, in: *New Ecoinformatics Tools Environ. Sci. Environ. Earth Sci.*, 2015: pp. 355–486. <https://doi.org/10.1007/978-3-319-13978-4>.
- [21] H. Harvey, R. Orvis, J. Rissman, *Designing Climate Solutions*, Island press, 2018. <https://doi.org/10.5822/978-1-61091-957-9>.
- [22] G.A. Meehl, C. Tebaldi, More intense, more frequent, and longer lasting heat waves in the 21st century, 2004. <https://doi.org/10.1126/science.1098704>.
- [23] J. Lemons, R. Heredia, D. Jamieson, C. Spash, CLIMATE CHANGE AND SUSTAINABLE DEVELOPMENT, in: J. Lemons, D.A. Brown (Eds.), *Sustain. Dev. Sci. Ethics, Public Policy*, Kluwer Academic Publishers, 1995: pp. 110–157.
- [24] P.C. Villasis, the 21st Century climate challenge, in: *Hum. Dev. Rep. 2007/ 2008*, 2008: pp. 20–69.
- [25] D.J. Wuebbles, Global Climate Change due to Radiatively Active Gases, in: C. N. Hewitt et al. (Ed.), *Glob. Atmos. Chem. Chang.*, Elsevier Science Publishers Ltd., 1993: pp. 53–92. https://doi.org/10.1007/978-94-015-3714-8_2.
- [26] S. Radiation, H. Balance, *ASSESSING CLIMATE CHANGE*, Third Edit, Springer, 2014.
- [27] C.S. Hsu, P.R. Robinson, Safety and environment, in: *Pet. Sci. Technol.*, Springer Nature Switzerland AG 2019, 2013: pp. 619–652. https://doi.org/10.1007/978-1-4471-5556-0_12.
- [28] U.S.I.T. Administration, *2016 Top Markets Report Smart Grid Country Case Study*, 2016.
- [29] United States Department of Energy, *Smart Grid System Report*, 2018.
- [30] MI Smart Grids, *Smart Grids Innovation challenge Country Report 2017*, 2017.

- [31] A. Poh, A. Ling, The Japanese Smart Grid Initiatives , Investments , and Collaborations, *Int. J. Adv. Comput. Sci. Appl.* 3 (2012) 44–54.
<https://doi.org/10.14569/IJACSA.2012.030706>.
- [32] A. Catalin, F. Covrig, M. Ardelean, J. Vasiljevska, M.S. Jiménez, C. Filiou, D.G. Ener, *Smart Grid Projects Outlook 2014*, 2014. <https://doi.org/10.2790/22075>.
- [33] M. Bui, C.S. Adjiman, A. Bardow, E.J. Anthony, A. Boston, S. Brown, P.S. Fennell, S. Fuss, A. Galindo, L.A. Hackett, J.P. Hallett, H.J. Herzog, G. Jackson, J. Kemper, S. Krevor, G.C. Maitland, M. Matuszewski, I.S. Metcalfe, C. Petit, G. Puxty, J. Reimer, D.M. Reiner, E.S. Rubin, S.A. Scott, N. Shah, B. Smit, J.P.M. Trusler, P. Webley, J. Wilcox, N. Mac Dowell, Carbon capture and storage (CCS): The way forward, *Energy Environ. Sci.* 11 (2018) 1062–1176.
<https://doi.org/10.1039/c7ee02342a>.
- [34] R.E. Ayala, Application of IGCC Technology to Power Generation, in: A.T. Atimtay, D.P. Harrison (Eds.), *Desulfurization Hot Coal Gas*, Springer-Verlag Berlin Heidelberg, 1998: pp. 75–101. https://doi.org/10.1007/978-3-642-58977-5_5.
- [35] S. Srinivasan, C. Yang, Competing Technologies, in: *Fuel Cells*, 2006: pp. 607–661. https://doi.org/10.1007/0-387-35402-6_11.
- [36] P. Coca, M. Perez-Fortes, A.D. Bojarski, Examples of industrial Applications, in: L. Puigjaner (Ed.), *Syngas from Waste Emerg. Technol.*, Springer-Verlag London, 2011: pp. 277–297. <https://doi.org/10.1007/978-0-85729-540-8>.
- [37] R.W. Smith, S.C. Gu, Natural Gas Power, in: R. Malhotra (Ed.), *Foss. Energy Sel. from Encycl. Sustain. Sci. Technol.*, Springer Science+Business Media, 2012: pp. 527–594. <https://doi.org/10.1007/978-1-4419-0851-3>.

- [38] A. Minchener, Coal and Clean Coal Technology: Challenges and Opportunities, in: H. Qi, B. Zhao (Eds.), Clean. Combust. Sustain. World, Springer-Verlag Berlin Heidelberg, 2013: pp. 3–10. <https://doi.org/10.1007/978-3-642-30445-3>.
- [39] C.E.S. Thomas, Electricity Generator Costs and Greenhouse Gas Emissions, in: C.E. Thomas (Ed.), Stopping Clim. Chang. Case Hydrog. Coal, Lect. Notes Energy, Springer International, 2017: pp. 9–12. <https://doi.org/10.1007/978-3-319-31655-0>.
- [40] D. Jones, D. Bhattacharyya, R. Turton, S.E. Zitney, Optimal design and integration of an air separation unit (ASU) for an integrated gasification combined cycle (IGCC) power plant with CO₂ capture, Fuel Process. Technol. 92 (2011) 1685–1695. <https://doi.org/10.1016/j.fuproc.2011.04.018>.
- [41] T.C. Merkel, M. Zhou, R.W. Baker, Carbon dioxide capture with membranes at an IGCC power plant, J. Memb. Sci. 389 (2012) 441–450. <https://doi.org/10.1016/j.memsci.2011.11.012>.
- [42] N.S. Siefert, S. Litster, Exergy and economic analyses of advanced IGCC–CCS and IGFC–CCS power plants, Appl. Energy. 107 (2013) 315–328.
- [43] A.D. Rao, A. Verma, G.S. Samuelsen, ENGINEERING AND ECONOMIC ANALYSES OF A COAL-FUELED SOLID OXIDE FUEL CELL HYBRID POWER PLANT, in: ASME Turbo Expo 2005, 2005: pp. 1–9.
- [44] J.C. Meerman, M. Knoope, A. Ramírez, W.C. Turkenburg, A.P.C. Faaij, The techno-economic potential of integrated gasification co-generation facilities with CCS Going from coal to biomass, Energy Procedia. 37 (2013) 6053–6061. <https://doi.org/10.1016/j.egypro.2013.06.534>.
- [45] K. Makino, Clean Coal Technology-For the Future Utilization, in: G. Yue, S. Li

- (Eds.), *Clean Coal Technol. Sustain. Dev.*, Springer Science+Business Media, 2016: pp. 3–9. <https://doi.org/10.1007/978-981-10-2023-0>.
- [46] P.S. Parulekar, Comparison between oxygen-blown and air-blown IGCC power plants: A gas turbine perspective, in: *Proc. ASME Turbo Expo 2011*, 2011: pp. 537–545. <https://doi.org/10.1115/GT2011-45154>.
- [47] L. Jimenez, M. Gadalla, D. Boer, T. Majozi, Integrated gasification combined cycle (IGCC) process simulation and optimization, *Comput. Chem. Eng.* 34 (2010) 331–338. <https://doi.org/10.1016/j.compchemeng.2009.04.007>.
- [48] T. Yamada, T. Ishii, M. Takatou, Y. Iso, *Study Results in Demonstration Operation of Oxyfuel Combustion Boiler for CO₂ Capture*, 2009. <http://ci.nii.ac.jp/naid/110007131514/>.
- [49] T. Uchida, Toward the realization of CO₂ zero-emission coal fired power plant using the oxyfuel technology, *Therm. Nucl. Power Gener. Conv.* 10 (2014) 101–106. <https://doi.org/10.14942/TENPES.10.101>.
- [50] T. Hasegawa, Development of Gas Turbine Combustors for Air-Blown IGCC, in: E. Benini (Ed.), *Adv. Gas Turbine Technol.*, Ernesto Be, Intech, 2016: pp. 239–266. <https://doi.org/http://dx.doi.org/10.5772/57353>.
- [51] D. SAQUIB SULTAN, C. MÜLLER, J. DENNIS, Capture of CO₂, in: *Energy & Fuels*, 2010: pp. 3687–3697.
- [52] P.N. Dyer, R.E. Richards, S.L. Russek, Ionic Transport Membrane Technology for Oxygen Separation and Syngas Production, in: *Electrochem. Soc. Proc.*, 1999: pp. 1173–1176. <https://doi.org/10.1149/199919.1173pv>.
- [53] K. Damen, M. Van Troost, A. Faaij, W. Turkenburg, A comparison of electricity and hydrogen production systems with CO₂ capture and storage. Part A: Review

- and selection of promising conversion and capture technologies, *Prog. Energy Combust. Sci.* 32 (2006) 215–246. <https://doi.org/10.1016/j.pecs.2005.11.005>.
- [54] R.J. Allam, Improved oxygen production technologies, *Energy Procedia*. 1 (2009) 461–470. <https://doi.org/10.1016/j.egypro.2009.01.062>.
- [55] A.R. Smith, J. Klosek, A review of air separation technologies and their integration with energy conversion processes, *Fuel Process. Technol.* 70 (2001) 115–134. [https://doi.org/10.1016/S0378-3820\(01\)00131-X](https://doi.org/10.1016/S0378-3820(01)00131-X).
- [56] S. Chen, N. Lior, W. Xiang, Coal gasification integration with solid oxide fuel cell and chemical looping combustion for high-efficiency power generation with inherent CO₂ capture, *Appl. Energy*. 146 (2015) 298–312. <https://doi.org/10.1016/j.apenergy.2015.01.100>.
- [57] P.N. Dyer, R.E. Richards, S.L. Russek, D.M. Taylor, Ion transport membrane technology for oxygen separation and syngas production, *Solid State Ionics*. 134 (2000) 21–33. [https://doi.org/10.1016/S0167-2738\(00\)00710-4](https://doi.org/10.1016/S0167-2738(00)00710-4).
- [58] L. Rosen, N. Degenstein, M. Shah, J. Wilson, S. Kellya, J. Peck, M. Christie, Development of oxygen transport membranes for coal-based power generation, *Energy Procedia*. 4 (2011) 750–755. <https://doi.org/10.1016/j.egypro.2011.01.115>.
- [59] P.A. Armstrong, Development of ITM oxygen technology for integration in IGCC and other advanced power generation, Final Sci. Report, Air Prod. Chem. Inc. (2015). <https://doi.org/10.2172/1224800>.
- [60] L.L. Anderson, P.A. Armstrong, J.M. Repasky, V.E.E. Stein, Enabling clean coal power generation: ITM oxygen technology, 28th Annu. Int. Pittsburgh Coal Conf. 2011, PCC 2011. 1 (2011) 314–328.
- [61] D.N. A., An introduction to gases and the gases industry, in: *Ind. Gases*, 1st ed.,

- Springer Netherlands, 1950: pp. 1–60.
- [62] F. Cardarelli, Gases, in: Mater. Handb. A Concise Deskt. Ref., 2nd ed., Springer-Verlag London, 2008.
- [63] E. Almqvist, History of Industrial Gases, Springer Science+Business Media, 2002.
- [64] T. Sato, Introductory Classroom / Q & A Basic Knowledge of Industrial Gas (1st) What is Industrial Gas?, Japan Weld. Eng. Soc. 53 (2005) 129–134.
- [65] C.T. Grabowski, Atmospheric gases, in: J.G. Wilson (Ed.), Gen. Princ. Etiol., Plenum Press, 1977: pp. 405–420. <https://doi.org/10.1097/00007611-194708000-00020>.
- [66] N.A. Downie, Gas technology, in: Ind. Gases, Springer Netherlands, 2002: pp. 61–297.
- [67] G.R. McCain, Gases, in: J. Smith (Ed.), Food Addit. User's Handb., Blackie and Son Ltd, 1991: pp. 257–272.
- [68] gasworld, Oxygen global market report, (2007).
<https://www.gasworld.com/oxygen-global-market-report/1277.article>.
- [69] Air Products, 2019 Sustainability Report, 2019.
- [70] T. and I. (METI) Research and Statistics Department Minister's Secretariat Ministry of Economy, Yearbook of Current Production Statistics Chemical Industry, n.d.
https://www.meti.go.jp/statistics/tyo/seidou/result/gaiyo/resourceData/02_kagaku/nenpo/h2dbb2018k.pdf.
- [71] IHS Markit, Chemical Economics Handbook Air Separation Gases, 2019.
<https://www.ihs.com/products/air-separation-gases-chemical-economics->

handbook.html.

- [72] H. Schoen, Handbook of Purified Gases, Springer-Verlag Berlin Heidelberg, 2015. <https://doi.org/10.1007/978-3-540-32599-4>.
- [73] A. Kohl, R. Nielsen, Gas Purification, 5th ed., Gulf Professional Publishing, 1997.
- [74] F.G. Kerry, Industrial gas handbook: Gas separation and purification, Taylor & Francis, 2007. <https://doi.org/10.1201/9781420008265>.
- [75] M.J. Kirschner, A. Alekseev, S. Dowy, M. Grahl, L. Jansson, P. Keil, G. Lauermann, M. Meilinger, W. Schmehl, H. Weckler, C. Windmeier, Oxygen, WILEY, 2017. <https://doi.org/10.1002/14356007.a18>.
- [76] R.W. Rousseau, ed., Handbook of Separation Process Technology, John Wiley & Sons, Inc., 1987.
- [77] Prakash Rao, Michael Muller, Industrial Oxygen: Its Generation and Use, 2007 ACEEE Summer Study Energy Effic. Ind. (2007) 124–135.
http://aceee.org/files/proceedings/2007/data/papers/78_6_080.pdf.
- [78] National Center for Industrial Property Information and Training, Patent distribution support chart Gas separation membrane device, 2011.
- [79] Shinko AirTech, Ltd., Gas Generator, (2019).
- [80] Gas Science, (n.d.). <http://www.pupukids.com/jp/gas/01/049.html> (accessed November 6, 2019).
- [81] B.K. Dutta, Principles of Mass Transfer and Separation Processes, PHI Learning Private Limited, 2007.
- [82] X. Zhu, W. Yang, Mixed Conducting Ceramic Membranes: Fundamentals, Materials and Applications, Springer US, 2017. <https://doi.org/10.1007/978-3->

662-53534-9.

- [83] W. Yang, H. Wang, X. Zhu, L. Lin, Development and application of oxygen permeable membrane in selective oxidation of light alkanes, *Top. Catal.* 35 (2005) 155–167. <https://doi.org/10.1007/s11244-005-3820-6>.
- [84] J. Sunarso, S.S. Hashim, N. Zhu, W. Zhou, Perovskite oxides applications in high temperature oxygen separation, solid oxide fuel cell and membrane reactor: A review, *Prog. Energy Combust. Sci.* 61 (2017) 57–77. <https://doi.org/10.1016/j.pecs.2017.03.003>.
- [85] J. Sunarso, S. Baumann, J.M. Serra, W.A. Meulenbergh, S. Liu, Y.S. Lin, J.C. Diniz da Costa, Mixed ionic-electronic conducting (MIEC) ceramic-based membranes for oxygen separation, *J. Memb. Sci.* 320 (2008) 13–41. <https://doi.org/10.1016/j.memsci.2008.03.074>.
- [86] M.J. den Exter, W.G. Haije, J.F. Vente, Viability of ITM Technology for Oxygen Production and Oxidation Processes: Material, System, and Process Aspects, in: A.C. Bose (Ed.), *Inorg. Membr. Energy Environ. Appl.*, Springer Science+Business Media, 2009: pp. 1–319. <https://doi.org/10.1007/978-0-387-34526-0>.
- [87] J.B. Goodenough, A. Manthiram, M. Paranthaman, Y.S. Zhen, Oxide ion electrolytes, *Mater. Sci. Eng. B12* (1992) 357–364. [https://doi.org/10.1016/0921-5107\(92\)90006-U](https://doi.org/10.1016/0921-5107(92)90006-U).
- [88] B.C.H. Steele, Ceramic ion conducting membranes, *Curr. Opin. Solid State Mater. Sci.* 1 (1996) 684–691. [https://doi.org/10.1016/S1359-0286\(96\)80052-0](https://doi.org/10.1016/S1359-0286(96)80052-0).
- [89] W. Deibert, M.E. Ivanova, S. Baumann, O. Guillon, W.A. Meulenbergh, Ion-conducting ceramic membrane reactors for high-temperature applications, *J.*

- Memb. Sci. 543 (2017) 79–97. <https://doi.org/10.1016/j.memsci.2017.08.016>.
- [90] C. Wagner, Equations for transport in solid oxides and sulfides of transition metals, Prog. Solid State Chem. 10 (1975) 3–16. [https://doi.org/10.1016/0079-6786\(75\)90002-3](https://doi.org/10.1016/0079-6786(75)90002-3).
- [91] H. Takamura, Oxygen Permeable Ceramics, J. Surf. Finish. Society Japan. 56 (2005) 491–496.
- [92] X. Zhu, W. Yang, Mixed Conducting Ceramic Membranes: Fundamentals, Materials and Applications, 2017. <https://doi.org/10.1007/978-3-662-53534-9>.
- [93] C. Zhang, J. Sunarso, S. Liu, Designing CO₂-resistant oxygen-selective mixed ionic-electronic conducting membranes: Guidelines, recent advances, and forward directions, Chem. Soc. Rev. 46 (2017) 2941–3005. <https://doi.org/10.1039/c6cs00841k>.
- [94] J. Sunarso, S. Baumann, J.M. Serra, W.A. Meulenbergh, S. Liu, Y.S. Lin, J.C. Diniz da Costa, Mixed ionic-electronic conducting (MIEC) ceramic-based membranes for oxygen separation, J. Memb. Sci. 320 (2008) 13–41. <https://doi.org/10.1016/j.memsci.2008.03.074>.
- [95] C. Zhang, X. Meng, J. Sunarso, L. Liu, R. Xu, Z. Shao, S. Liu, Oxygen permeation behavior through Ce_{0.9}Gd_{0.1}O_{2-δ} membranes electronically short-circuited by dual-phase Ce_{0.9}Gd_{0.1}O_{2-δ}-Ag decoration, J. Mater. Chem. A. 3 (2015) 19033–19041. <https://doi.org/10.1039/c5ta04345j>.
- [96] J. Sunarso, K. Zhang, S. Liu, High Temperature Oxygen Separation Using Dense Ceramic Membrane, in: W.Y. Chen, T. Suzuki, M. Lackner (Eds.), Handb. Clim. Chang. Mitig. Adapt. Second Ed., 2nd ed., Springer International, 2016: pp. 2681–2706. <https://doi.org/10.1007/978-3-319-14409-2>.

- [97] D.D. Athayde, D.F. Souza, S.A. M.A., Review of perovskite ceramic synthesis and membrane preparation methods, *Ceram. Int.* 42 (2016) 6555–6571.
<https://doi.org/10.1016/j.ceramint.2016.01.130>.
- [98] A. Haffelin, C. Niedrig, S.F. Wagner, S. Baumann, W.A. Meulenber, E. Ivers-Tiffée, Three-Dimensional Performance Model for Oxygen Transport Membranes, *J. Electrochem. Soc.* 161 (2014) F1409–F1415.
<https://doi.org/10.1149/2.0601414jes>.
- [99] W.K. Hong, G.M. Choi, Oxygen permeation of BSCF membrane with varying thickness and surface coating, *J. Memb. Sci.* 346 (2010) 353–360.
<https://doi.org/10.1016/j.memsci.2009.09.056>.
- [100] S. Baumann, J.M. Serra, M.P. Lobera, S. Escolástico, F. Schulze-Küppers, W.A. Meulenber, Ultrahigh oxygen permeation flux through supported $\text{Ba}_{0.5}\text{Sr}_{0.5}\text{Co}_{0.8}\text{Fe}_{0.2}\text{O}_{3-\delta}$ membranes, *J. Memb. Sci.* 377 (2011) 198–205.
<https://doi.org/10.1016/j.memsci.2011.04.050>.
- [101] S. Baumann, P. Niehoff, F. Schulze-Küppers, M. Ramasamy, W.A. Meulenber, O. Guillon, The Role of Solid-Gas Electrochemical Interfaces for Mixed Ionic Electronic Conducting Oxygen Transport Membranes, *ECS Trans.* 66 (2015) 21–33.
- [102] P.M. Geffroy, J.M. Bassat, A. Vivet, S. Fourcade, T. Chartier, P. Del Gallo, N. Richet, Oxygen semi-permeation, oxygen diffusion and surface exchange coefficient of $\text{La}_{(1-x)}\text{Sr}_x\text{Fe}_{(1-y)}\text{Ga}_y\text{O}_{3-\delta}$ perovskite membranes, *J. Memb. Sci.* 354 (2010) 6–13. <https://doi.org/10.1016/j.memsci.2010.03.001>.
- [103] Y. Teraoka, T. Fukuda, N. Miura, N. Yamazoe, Development of Oxygen Semipermeable Membrane Using Mixed Conductive Perovskite-Type Oxides

- (Part 2), *J. Ceram. Soc. Japan*. 97 (1989) 533–538.
- [104] P. Lemes-Rachadel, G.S. Garcia, R.A.F. Machado, D. Hotza, J.C.D. da Costa, Current developments of mixed conducting membranes on porous substrates, *Mater. Res.* 17 (2014) 242–249. <https://doi.org/10.1590/S1516-14392013005000175>.
- [105] J.M. Serra, J. Garcia-Fayos, S. Baumann, F. Schulze-Küppers, W.A. Meulenbergh, Oxygen permeation through tape-cast asymmetric all- $\text{La}_{0.6}\text{Sr}_{0.4}\text{Co}_{0.2}\text{Fe}_{0.8}\text{O}_{3-\delta}$ membranes, *J. Memb. Sci.* 447 (2013) 297–305. <https://doi.org/10.1016/j.memsci.2013.07.030>.
- [106] A.A. Plazaola, A.C. Labella, Y. Liu, N.B. Porras, D.A.P. Tanaka, M.V.S. Annaland, F. Gallucci, Mixed ionic-electronic conducting membranes (MIEC) for their application in membrane reactors: A review, *Processes*. 7 (2019). <https://doi.org/10.3390/pr7030128>.
- [107] S. Baumann, W.A. Meulenbergh, H.P. Buchkremer, Manufacturing strategies for asymmetric ceramic membranes for efficient separation of oxygen from air, *J. Eur. Ceram. Soc.* 33 (2013) 1251–1261. <https://doi.org/10.1016/j.jeurceramsoc.2012.12.005>.
- [108] K. Watanabe, M. Yuasa, T. Kida, K. Shimanoe, Y. Teraoka, N. Yamazoe, Dense/porous asymmetric-structured oxygen permeable Membranes based on $\text{La}_{0.6}\text{Ca}_{0.4}\text{CoO}_{3-\delta}$ perovskite-type oxide, *Chem. Mater.* 20 (2008) 6965–6973. <https://doi.org/10.1021/cm8013144>.
- [109] F. Schulze-Küppers, S. Baumann, W.A. Meulenbergh, D. Stöver, H.P. Buchkremer, Manufacturing and performance of advanced supported $\text{Ba}_{0.5}\text{Sr}_{0.5}\text{Co}_{0.8}\text{Fe}_{0.2}\text{O}_{3-\delta}$ (BSCF) oxygen transport membranes, *J. Memb. Sci.* 433

- (2013) 121–125. <https://doi.org/10.1016/j.memsci.2013.01.028>.
- [110] P.L. Rachadel, J. Motuzas, G. Ji, D. Hotza, J.C. Diniz da Costa, The effect of non-ionic porous domains on supported $\text{Ba}_{0.5}\text{Sr}_{0.5}\text{Co}_{0.8}\text{Fe}_{0.2}\text{O}_{3-\delta}$ membranes for O_2 separation, *J. Memb. Sci.* 454 (2014) 382–389. <https://doi.org/10.1016/j.memsci.2013.11.054>.
- [111] P. Niehoff, S. Baumann, F. Schulze-Küppers, R.S. Bradley, I. Shapiro, W.A. Meulenbergh, P.J. Withers, R. Vaßen, Oxygen transport through supported $\text{Ba}_{0.5}\text{Sr}_{0.5}\text{Co}_{0.8}\text{Fe}_{0.2}\text{O}_{3-\delta}$ membranes, *Sep. Purif. Technol.* 121 (2014) 60–67. <https://doi.org/10.1016/j.seppur.2013.07.002>.
- [112] J.G. Pharoah, L. Handl, V. Schmidt, The effect of electrode morphology on solid oxide fuel cell performance, *Energyequipsys.* 3 (2015) 25–32. <https://doi.org/10.1149/06801.2037ecst>.
- [113] A. V. Kovalevsky, A.A. Yaremchenko, V.A. Kolotygin, A.L. Shaula, V. V. Kharton, F.M.M. Snijders, A. Buekenhoudt, J.R. Frade, E.N. Naumovich, Processing and oxygen permeation studies of asymmetric multilayer $\text{Ba}_{0.5}\text{Sr}_{0.5}\text{Co}_{0.8}\text{Fe}_{0.2}\text{O}_{3-\delta}$ membranes, *J. Memb. Sci.* 380 (2011) 68–80. <https://doi.org/10.1016/j.memsci.2011.06.034>.
- [114] B. He, D. Ding, Y. Ling, J. Xu, L. Zhao, Efficient modification for enhancing surface activity of $\text{Ba}_{0.5}\text{Sr}_{0.5}\text{Co}_{0.8}\text{Fe}_{0.2}\text{O}_{3-\delta}$ oxygen permeation membrane, *J. Memb. Sci.* 477 (2015) 7–13. <https://doi.org/10.1016/j.memsci.2014.12.020>.
- [115] P.L. Rachadel, J. Motuzas, R.A.F. Machado, D. Hotza, J.C. Diniz da Costa, Influence of porous structures on O_2 flux of BSCF asymmetric membranes, *Sep. Purif. Technol.* 175 (2017) 164–169. <https://doi.org/10.1016/j.seppur.2016.10.053>.
- [116] S. Baumann, J.M. Serra, M.P. Lobera, S. Escolástico, F. Schulze-Küppers, W.A.

- Meulenberg, Ultrahigh oxygen permeation flux through supported $\text{Ba}_{0.5}\text{Sr}_{0.5}\text{Co}_{0.8}\text{Fe}_{0.2}\text{O}_{3-\delta}$ membranes, *J. Memb. Sci.* 377 (2011) 198–205.
<https://doi.org/10.1016/j.memsci.2011.04.050>.
- [117] G. Pećanac, S. Foghmoes, M. Lipińska-Chwalek, S. Baumann, T. Beck, J. Malzbender, Strength degradation and failure limits of dense and porous ceramic membrane materials, *J. Eur. Ceram. Soc.* 33 (2013) 2689–2698.
<https://doi.org/10.1016/j.jeurceramsoc.2013.04.018>.
- [118] J.H. Park, E. Magnone, J.P. Kim, S.H. Choi, Oxygen permeation performance of $\text{Ba}_{0.5}\text{Sr}_{0.5}\text{Co}_{0.8}\text{Fe}_{0.2}\text{O}_{3-\delta}$ membrane after surface modification, *Korean J. Chem. Eng.* 29 (2012) 235–242. <https://doi.org/10.1007/s11814-011-0153-y>.
- [119] S.Y. Jeon, H.N. Im, B. Singh, M. Choi, Y.S. Yoo, J.H. Hwang, S.J. Song, Oxygen permeation through dense $\text{La}_{0.1}\text{Sr}_{0.9}\text{Co}_{0.8}\text{Fe}_{0.2}\text{O}_{3-\delta}$ perovskite membranes: Catalytic effect of porous $\text{La}_{0.1}\text{Sr}_{0.9}\text{Co}_{0.8}\text{Fe}_{0.2}\text{O}_{3-\delta}$ layers, *Ceram. Int.* 41 (2015) 7446–7452. <https://doi.org/10.1016/j.ceramint.2015.02.064>.
- [120] B. He, K. Zhang, Y. Ling, J. Xu, L. Zhao, A surface modified $\text{La}_{0.6}\text{Sr}_{0.4}\text{Co}_{0.2}\text{Fe}_{0.8}\text{O}_{3-\delta}$ ultrathin membrane for highly efficient oxygen separation, *J. Memb. Sci.* 464 (2014) 55–60.
<https://doi.org/10.1016/j.memsci.2014.03.075>.
- [121] B.T. Na, J.H. Park, J.H. Park, J.H. Yu, J.H. Joo, Elucidation of the Oxygen Surface Kinetics in a Coated Dual-Phase Membrane for Enhancing Oxygen Permeation Flux, *ACS Appl. Mater. Interfaces.* 9 (2017) 19917–19924.
<https://doi.org/10.1021/acsami.7b04685>.
- [122] X. Tan, K. Li, *Inorganic Membrane Reactors*, John Wiley & Sons, Ltd, 2015.
- [123] A.C. Bose, ed., *Inorganic Membranes for Energy and Environmental*

Applications, Springer Science+Business Media, 2009.

- [124] C. Karakaya, R.J. Kee, Progress in the direct catalytic conversion of methane to fuels and chemicals, *Prog. Energy Combust. Sci.* **55** (2016) 60–97.
<https://doi.org/10.1016/j.pecs.2016.04.003>.
- [125] Z. Dai, L. Ansaloni, L. Deng, Recent advances in multi-layer composite polymeric membranes for CO₂ separation: A review, *Green Energy Environ.* **1** (2016) 102–128. <https://doi.org/10.1016/j.gee.2016.08.001>.
- [126] L.K. Wang, J.P. Chen, Y.-T. Hung, N.K. Shamas, eds., *Membrane and Desalination Technologies*, 13th ed., Humana Press, 2011.
<https://doi.org/10.1007/978-1-59745-278-6>.
- [127] M.A. Nemitallah, M.A. Habib, H.M. Badr, Ion Transport Membranes (ITMs) for Oxygen Separation, in: *Oxyfuel Comb. Clean Energy Appl. Green Energy Technol.*, 2019: pp. 91–132. https://doi.org/10.1007/978-3-030-10588-4_3.
- [128] M.F. Carolan, C.M. Chen, S.W. Rynders, Engineering Development of Ceramic Membrane Reactor Systems for Converting Natural Gas to Hydrogen and Synthesis Gas for Liquid Transportation Fuels, *Proc. 2002 U.S. DOE Hydrog. Progr. Rev. NREL/CP-61* (2002) 1–9.
- [129] H. Takamura, Hydrocarbon Reforming by Using Oxygen Permeable Membranes, *MEMBRANE*. **37** (2012) 67–73.
- [130] D.D. Athayde, D.F. Souza, A.M.A. Silva, D. Vasconcelos, E.H.M. Nunes, J.C.D. Da Costa, W.L. Vasconcelos, Review of perovskite ceramic synthesis and membrane preparation methods, *Ceram. Int.* **42** (2016) 6555–6571.
<https://doi.org/10.1016/j.ceramint.2016.01.130>.
- [131] H. Takebe, K. Mirinaga, Fabrication of YSZ Tubes Consisted of Dense and

- Porous Layers for Solid Oxide Fuel Cell by the Slip Casting, *Ceram. Soc. Japan*. 98 (1990) 1088–1092.
- [132] D. Beckel, A. Bieberle-Hütter, A. Harvey, A. Infortuna, U.P. Muecke, M. Prestat, J.L.M. Rupp, L.J. Gauckler, Thin films for micro solid oxide fuel cells, *J. Power Sources*. 173 (2007) 325–345. <https://doi.org/10.1016/j.jpowsour.2007.04.070>.
- [133] A.J. Moulson, J.M. Herbert, eds., *Electroceramics: Materials, Properties, Applications*, 2nd ed, WILEY, 2003.
- [134] A.A. Tracton, *Coatings technology: Fundamentals, testing, and processing techniques*, 2006.
- [135] S.P. Jiang, Thin coating technologies and applications in high-temperature solid oxide fuel cells, in: S. Zhang (Ed.), *Org. Nanostructured Thin Film Devices Coatings Clean Energy*, CRC Press, 2010: pp. 155–188. <https://doi.org/10.1201/b11846>.
- [136] D.F. Souza, E.H.M. Nunes, W.L. Vasconcelos, Preparation of $\text{Ba}_{0.5}\text{Sr}_{0.5}\text{Co}_{0.8}\text{Fe}_{0.2}\text{O}_{3-\delta}$ asymmetric structures by freeze-casting and dip-coating, *Ceram. Int.* 44 (2018) 1002–1006. <https://doi.org/10.1016/j.ceramint.2017.10.035>.
- [137] P.L. Rachadel, D.F. Souza, E.H.M. Nunes, J.C.D. da Costa, W.L. Vasconcelos, D. Hotza, A novel route for manufacturing asymmetric BSCF-based perovskite structures by a combined tape and freeze casting method, *J. Eur. Ceram. Soc.* 37 (2017) 5249–5257. <https://doi.org/10.1016/j.jeurceramsoc.2017.04.035>.
- [138] M. Suzuki, Introduction to Thin Film Deposition, *J. Vac. Soc. Jpn.* 57 (2014) 303–307.
- [139] J. Zhu, Z. Liu, S. Guo, W. Jin, Influence of permeation modes on oxygen permeability of the multichannel mixed-conducting hollow fibre membrane,

- Chem. Eng. Sci. 122 (2015) 614–621. <https://doi.org/10.1016/j.ces.2014.10.014>.
- [140] B.F.K. Kingsbury, K. Li, A morphological study of ceramic hollow fibre membranes, *J. Memb. Sci.* 328 (2009) 134–140.
<https://doi.org/10.1016/j.memsci.2008.11.050>.
- [141] A.M. Ilham, N. Khoiroh, S. Jovita, R.M. Iqbal, L. Harmelia, S.D. Nurherdiana, W.P. Utomo, H. Fansuri, Morphological and Physical Study of $\text{La}_{0.7}\text{Sr}_{0.3}\text{Co}_{0.2}\text{Fe}_{0.8}\text{O}_{3-\delta}$ (LSCF 7328) Flat Membranes Modified by Polyethylene Glycol (PEG), *J. Appl. Membr. Sci. Technol.* 22 (2018) 119–130.
<https://doi.org/10.11113/amst.v22n2.131>.
- [142] Y. Chi, T. Li, B. Wang, Z. Wu, K. Li, Morphology, performance and stability of multi-bore capillary $\text{La}_{0.6}\text{Sr}_{0.4}\text{Co}_{0.2}\text{Fe}_{0.8}\text{O}_{3-\delta}$ oxygen transport membranes, *J. Memb. Sci.* 529 (2017) 224–233. <https://doi.org/10.1016/j.memsci.2017.02.010>.
- [143] X.M. Tan, D. Rodrigue, A review on porous polymeric membrane preparation. Part I: Production techniques with polysulfone and poly (vinylidene fluoride), *Polymers (Basel)*. 11 (2019). <https://doi.org/10.3390/polym11071160>.
- [144] W. Lu, Z. Yuan, Y. Zhao, H. Zhang, H. Zhang, X. Li, Porous membranes in secondary battery technologies, *Chem. Soc. Rev.* 46 (2017) 2199–2236.
<https://doi.org/10.1039/c6cs00823b>.
- [145] G.R. Guillen, Y. Pan, M. Li, E.M. V Hoek, Preparation and Characterization of Membranes Formed by Nonsolvent Induced Phase Separation : A Review, *Ind. Eng. Chem. Res.* 50 (2011) 3798–3817. <https://doi.org/10.1021/ie101928r>.
- [146] J. Smid, C.G. Avci, V. Günay, R.A. Terpstra, J.P.G.M. Van Eijk, Preparation and characterization of microporous ceramic hollow fibre membranes, *J. Memb. Sci.* 112 (1996) 85–90. [https://doi.org/10.1016/0376-7388\(95\)00274-X](https://doi.org/10.1016/0376-7388(95)00274-X).

- [147] X. Zhu, W. Yang, Dual-, in: *Mix. Conduct. Ceram. Membr. Fundam. Mater. Appl.*, 2017: p. 375. <https://doi.org/10.1007/978-3-662-53534-9>.
- [148] P. Bernardo, G. Clarizia, 30 Years of Membrane Technology for Gas Separation, *Chem. Eng. Trans.* 32 (2013) 1999–2004. <https://doi.org/10.3303/CET1332334>.
- [149] D.R. Askeland, P.P. Fulay, W.J. Wright, *The Science and Engineering of Materials*, 6th ed., Cengage Learning, 2011.
<https://doi.org/10.2355/isijinternational1966.26.93>.
- [150] C.B. Carter, M.G. Norton, *Ceramic Materials Science and Engineering*, 2nd ed., Springer Science+Business Media, 2013.
<https://doi.org/10.1017/CBO9781107415324.004>.
- [151] M.N. Rahaman, *Ceramic Processing and Sintering*, 2nd ed., MARCEL DEKKER, 2003. <https://doi.org/10.1201/9781315274126>.
- [152] M. Kaneno, Historical Development of Porous Fine Ceramics, *Natl. Museum Nat. Sci. Tokyo, Surv. Rep.* 12th. (2008) 163–194.
- [153] J. Hojo, *Ceramics Powder Processing : Design of Particle Structure toward Development of Sintered Texture and Functions*, *J. Jpn. Soc. Powder Powder Metall.* 63 (2016) 801–810.
- [154] D. Sarkar, ed., *Ceramic processing*, CRC Press, 2017.
<https://doi.org/10.1201/9781315276045>.
- [155] R. Pampuch, A Brief History of Ceramic Innovation, in: *An Introd. to Ceram.*, Springer International, 2014: pp. 1–16. <https://doi.org/10.1007/978-3-319-10410-2>.
- [156] F. Shi, *Ceramic Materials - Progress in Modern Ceramics*, IntechOpen, 2012.
<https://doi.org/10.5772/2593>.

- [157] J.S. Reed, Principles of Ceramics Processing, 2nd ed., John Wiley & Sons, Inc., 2013.
- [158] M. Takahashi, Fundamental of Ceramics Powder Forming Processes and Further Development for Novel Materials, Hunsai. (2010) 3–14.
- [159] M. Fuji, T. Yamakawa, H. Watanabe, T. Endo, M. Takahashi, Tasks in Ceramics Powder Forming to Be Overcome, Annu. Rep. Ceram. Res. Lab. Nagoya Inst. Technol. 7 (2007) 29–43.
- [160] M. Arakawa, Introduction to Power Science, Japan Soc. Colour Mater. 43 (1970) 603–611.
- [161] T. Uchikoshi, Microstructure Design of Ceramics by Cotrolling the Dispersion of Fine Particles in a Liquid, and the Application of the Design Technique to Fabricate Novel Materials., THE MICROMERITICS. 57 (2014) 36–42.
- [162] W.M. Sigmund, N.S. Bell, L. Bergström, Novel Powder-Processing Methods for Advanced Ceramics, J. Am. Ceram. Soc. 83 (2000) 1557–1574.
<https://doi.org/10.1111/j.1151-2916.2000.tb01432.x>.
- [163] Y. Sakka, Fabrication of Highly Microstructure Controlled Ceramics by Novel Colloidal Processing, J. Ceram. Soc. Japan. 114 (2006) 371–376.
- [164] I. Nakamura, The Effect of Slurry Control on Structure and Characteristic of Electronic Ceramics, THE MICROMERITICS. 54 (2011) 47–51.
- [165] N. Adachi, O. Sakurada, M. Hashiba, Ceramic Processing Using Aqueous Suspension, J. Soc. Inorg. Mater. Japan. 12 (2005) 463–471.
- [166] J.A. Lewis, Colloidal Processing of Ceramics, J. Am. Ceram. Soc. 83 (2004) 2341–2359. <https://doi.org/10.1111/j.1151-2916.2000.tb01560.x>.
- [167] Y. Sakka, T.S. Suzuki, T. Uchikoshi, Fabrication of Highly Structural Controlled

- Ceramics by Advanced Colloidal Processing, *THE MICROMERITICS*. 54 (2011) 28–35.
- [168] J.B. Madeline, M. Meireles, J. Persello, C. Martin, R. Botet, R. Schweins, B. Cabane, From colloidal dispersions to colloidal pastes through solid-liquid separation processes, *Pure Appl. Chem.* 77 (2005) 1369–1394.
<https://doi.org/10.1351/pac200577081369>.
- [169] P. Coussot, Colloid, in: *Rheophysics, Soft Biol. Matter*, Springer International, 2014: pp. 1–332. <https://doi.org/10.1007/978-3-319-06148-1>.
- [170] J.R. Partington, Colloids, in: *A Hist. Chem.*, Macmillan & Co ltd, 1964: pp. 729–746. <https://doi.org/10.4159/harvard.9780674866157.c28>.
- [171] K. Inoue, Fundamental Aspects of Interface and Colloid Chemistry, *J. Met. Finish. Soc.* 29 (1978) 261–267.
- [172] P. Sarkar, P.S. Nicholson, Electrophoretic Deposition (EPD): Mechanisms, Kinetics, and Application to Ceramics, *J. Am. Ceram. Soc.* 79 (1996) 1987–2002.
- [173] E. Cristiano, Y.J. Hu, M. Siegfried, D. Kaplan, H. Nitsche, A comparison of point of zero charge measurement methodology, *Clays Clay Miner.* 59 (2011) 107–115.
<https://doi.org/10.1346/CCMN.2011.0590201>.
- [174] E. Tombácz, Ph-dependent surface charging of metal oxides, *Period. Polytech.* 53 (2009) 77–86. <https://doi.org/10.3311/pp.ch.2009-2.08>.
- [175] T.J. Graule, F.H. Baader, L.J. Gauckler, Casting uniform ceramics with direct coagulation, *Chemtech.* 25 (1995) 31–37.
- [176] E. Matijevic, ed., *Surface and Colloid Science*, 12th ed., Plenum Press, 1982.
- [177] A. Watanabe, The Coagulation of Colloidal Powders, *Japan Soc. Powder Powder Metall.* 11 (1964) 17–40.

- [178] H. Ohshima, Basic Theory of Colloid Stability, J. Jpn. Soc. Color Mater. 77 (2004) 328–332.
- [179] S. Hatisu, Electric double layer and ζ -potential, J. Jpn. Soc. Color Mater. 38 (2005) 523–528. <https://doi.org/10.1002/0471799742.ch5>.
- [180] K. Furusawa, Fundamental Theory of Fine Particle Suspension Stability, Japanese Soc. Print. Sci. Technol. 30 (1993) 76–83.
<https://doi.org/10.11413/nig1987.30.76>.
- [181] Y. ADACHI, M. KOBAYASHI, L. FENG, Y. TSUJIMOTO, Y. YAMASHITA, Electrical Double Layers and Colloidal Flocculation, Oleoscience. 13 (2013) 299–307. <https://doi.org/10.5650/oleoscience.13.299>.
- [182] W.M. Sigmund, N.S. Bell, L. Bergström, Novel Popwder-Processing Methods for Advanced Ceramics, J. Am. Ceram. Soc. 87 (2000) 1557–1574.
<https://doi.org/10.1007/s00595-015-1265-5>.
- [183] P. Sarkar, P.S. Nicholson, Electrophoretic deposition (EPD): Mechanisms, kinetics, and application to ceramics, J. Am. Ceram. Soc. 79 (1996) 1987–2002.
<https://doi.org/10.1111/j.1151-2916.1996.tb08929.x>.
- [184] C. Felix, A. Yaroshchuk, S. Pasupathi, B.G. Pollet, M.P. Bondarenko, V.I. Kovalchuk, E.K. Zholkovskiy, Electrophoresis and stability of nano-colloids: History, theory and experimental examples, Adv. Colloid Interface Sci. 211 (2014) 77–92. <https://doi.org/10.1016/j.cis.2014.06.005>.
- [185] K. Furusawa, Zeta(ζ)-potential Measurements, Bunseki. 5 (2004) 247–254.
<https://doi.org/10.1038/ni.3772>.
- [186] S. Takeda, Electrokinetics in Highly Concentrated Colloid Systems, Japan Oil Chem. Soc. 13 (2013) 315–320.

- [187] H. Ohshima, Developments in Theories of Electrokinetic Phenomena : From Smoluchowski to ELKIN, Japan Oil Chem. Soc. 13 (2013) 291–297.
- [188] B. Ferrari, R. Moreno, EPD kinetics: A review, J. Eur. Ceram. Soc. 30 (2010) 1069–1078. <https://doi.org/10.1016/j.jeurceramsoc.2009.08.022>.
- [189] J.H. Dickerson, A.R. Boccaccini, eds., Electrophoretic Deposition of Nanomaterials, Springer, 2013. <https://doi.org/10.1007/978-1-4614-4605-7>.
- [190] L. Besra, M. Liu, A review on fundamentals and applications of electrophoretic deposition (EPD), Prog. Mater. Sci. 52 (2007) 1–61. <https://doi.org/10.1016/j.pmatsci.2006.07.001>.
- [191] M.F. De Riccardis, Ceramic Coatings Obtained by Electrophoretic Deposition: Fundamentals, Models, Post-Deposition Processes and Applications, in: F. Shi (Ed.), Ceram. Coatings - Appl. Eng., IntechOpen, 2012. <https://doi.org/10.5772/29435>.
- [192] I. Aznam, J.C.W. Mah, A. Muchtar, M.R. Somalu, M.J. Ghazali, A review of key parameters for effective electrophoretic deposition in the fabrication of solid oxide fuel cells, J. Zhejiang Univ. Sci. A. 19 (2018) 811–823. <https://doi.org/10.1631/jzus.A1700604>.
- [193] P.M. Biesheuvel, H. Verweij, Theory of Cast Formation in Electrophoretic Deposition, J. Am. Ceram. Soc. 82 (1999) 1451–1455. <https://doi.org/10.1111/j.1151-2916.1999.tb01939.x>.
- [194] L. Besra, M. Liu, A review on fundamentals and applications of electrophoretic deposition (EPD), Prog. Mater. Sci. 52 (2007) 1–61. <https://doi.org/10.1016/j.pmatsci.2006.07.001>.
- [195] T. Uchikoshi, Fabrication of Inorganic Nano-Material by Electrophoretic

- Deposition, J. Soc. Inorg. Mater. Japan. 8 (2001) 478–483.
- [196] J. Hamagami, K. Kanamura, Innovation of Material Processing by Using Electrophoretic Deposition Method, J. Soc. Powder Technol., Japan. 39 (2002) 587–594.
- [197] T.M. Sridhar, N. Eliaz, U. Kamachi Mudali, B. Raj, Electrophoretic Deposition of Hydroxyapatite Coatings and Corrosion Aspects of Metallic Implants, Corros. Rev. 20 (2002) 255–294. <https://doi.org/10.1515/CORRREV.2002.20.4-5.255>.

Chapter 2 | Application of electrophoretic deposition process to BSCF asymmetric membrane

Preface

As mentioned in the previous chapter, BSCF-based MIEC membrane with asymmetric structure have been attracted attention for air separation application. In this chapter the process parameters such as suspension preparation and subsequent co-firing conditions in the EPD process of an oxygen separation membrane with an asymmetric structure have been examined. After that, the air separation characteristics of the produced oxygen separation membrane have been evaluated. Consequently, the effectiveness of the EPD process in the production of the oxygen separation membrane using BSCF-based MIEC has been verified.

1. Introduction

Oxygen is one of the most important industrial gases widely used in various fields such as the chemical industry, iron metallurgy, glass manufacturing, clean power generation and environmental protection. Oxygen is industrially produced by the separation from air and the methods are roughly classified into three types; i.e., cryogenic separation, adsorption separation and membrane separation. Among them, the cryogenic separation method using the difference in the boiling points of oxygen, nitrogen and argon is the most common method suitable for the mass production of the high purity gas (>99%). At present, only cryogenic distillation is a commercialized technology for the large-scale production of pure oxygen. In recent years, the idea of not

only large-scale industrial production, but also the distributed placement of small to medium scale production, the so-called “local production for local consumption”, has been widely used mainly in the field of energy production. Adsorption separation using a zeolite is a suitable method for small to medium scale production, but the purity of the obtained oxygen is as low as 95%. On the other hand, membrane separation by utilizing the difference in the molecular sizes of the oxygen and nitrogen and their affinity to the membrane surface is also suitable for small-scale production. For example, high-speed oxygen separation technology using graphene having nanoscale windows (pores?) as large as molecular oxygen has recently been reported [1]. Oxygen pumping using an oxide ion conductor is another effective method for obtaining high purity-oxygen, but an external circuit connection is necessary for driving the reaction. Oxygen separation membranes using mixed ion electron conductors (MIECs) are attracting attention because they can be driven only by the oxygen partial pressure difference across the membrane at high temperatures without connecting to external circuits [2–7].

The oxygen separation membrane using a perovskite-type $\text{La}_{1-x}\text{Sr}_x\text{Co}_{1-y}\text{Fe}_y\text{O}_{3-\delta}$ (LSCF)-based MIEC was first reported by Teraoka et al. [8]. Since then, the oxygen separation properties of the MIEC membrane have been improved by partially or totally replacing the A or B site cations in many perovskite-type oxide systems. Especially, it has been reported that the $\text{Ba}_{0.5}\text{Sr}_{0.5}\text{Co}_{0.8}\text{Fe}_{0.2}\text{O}_{3-\delta}$ (BSCF)-based membrane exhibits an excellent oxygen separation property [9]. In general, the bulk diffusion rate of the oxide ion in an MIEC membrane increases in proportion to the oxygen concentration gradient. Reducing the membrane thickness is a common strategy to improve the oxygen separation property, however, further improvement of the oxygen separation property is required for practical use.

For example, improvement of the oxygen separation performance has been attempted using an asymmetric-structured membrane consisting of dense/porous bi-layers. The porous layer plays the role of the site for the dissociation reaction of oxygen as well as the support for thinning the dense layer. Teraoka et al. reported that the dense/porous asymmetric structure can effectively to improve the mechanical strength and oxygen separation performance of the $\text{La}_{0.6}\text{Sr}_{0.4}\text{CoO}_{3-\delta}$ (LSC)-based oxygen separation membranes. They demonstrated that the oxygen separation performance was significantly improved by reducing the thickness of the dense layer from 1.5 mm to about 15 μm [10,11]. For the fabrication process of oxygen separation membranes with an asymmetric structure, thin layers are usually prepared on porous supports by tape casting, screen printing, dip coating and spin coating [10]. The phase inversion method is a promising technique to produce a ceramic asymmetric membrane in a single step at a lower cost. However, since the phase inversion of ceramic films involves many variables during the manufacturing process, control of the film thickness and structure is possible, but not easy [11–13]. The tape casting method is generally used as a method for producing a free-standing film, but is not suitable for producing an asymmetric film. Besides these methods, porous body preparation methods, such as the perovskite foam method, have been reported [14–16]. However, organic substances, such as binders contained in the green layer, often prevent the formation of good interface bonding between the thin dense layer and the porous support [17–22]. An alternative method to these wet processes is the electrophoretic deposition (EPD) process which is one of the colloidal processes wherein ceramic layers are directly shaped on a conductive substrate from stable colloidal suspensions by the application of a DC electric field. The MIEC exhibits an electronic conduction at room temperature, therefore, it can be directly used

as an EPD electrode without any further surface treatment, such as a graphite coating. However, in order to obtain a gas-tight dense and thin layer on a porous support by the following co-firing process, the thermal expansion and shrinkage characteristics of the porous support and thin layer should be determined [23].

In this study, we tried to fabricate BSCF-based asymmetric oxygen separation membranes using the EPD process followed by co-firing. It may be a problem of practical concern that BSFC membranes have a low mechanical resistance and low chemical stability. In particular, the high chemical reactivity of BSCF will lead to the formation of a very resistant reactive phase at the interface when another mixed conductor is used as a support layer. However, such problems would be solved by using the same BSCF for the support and the thin dense membrane. The pre-firing temperature of the support must be lower than the co-firing temperature to prevent cracking and peeling of the thin layer due to the generation of thermal stress during the co-firing. The co-firing conditions should be optimized so that the thin layer is fully densified, while the support layer retains a porous structure [18–22]. Based on these factors, a detailed study was made of the preparation conditions of the porous support and thin layer as well as the co-firing conditions.

2. Experimental methods

Figure 2-1, Process (I) shows a schematic illustration explaining the preparation procedure of the porous support. $\text{Ba}_{0.5}\text{Sr}_{0.5}\text{Co}_{0.8}\text{Fe}_{0.2}\text{O}_{3-\delta}$ (BSCF) prepared by the citrate precursor method with a D50 particle size of 0.55 μm (Kusaka Rare Metal Products Co., Ltd.) and wheat starch as the pore-forming agent with a particle size of 1–30 μm (Nakarai

Tesque, Inc.) were used. The BSCF powder and pre-determined ratio (0~50 wt%) of the starch powders were mixed in a mortar. The powder mixture was uniaxially pressed into a disc with a 1.0-mm thickness and 28-mm diameter, then pre-fired at 500 °C for 1 hours to obtain a porous support. To prepare the suspension for the EPD, the BSCF powder was dispersed in reagent-grade ethanol (0.6 g/ 100 ml), then ultrasonicated. The zeta potential of the suspension was measured by laser doppler velocimetry (Zetasizer Nano-ZS, Malvern Instruments, UK). For adjustment of the pH, acetic acid or ammonium hydroxide diluted ten times with ethanol in volume was used. The zeta potential of BSCF exhibited the highest value of +37 mV at pH 7 as shown in Fig. 2-2, suggesting that the suspension would be most stable at pH7. Therefore, the pH of the suspension was adjusted to 7.

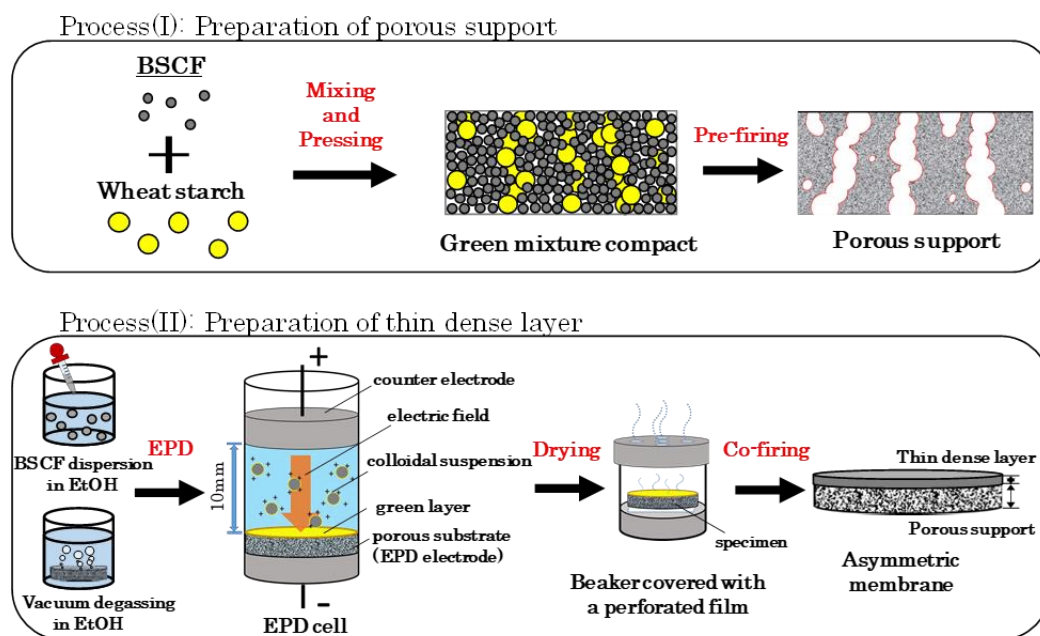


Fig. 2-1 Schematic illustrations showing the preparation procedure of the BSCF-based asymmetric membrane.

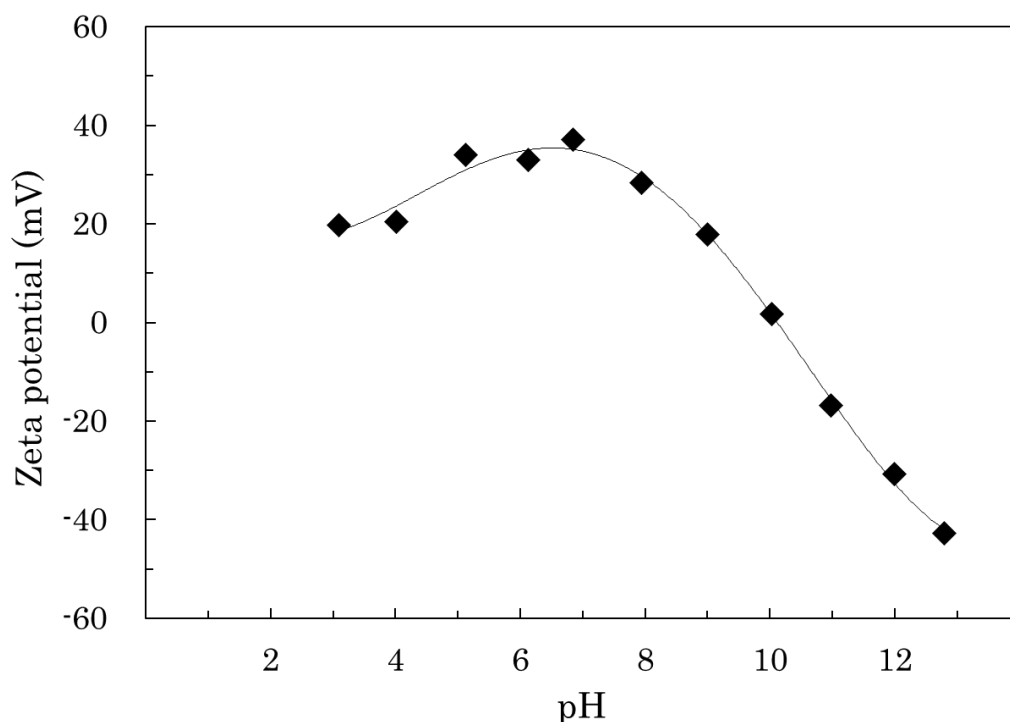


Fig. 2-2 Relation of zeta-potential of BSCF versus pH.

Figure 2-1, Process (II) shows a schematic illustration explaining the formation of a thin layer on a porous support by the EPD process. The electrode distance, the applied voltage and the deposition time were fixed at 10 mm, 150 V and 10 min, respectively. A 10-ml suspension was used for the fabrication of one layer. The porous support was degassed by solvent impregnation in a vacuum atmosphere before the EPD. The post-EPD specimens were slowly dried in a beaker covered with a perforated film, then co-fired at 800-1100 °C for 3 hours in air to densify the thin layer. The sintering behaviors of the porous support and the thin layer were separately characterized by dilatometry to determine the co-fired temperature at which cracking does not occur. The relative density of the porous support and green layer formed by the EPD were measured by the Archimedes method in kerosene. The microstructures of the fabricated membranes were

observed by scanning electron microscopy (SEM) using a field-emission SEM (JEOL, JSM-6500F) and a mini-SEM (Hitachi, TM-3000). The experimental setup for the measurement of the oxygen separation performance is schematically shown in [Fig. 3](#). The oxygen separation performances of the BSCF asymmetric membranes were evaluated at the constant flow rate of 200 ml/min for the air feed gas rate and 200 ml/min for the Ar sweep gas rate at fixed temperatures between 600 - 850 °C. The porous support was placed on the feed gas side. The membrane disc (diameter of 14 mm) was sealed to an aluminum tube using a silver ring at 900 °C. The permeated gas was analyzed by an oxygen sensor and gas chromatograph (G.C.). The nitrogen concentration in the permeated gas was monitored to make sure that no leakage of air occurred. It was confirmed by gas chromatography that the sample after the performance measurement remained gas tight even after cooling to room temperature.

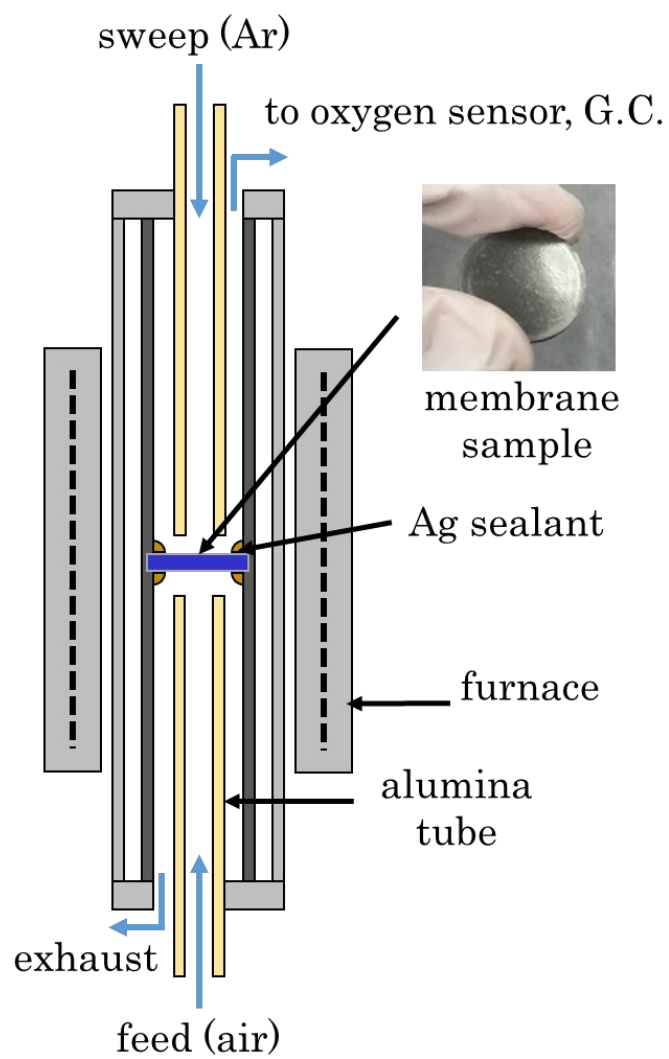


Fig. 2-3 Schematic of oxygen separation performance test.

3. Results and discussion

Figure 2-4 shows the relationship between the relative density and firing temperature of the BSCF molded body produced by a uniaxial molding method and the BSCF free-standing layer produced by the EPD method. The BSCF free-standing layer produced by the EPD method has not been subjected to the subsequent mechanical pressing treatment. Nevertheless, it showed a higher green density than that of the green compact prepared by 50 MPa uniaxial pressing. It was also shown that the sintered density of the EPD layer was equivalent to that of the uniaxially-pressed compact. Both samples were able to be densified to a relative density of 95% or more by sintering at a temperature of 1000 °C or higher. However, the BSCF heat treated at 1200 °C melted. In general, to maximize the conductivity of the solid electrolyte, the material should be densified to a relative density of 95% or higher. Therefore, a co-firing temperature of 1100 °C was considered to be optimal in order to densify a thin layer formed on a porous body.

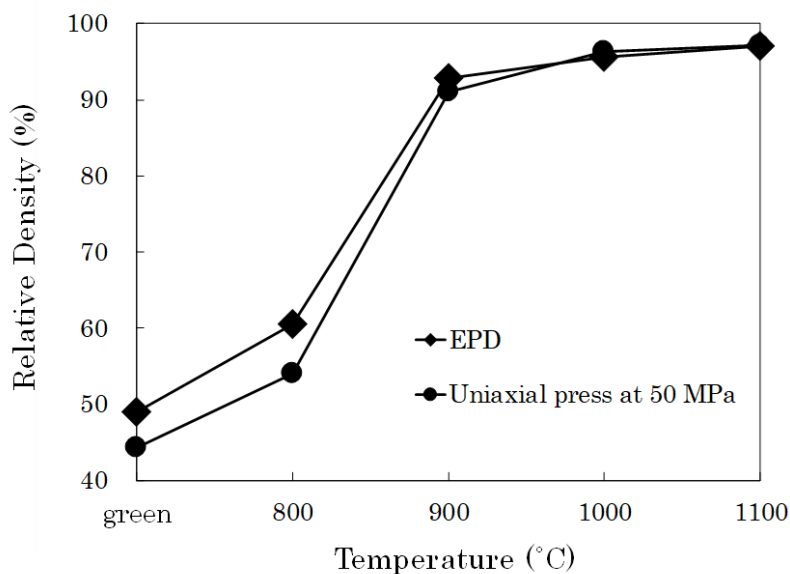


Fig. 2-4 Density change of the BSCF compacts by sintering in air.

Figure 2-5 shows the relationship of the porosity versus the amount of pore-forming agent for a porous support sintered at 1100 °C. Figure 2-6 shows SEM images of the microstructure of the porous supports sintered at 1100 °C prepared with different amounts of the pore-forming agent. The porosity of the BSCF support increased with the amount of starch. In the samples having a starch addition amount of 40 wt% and 50 wt%, the pores tended to be connected and coarsened, resulting in a very brittle property when used as a support and EPD electrode. Therefore, the optimum addition of the pore-forming agent was determined to be 30 wt%. In general, delamination and cracking caused by differences in the shrinkage are major problems for the production of layered composites by a co-firing process; therefore, it is necessary to make the heat shrinkage rates of both materials as close as possible. In our case, the pre-sintering temperature of the porous support should be optimized between 500 °C, which is the burnout temperature of the pore-forming agent, and 1100 °C, which is the co-firing temperature.

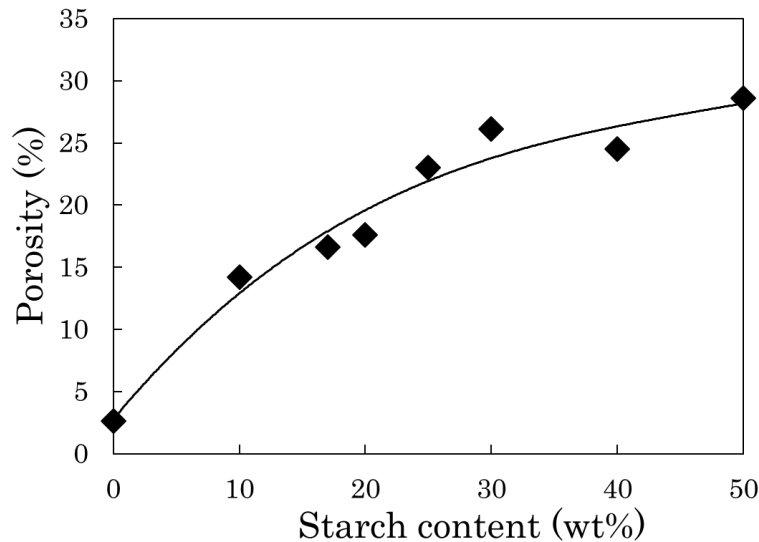


Fig. 2-5 Relationship between porosity of the porous body sintered at 1100 °C and starch content as the pore forming agent.

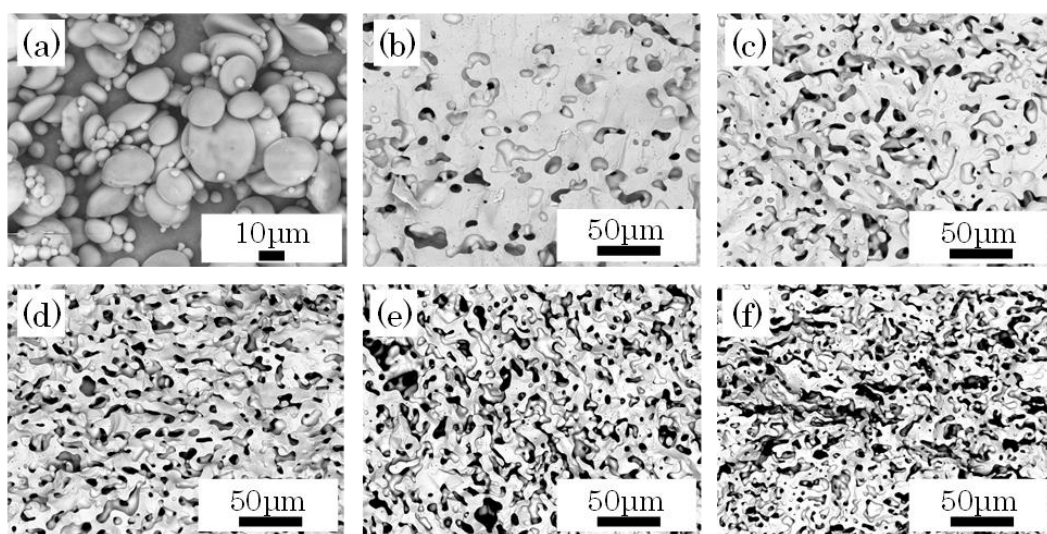


Fig. 2-6 SEM micrographs of (a) as-received wheat starch powder and porous BSCFs prepared with wheat starch of (b) 10wt%, (c) 20wt%, (d) 30wt%, (e) 40wt% and (f) 50wt%.

Figure 2-7 shows the relationship between the porosity and sintering temperature of the BSCF compacts to which 30 wt% of the pore-forming agent was added. At the pre-firing temperature of 500 °C, the porosity was 70% or more, and a large change was not seen up to around 800 °C, then it sharply dropped to about 30% at 1100 °C. In both the porous body and the EPD layer, sintering significantly progresses at 800 °C or higher. The thermal stress at the interface between the two during the co-sintering is also considered to mostly increase at 800 °C or higher. In order to reduce the thermal stress of the porous body pre-fired at different temperatures and the EPD layer, the thermal shrinkage during the heating process was evaluated.

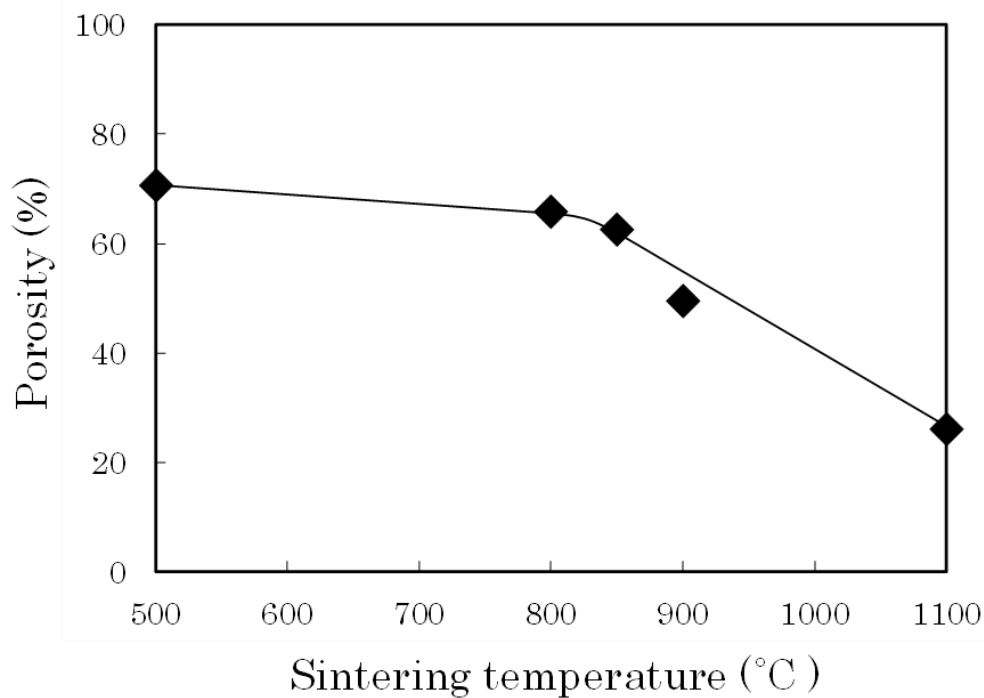


Fig. 2-7 Relation of porosity of BSCF porous support versus sintering temperature. Porous BSCFs were prepared with the addition of 30wt% wheat starch. Sintering at each fixed temperature was performed in air for 3h.

Figure 2-8 shows the dilatometric measurements during the heating process from room temperature to 1100 °C for the green EPD layer and the porous supports pre-fired at different temperatures. The sintering-shrinkage of the porous supports strongly depends on the pre-firing temperatures. The difference in the degree of contraction of the porous body and the EPD layer in this temperature range is a major factor causing the cracking and peeling. The porous support pre-fired at 500 °C had the lowest shrinkage mismatch with the EPD layer between 800-1000 °C. Based on these results, it was suggested that a crack-less, no peeling thin dense layer would be prepared on the porous support by setting the pre-firing temperature of the porous support to 500 °C and the co-firing temperature to 1100 °C.

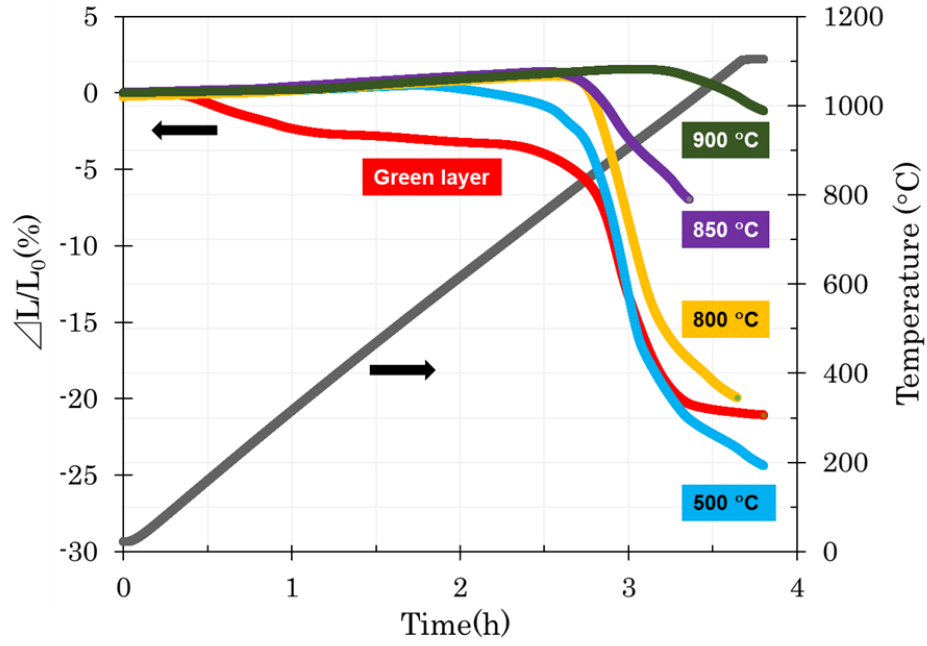


Fig. 2-8 Thermal shrinkage of BSCF compacts during heating at the constant rate of 5 °C/min

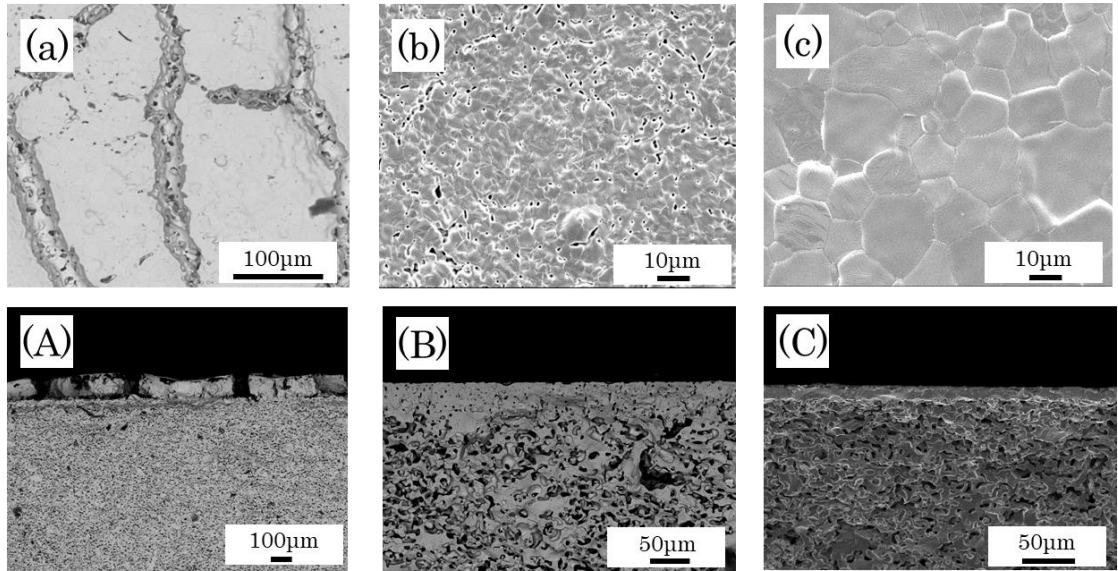


Fig. 2-9 Microstructures of the outer surfaces of the thin dense layers (a-c) as well as the fractured cross-section at the interfaces of the dense/porous BSCFs (A-C). The pre-firing temperatures were (a, A) 500 °C, (b, B) 800 °C, and (c, C) 900 °C. The co-firing temperature was fixed at 1100 °C for all the samples.

Figure 2-9 shows the outer surfaces of the thin dense layers as well as the fractured cross-sectional microstructures at the interfaces of the dense/porous BSCFs. Under the optimized sintering conditions, a dense layer of about 20- μm thickness without any cracking and peeling was successfully obtained. The interface between the dense layer and the porous support was well bonded. Figure 2-10 shows the comparison of the oxygen separation performances of a free-standing membrane fabricated by uniaxial pressing, an asymmetric membrane fabricated by the optimized EPD condition and the previously-reported asymmetric membrane with a similar film thickness prepared by the tape casting method [10,24]. In the inserted figure of Fig. 2-10, the logarithm of the oxygen permeability vs. temperature reciprocal is plotted for each sample. Since the Arrhenius plot showed linearity, the apparent activation energy was calculated. For the oxygen separation membrane using the perovskite-type MIEC, it has been reported that the rate-determining steps in the high and a low temperature regions are bulk diffusion and a surface exchange reaction, respectively [3,25,26]. The apparent activation energy of the former is lower than that of the latter. In this study, the temperature at which the surface exchange reaction control shifts to the bulk diffusion control is around 750 °C, which is almost similar to that reported in previous studies. Baumann et al. reported that the activation energies in the high and low temperature regions of BSCF are 32.0 kJ mol⁻¹ and 51.7 kJ mol⁻¹, respectively [27]. Their experiments were performed at different gas-flow rates, but the activation energies are almost similar to those of our results. The j_{O_2} of the asymmetric membrane prepared by EPD was comparable or higher than that by the tape casting [10,24]. The highest oxygen permeation flux of 2.5 ml (STP) min⁻¹cm⁻² was obtained at 850 °C for the asymmetric membrane prepared by EPD. In general, the EPD process does not limit the size and shape of the substrates,

therefore, the production of a long cylindrical asymmetric membrane would be easy. It is expected that the EPD method will significantly contribute to the widespread use of the oxygen separation system using the oxide ionic-electronic mixed conductors.

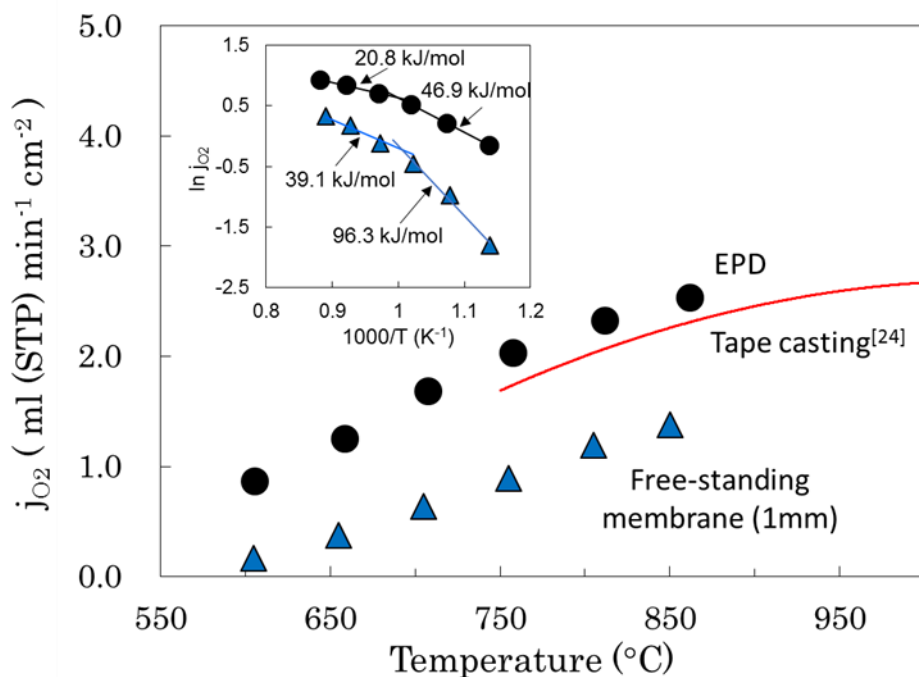


Fig. 2-10 Oxygen separation performance of BSCF membranes.

4. Conclusions

The EPD method was used for the fabrication of a dense/porous asymmetric oxygen separation membrane based on the BSCF mixed ionic-electronic conductor. The electric conductivity of the porous BSCF supports is satisfactorily high at room temperature, therefore, the BSCF powder was deposited onto porous BSCF supports without any surface treatment. Fabrication of a crack-free and non-peeling asymmetric membrane by the EPD method was successfully performed by minimizing the thermal stress

between the EPD layer and porous support during the co-firing. An asymmetric membrane composed of a thin dense layer with a relative density of 95% or more and a porous support with a porosity of about 30% exhibited an oxygen permeation flow rate of up to 2.5 ml (STP) min⁻¹ cm⁻² at 850 °C.

References

- [1] F. Vallejos-Burgos, F.X. Coudert, K. Kaneko, Air separation with graphene mediated by nanowindow-rim concerted motion, *Nat. Commun.* 9 (2018) 1–9. doi:10.1038/s41467-018-04224-6.
- [2] X. Zhu, W. Yang, *Mixed Conducting Ceramic Membranes: Fundamentals, Materials and Applications*, Springer US, 2017. doi:10.1007/978-3-662-53534-9.
- [3] J. Sunarso, S. Baumann, J.M. Serra, W.A. Meulenbergh, S. Liu, Y.S. Lin, J.C. Diniz da Costa, Mixed ionic-electronic conducting (MIEC) ceramic-based membranes for oxygen separation, *J. Memb. Sci.* 320 (2008) 13–41. doi:10.1016/j.memsci.2008.03.074.
- [4] M. Riaz, M. Abdullah Butt, Oxygen Transport Membranes and their Role in CO₂ Capture and Syngas Production, *J. Membr. Sci. Technol.* 08 (2018) 2–9. doi:10.4172/2155-9589.1000181.
- [5] T. Van Mai, J. Lovell, Impact of climate change, adaptation, and potential mitigation to Vietnam agriculture, 2016. doi:10.1007/978-3-319-14409-2_87.
- [6] V. V Kharton, A.A. Yaremchenko, E.N. Naumovich, Research on the electrochemistry of oxygen ion conductors in the former Soviet Union. II. Perovskite-related oxides, *J. Solid State Electrochem.* 3 (1999) 303–326.
- [7] W. Deibert, M.E. Ivanova, S. Baumann, O. Guillon, W.A. Meulenbergh, Ion-conducting ceramic membrane reactors for high-temperature applications, *J. Memb. Sci.* 543 (2017) 79–97. doi:10.1016/j.memsci.2017.08.016.
- [8] Y. Teraoka, H. Zhang, S. Furukawa, N. Yamazoe, Oxygen Permeation Through Perovskite-Type Oxide, *Chem. Lett.* (1985) 1743–1746.

- [9] Z. Shao, W. Yang, Y. Cong, J. Tong, G. Xiong, Investigation of the permeation behavior and stability of a $\text{Ba}_{0.5}\text{Sr}_{0.5}\text{Co}_{0.8}\text{Fe}_{0.2}\text{O}_{3-\delta}$ oxygen membrane, *J. Memb. Sci.* 172 (2000) 177–188. doi:10.1016/S0376-7388(00)00337-9.
- [10] P. Lemes-Rachadel, G.S. Garcia, R.A.F. Machado, D. Hotza, J.C.D. da Costa, Current developments of mixed conducting membranes on porous substrates, *Mater. Res.* 17 (2014) 242–249. doi:10.1590/S1516-14392013005000175.
- [11] G.R. Guillen, Y. Pan, M. Li, E.M. V Hoek, Preparation and Characterization of Membranes Formed by Nonsolvent Induced Phase Separation : A Review, *Ind. Eng. Chem. Res.* 50 (2011) 3798–3817. doi:10.1021/ie101928r.
- [12] H. Fang, C. Ren, Y. Liu, D. Lu, L. Winnubst, C. Chen, Phase-inversion tape casting and synchrotron-radiation computed tomography analysis of porous alumina, *J. Eur. Ceram. Soc.* 33 (2013) 2049–2051. doi:10.1016/j.jeurceramsoc.2013.02.032.
- [13] W. He, H. Huang, J. Gao, L. Winnubst, C. Chen, Phase-inversion tape casting and oxygen permeation properties of supported ceramic membranes, *J. Memb. Sci.* 452 (2014) 294–299. doi:10.1016/j.memsci.2013.09.063.
- [14] P. Colombo, J.R. Hellmann, Ceramic foams from preceramic polymers, (2002) 260–272. doi:10.1007/s10019-002-0209-z.
- [15] P. Ge, A. Vivet, L. Guironnet, N. Richet, F. Rossignol, T. Chartier, Perovskite foams used in combination with dense ceramic membranes for oxygen transport membrane applications, 44 (2018) 19831–19835. doi:10.1016/j.ceramint.2018.07.241.
- [16] T. Ohji, M. Fukushima, T. Ohji, M. Fukushima, Macro-porous ceramics: processing and properties Macro-porous ceramics: processing and properties,

- 6608 (2013). doi:10.1179/1743280411Y.0000000006.
- [17] Y. Sakka, T. Uchikoshi, Forming and microstructure control of ceramics by electrophoretic deposition (EPD), *KONA Powder Part. J.* 28 (2010) 74–90. doi:10.14356/kona.2010009.
- [18] L. Besra, M. Liu, A review on fundamentals and applications of electrophoretic deposition (EPD), *Prog. Mater. Sci.* 52 (2007) 1–61. doi:10.1016/j.pmatsci.2006.07.001.
- [19] Y. Fukada, N. Nagarajan, W. Mekky, Y. Bao, H. Kim, P.S. Nicholson, ELECTROPHORETIC DEPOSITION : FUNDAMENTALS AND APPLICATIONS Electrophoretic deposition — mechanisms, myths and materials, *J. Mater. Sci.* 39 (2004) 787–801.
- [20] A.R. Boccaccini, J.A. Roether, B.J.C. Thomas, M.S.P. Shaffer, E. Chavez, The Electrophoretic Deposition of Inorganic Nanoscaled Materials, *J. Ceram. Soc. Japan.* 14 (2006) 1–14.
- [21] P.S.N. Partho Sarkar, Electrophoretic Deposition (EPD): Mechanisms, Kinetics, and Application to Ceramics, *J. Am. Ceram. Soc.* 79 (1996) 1987–2002.
- [22] A.J. Moulson, J.M. Herbert, eds., *Electroceramics: Materials, Properties, Applications*, 2nd ed, WILEY, 2003.
- [23] T. Ishihara, K. Shimose, T. Kudo, H. Nishiguchi, T. Akbay, Y. Takita, Preparation of Yttria-Stabilized Zirconia Thin Films on Strontium-Doped LaMnO₃ Cathode Substrates via Electrophoretic Deposition for Solid Oxide Fuel Cells, *J. Am. Ceram. Soc.* 83 (2000) 1921–1927. doi:10.1111/j.1151-2916.2000.tb01491.x.
- [24] F. Schulze-Küppers, S. Baumann, W.A. Meulenbergh, D. Stöver, H.P.

- Buchkremer, Manufacturing and performance of advanced supported $\text{Ba}_{0.5}\text{Sr}_{0.5}\text{Co}_{0.8}\text{Fe}_{0.2}\text{O}_{3-\delta}$ (BSCF) oxygen transport membranes, *J. Memb. Sci.* 433 (2013) 121–125. doi:10.1016/j.memsci.2013.01.028.
- [25] K. Watanabe, M. Yuasa, T. Kida, K. Shimanoe, Y. Teraoka, N. Yamazoe, Preparation of oxygen evolution layer/ $\text{La}_{0.6}\text{Ca}_{0.4}\text{CoO}_3$ dense membrane/porous support asymmetric structure for high-performance oxygen permeation, *Solid State Ionics*. 179 (2008) 1377–1381. doi:10.1016/j.ssi.2007.12.092.
- [26] K. Watanabe, M. Yuasa, T. Kida, K. Shimanoe, Y. Teraoka, N. Yamazoe, Dense/porous asymmetric-structured oxygen permeable membranes based on $\text{La}_{0.6}\text{Ca}_{0.4}\text{CoO}_3$ perovskite-type oxide, *Chem. Mater.* 20 (2008) 6965–6973. doi:10.1021/cm8013144.
- [27] S. Baumann, J.M. Serra, M.P. Lobera, S. Escolástico, F. Schulze-küppers, W.A. Meulenbergh, Ultrahigh oxygen permeation flux through supported $\text{Ba}_{0.5}\text{Sr}_{0.5}\text{Co}_{0.8}\text{Fe}_{0.2}\text{O}_{3-\delta}$ membrane, *J. Memb. Sci.* 377 (2011) 198–205. doi:10.1016/j.memsci.2011.04.050.

Chapter 3 | Fabrication of BSCF multi-layered oxygen separation membrane using sequential electrophoretic deposition process

Preface

In the previous chapter, the EPD process was applied to the fabrication of an oxygen separation membrane with an asymmetric structure composed of a dense layer / porous support based on BSCF. As a result, sufficiently high oxygen separation characteristics were shown compared with the BSCF asymmetric membranes reported so far, and the effectiveness of the EPD process was demonstrated. The asymmetric-structured membrane can promote the oxygen reduction reaction due to the high specific surface area of the porous support layer. In order to increase the area for sufficient oxygen generation reaction on the sweep side, it is preferable to form a porous MIEC layer on the dense MIEC layer as well. In this chapter, the fabrication of tri-layered structure, composed of an porous oxygen-evolution layer / dense oxide ion-transporting layer / porous oxygen-reduction support in which a porous oxygen evolution layer is formed on an asymmetric structure, has been attempted expecting improved oxygen separation performance compared to a bi-layered structure composed of dense layer / porous support.

1. Introduction

As the methods for forming a bi-layer composed of porous oxygen-evolution layer / dense oxide ion-transporting layer on a porous oxygen-reduction support, spin coating, dip coating and tape casting have been reported very often[1–9]. However, there are few reports on film formation of such a bi-layer only by the EPD method[10–13]. When producing a laminated body by EPD method, it is common to perform EPD sequentially

by changing the suspension for each layer[14–21]. In order to form a bi-layer consisting of a porous layer / dense layer in a single sintering process, a suspension composed of only the base material must be used for the first layer, and a suspension composed of the base material and pore former must be used for the second layer. At this time, in the formation of the second layer, the two kinds of particles must be uniformly co-deposited to obtain a porous layer having a uniform pore distribution. In that case, a major problem is that the suspension for forming the first layer is mixed into the suspension for forming the second layer. Using the cylindrical cell reported in the previous chapter, a suspension containing a minimum amount of particles necessary for forming a film thickness required for each layer was injected into the cell. By doing EPD in this way, concentration unevenness and contamination of the suspensions were prevented.

In this study, in order to obtain the above-mentioned bi-layered structure by sequential EPD followed by co-sintering, the dispersion control of the BSCF and polymethyl methacrylate (PMMA) particles, and the EPD deposition conditions were examined.

2. Experimental methods

Figure 3-1, Process (I) shows a schematic illustration explaining the preparation procedure of the porous support. $\text{Ba}_{0.5}\text{Sr}_{0.5}\text{Co}_{0.8}\text{Fe}_{0.2}\text{O}_{3-\delta}$ (BSCF) prepared by the citrate precursor method with a D50 particle size of $0.55\ \mu\text{m}$ (Kusaka Rare Metal Products Co., Ltd.) and wheat starch as the pore-forming agent with a particle size of $1\text{--}30\ \mu\text{m}$ (Nakarai Tesque, Inc.) were used. The BSCF powder and pre-determined ratio (30 wt%) of the starch powders were mixed in a mortar. The powder mixture was uniaxially pressed into a disc with a 1.0mm thickness and 28mm diameter, then pre-fired at $500\ ^\circ\text{C}$ for 1 hours

to obtain a porous support. To prepare the suspension of EPD for the forming dense layer, the BSCF powder thermal-treated at 250 °C for 30 min, was dispersed in reagent-grade ethanol (0.6 g/ 100 ml), then ultrasonicated. The zeta potential of the suspension was measured by laser doppler velocimetry (Zetasizer Nano-ZS, Malvern Instruments, UK). For adjustment of the pH, acetic acid or ammonium hydroxide diluted ten times with ethanol in volume was used. The zeta potential of thermal-treated BSCF exhibited the highest value of +53 mV at pH 7 as shown in Fig. 3-2, suggesting that the suspension would be most stable at pH7. Therefore, the pH of the suspension was adjusted to 7. The EPD suspension for the porous layer is composed of heat-treated BSCF and Polymethyl methacrylate (PMMA) as a pore former, 0.3 g each in 100 ml ethanol. The EPD suspension for the porous layer was also prepared in the same procedure as for the dense layer.

Figure 3-1, Process (II) shows a schematic illustration explaining the formation of a thin layer on a porous support by the EPD process. The electrode distance, the applied voltage and the deposition time were fixed at 10 mm, 150 V and 10 min, respectively. A 10-ml suspension was used for the fabrication of one layer. The porous support was degassed by solvent impregnation in a vacuum atmosphere before the EPD. The post-EPD specimens were slowly dried in a beaker covered with a perforated film, then co-fired at 1100 °C for 3 hours in air to densify the thin layer. The sintering behaviors of the porous support and the thin layer were separately characterized by dilatometry to determine the co-fired temperature at which cracking does not occur. The relative density of the porous support and green layer formed by the EPD were measured by the Archimedes method in kerosene. The microstructures of the fabricated membranes were observed by scanning electron microscopy (SEM) using a field-emission SEM (JEOL,

JSM-7600F) and a mini-SEM (Hitachi, TM-3000). The oxygen separation performances of the BSCF asymmetric membranes were evaluated at the constant flow rate of 200 ml/min for the air feed gas rate and 200 ml/min for the Ar sweep gas rate at fixed temperatures between 600 - 850 °C. The porous support was placed on the feed gas side. The membrane disc (diameter of 14 mm) was sealed to an aluminum tube using a silver ring at 900 °C. The permeated gas was analyzed by an oxygen sensor and gas chromatograph (G.C.). The nitrogen concentration in the permeated gas was monitored to make sure that no leakage of air occurred. It was confirmed by gas chromatography that the sample after the performance measurement remained gas tight even after cooling to room temperature.

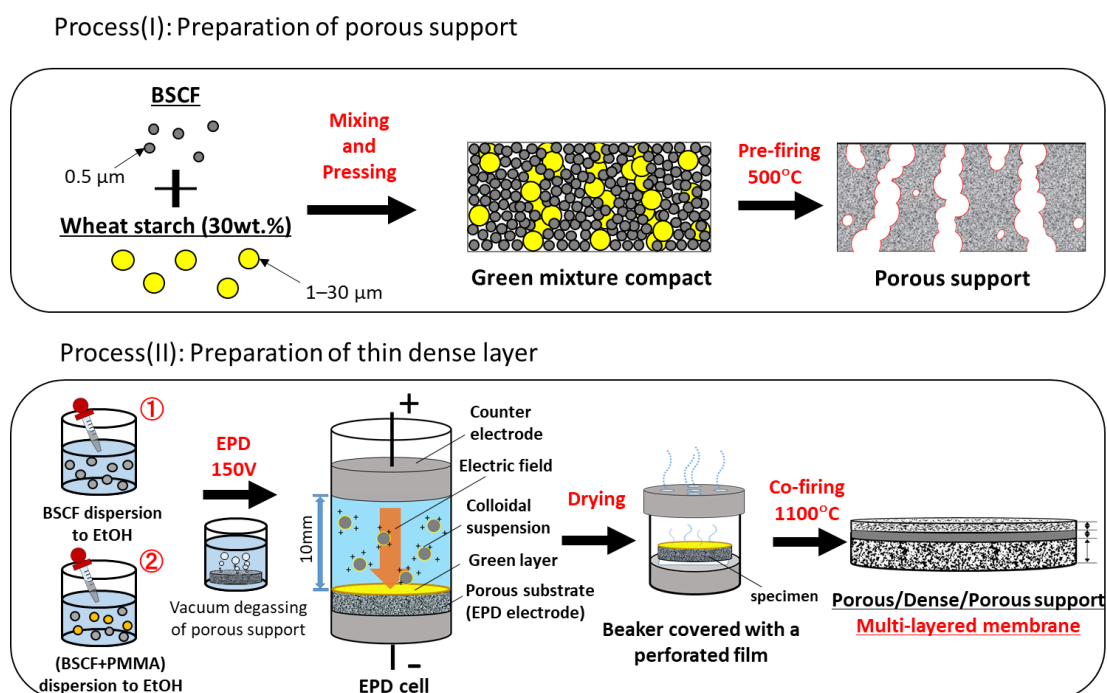


Fig. 3-1 Schematic illustrations showing the preparation procedure of the BSCF-based multi-layered membrane

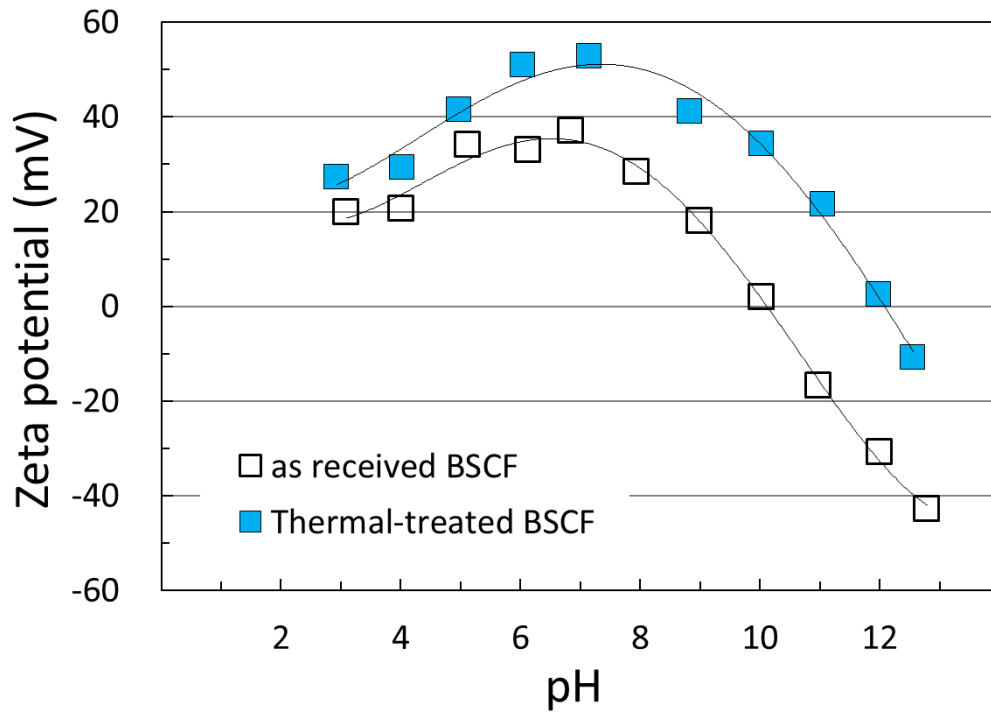


Fig. 3-2 Zeta potential of thermal-treated BSCF

3. Results and Discussion

Figure 3-3 shows the pH dependence of the change in the microstructure of the layer after the co-firing. Since the pore distribution was the most uniform in the pH 7 porous layer, it is considered that BSCF and PMMA were uniformly deposited. The porous layer at pH 5 had a non-uniform pore distribution compared to that at pH 7. Further, the oxygen generation layer having pH 3 was peeled off at the interface with the dense layer, and a portion where no porous layer was formed was observed.

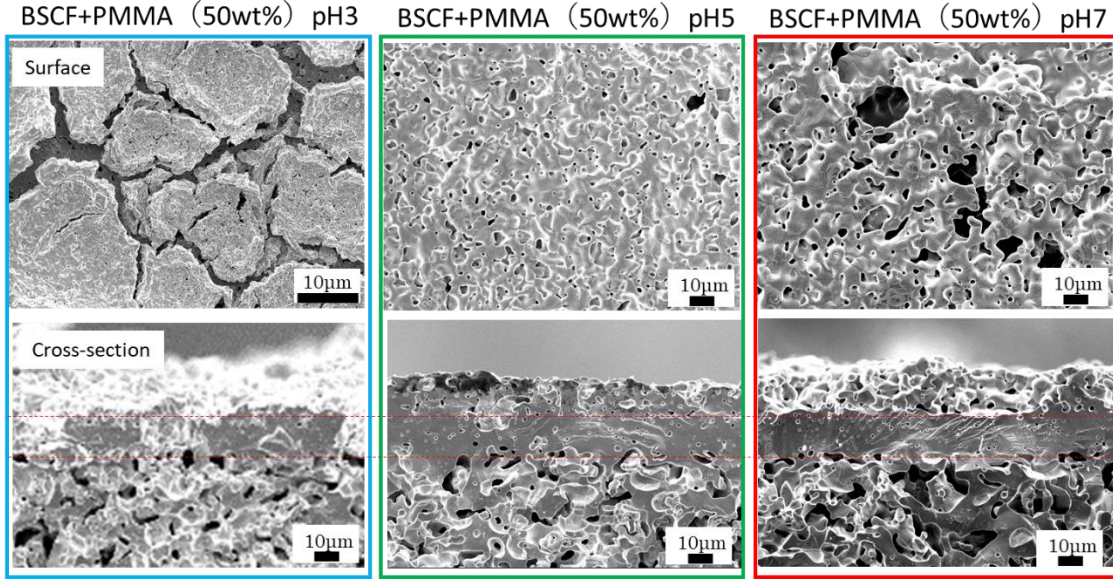


Fig. 3-3 pH dependence of the change in the microstructure of the layer after the co-firing.

These results were examined from the principle of electrophoresis. For the binary slurry, Hückel's equation representing the electrophoretic deposition rate and Stokes' equation representing the gravity sedimentation rate are shown below

$$v = [(\varepsilon_0 \varepsilon_r) \zeta / 18 \eta^2] E \quad (3-1)$$

$$v = \frac{[d^2 (\rho_p - \rho_w) g]}{18 \eta} \quad (3-2)$$

here, ε_0 is the vacuum permittivity, ε_r is the relative permittivity of the solvent, ζ is the zeta potential, η is the solution viscosity, E is the electric field, d is the particle size, ρ_p is solute density, ρ_w is the solvent density, g is the gravitational acceleration. Based on the electrophoretic velocity equation, the difference in the electrophoretic velocity of the two components depends only on the zeta potential. For example, when the zeta potentials are the same, the electrophoretic speeds coincide with each other, and

conversely, a speed difference is generated by the difference between the zeta potentials. On the other hand, the gravitational settling speed depends on the density of the dispersoids because the average particle sizes of BSCF and PMMA are the same. BSCF has an average particle size of 0.5 μm and a theoretical density of 5.72 g/cm^3 , and PMMA has an average particle size of 0.5 μm and a theoretical density of 1.18 g/cm^3 . When calculating the respective gravity settling rates, the settling rate of BSCF is about 3 times higher than that of PMMA. Therefore, in this study, the applied electric field was set sufficiently high so that the electrophoretic velocity could be neglected.

Figure 3-4 shows the relation of zeta-potential of BSCF and PMMA versus pH. Based on this formula, the zeta potential of the two components at pH 7 is almost the same, and the migration speed of the particles is almost the same, so that a porous layer having a uniform pore distribution could be formed. The difference between the two zeta potentials is bigger at pH 5 than pH 3, resulting in a greater difference in electrophoretic speed. Pore distribution is uneven and coarse pores are observed at the interface with the dense layer, so the PMMA concentration may vary from the dense layer to the porous layer surface. Finally, at pH 3, there is a large gap in the zeta potential of each other, and the electrophoretic speed of PMMA is much faster than that of BSCF. Therefore, PMMA is preferentially deposited on the interface with the dense layer interface, which is thought to have led to peeling of the deposited layer after co-firing.

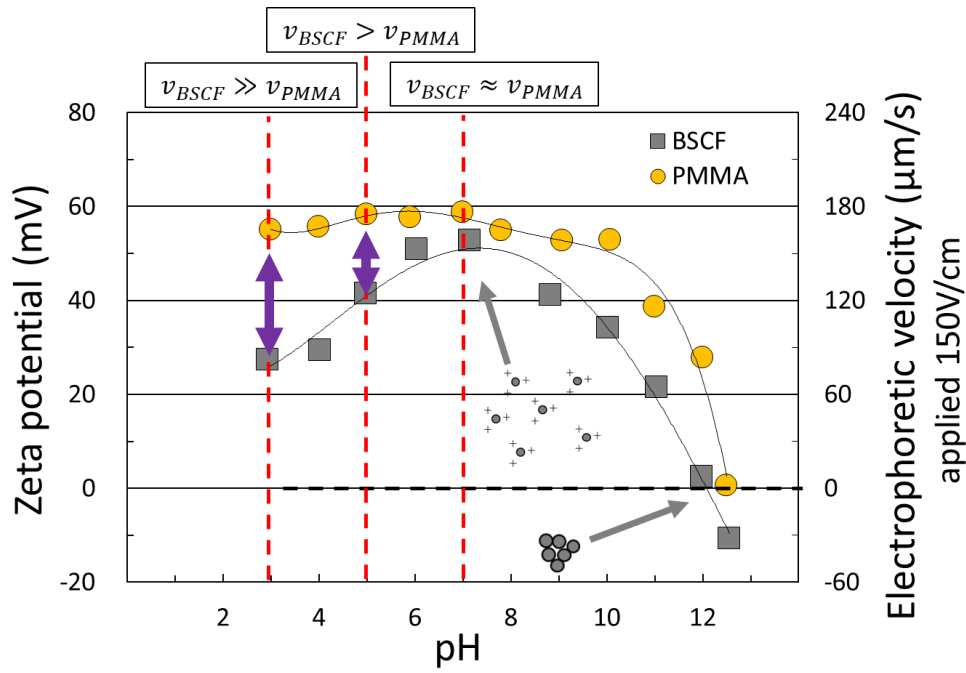


Fig. 3-4 Relation of zeta-potential of BSCF and PMMA versus pH.

Figure 3-5 shows the microstructure of the porous layer after co-firing with respect to the added amount of PMMA at a pH 7 where the migration speed of the two components is uniform. As the amount of PMMA added increased, the number of pores in the porous layer increased. In the porous layer with an added amount of PMMA of 10 wt%, Although the distribution of pores was uniform, there were many isolated pores because the amount of pore-forming material was small to form continuous pores. The porous layer with 30 wt% PMMA increased the pore connectivity. However, it was insufficient for pores to connect from the interface with the dense layer to the surface. Finally, in the porous layer added with 50 wt% PMMA, the pore distribution was uniform and closed pores were not observed, and a structure in which the base material formed a three-dimensional network was observed. Therefore, a sample with a suspension pH 7 and an added amount of PMMA of 50 wt% was used for the oxygen separation characteristics test under the conditions examined in this study.

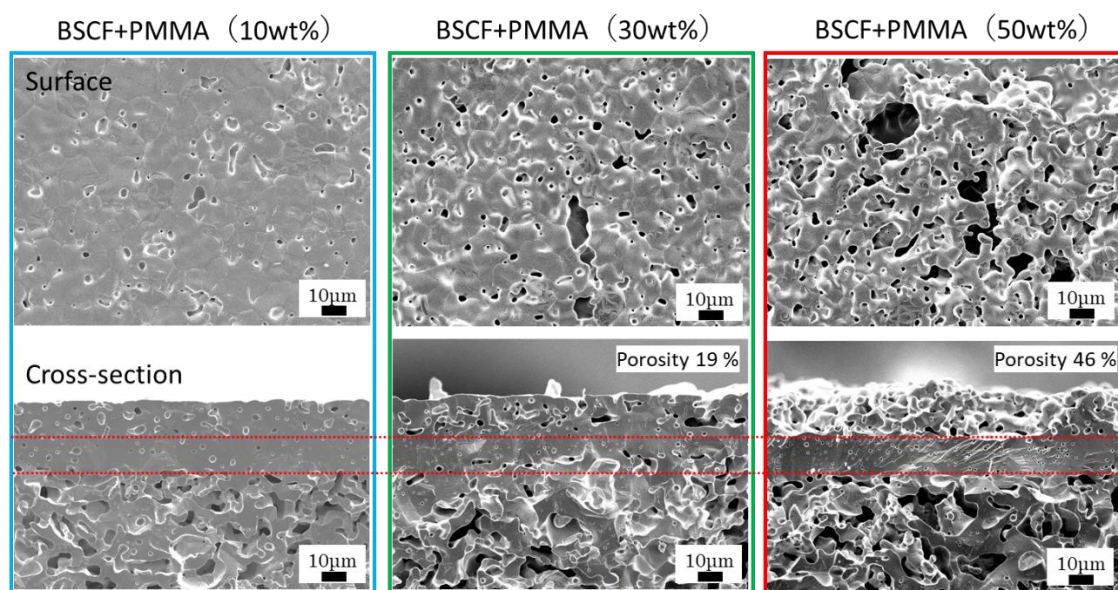


Fig. 3-5 The dependence of the amount of PMMA on the microstructure of the porous layer

4. Conclusions

In this study, we tried to deposit a porous layer / dense layer on porous support by sequential electrophoretic deposition. In the co-deposition of two components by EPD, the difference between the two zeta potentials and the concentration ratio of BSCF and PMMA were investigated as process parameters. Based on the electrophoretic velocity equation, it was clarified that the two components can be deposited uniformly by forming a film under conditions where the zeta potential is sufficiently high and the difference is as small as possible. As a result, it was shown that a porous layer having a uniform pore distribution can be formed by uniformly depositing and firing two components of BSCF as a base material and PMMA as a pore former. Moreover, it was suggested that an EPD layer with a concentration gradient can be formed by using the difference in zeta potential. It was also suggested that the porosity of the porous layer can be controlled by

changing the concentration ratio of BSCF and PMMA under conditions where the two components are uniformly deposited. From the above results, when applying the EPD method as a method for forming a porous layer, it was an essential factor in using the difference in the zeta potential and the concentration ratio for control the microstructure.

References

- [1] B. He, D. Ding, Y. Ling, J. Xu, L. Zhao, Efficient modification for enhancing surface activity of $\text{Ba}_{0.5}\text{Sr}_{0.5}\text{Co}_{0.8}\text{Fe}_{0.2}\text{O}_{3-\delta}$ oxygen permeation membrane, *J. Memb. Sci.* 477 (2015) 7–13. <https://doi.org/10.1016/j.memsci.2014.12.020>.
- [2] P.L. Rachadel, J. Motuzas, R.A.F. Machado, D. Hotza, J.C. Diniz da Costa, Influence of porous structures on O_2 flux of BSCF asymmetric membranes, *Sep. Purif. Technol.* 175 (2017) 164–169. <https://doi.org/10.1016/j.seppur.2016.10.053>.
- [3] K. Watanabe, M. Yuasa, T. Kida, K. Shimanoe, Y. Teraoka, N. Yamazoe, Preparation of oxygen evolution layer/ $\text{La}_{0.6}\text{Ca}_{0.4}\text{CoO}_{3-\delta}$ dense membrane/porous support asymmetric structure for high-performance oxygen permeation, *Solid State Ionics*. 179 (2008) 1377–1381. <https://doi.org/10.1016/j.ssi.2007.12.092>.
- [4] S. Baumann, J.M. Serra, M.P. Lobera, S. Escolástico, F. Schulze-Küppers, W.A. Meulenbergh, Ultrahigh oxygen permeation flux through supported $\text{Ba}_{0.5}\text{Sr}_{0.5}\text{Co}_{0.8}\text{Fe}_{0.2}\text{O}_{3-\delta}$ membranes, *J. Memb. Sci.* 377 (2011) 198–205. <https://doi.org/10.1016/j.memsci.2011.04.050>.
- [5] J.M. Serra, J. Garcia-Fayos, S. Baumann, F. Schulze-Küppers, W.A. Meulenbergh, Oxygen permeation through tape-cast asymmetric all- $\text{La}_{0.6}\text{Sr}_{0.4}\text{Co}_{0.2}\text{Fe}_{0.8}\text{O}_{3-\delta}$ membranes, *J. Memb. Sci.* 447 (2013) 297–305. <https://doi.org/10.1016/j.memsci.2013.07.030>.
- [6] J.H. Park, E. Magnone, J.P. Kim, S.H. Choi, Oxygen permeation performance of $\text{Ba}_{0.5}\text{Sr}_{0.5}\text{Co}_{0.8}\text{Fe}_{0.2}\text{O}_{3-\delta}$ membrane after surface modification, *Korean J. Chem. Eng.* 29 (2012) 235–242. <https://doi.org/10.1007/s11814-011-0153-y>.
- [7] H.J.M. Bouwmeester, Dense ceramic membranes for methane conversion, *Catal. Today*. 82 (2003) 141–150. [https://doi.org/10.1016/S0920-5861\(03\)00222-0](https://doi.org/10.1016/S0920-5861(03)00222-0).
- [8] W.K. Hong, G.M. Choi, Oxygen permeation of BSCF membrane with varying

- thickness and surface coating, *J. Memb. Sci.* 346 (2010) 353–360.
<https://doi.org/10.1016/j.memsci.2009.09.056>.
- [9] A. V. Kovalevsky, A.A. Yaremchenko, V.A. Kolotygin, F.M.M. Snijkers, V. V. Kharton, A. Buekenhoudt, J.J. Luyten, Oxygen permeability and stability of asymmetric multilayer $\text{Ba}_{0.5}\text{Sr}_{0.5}\text{Co}_{0.8}\text{Fe}_{0.2}\text{O}_{3-\delta}$ ceramic membranes, *Solid State Ionics*. 192 (2011) 677–681. <https://doi.org/10.1016/j.ssi.2010.05.030>.
- [10] H.A. Rahman, A. Muchtar, N. Muhamad, H. Abdullah, Influence of Processing Parameters on Electrophoretically Deposited $\text{La}_{0.6}\text{Sr}_{0.4}\text{Co}_{0.2}\text{Fe}_{0.8}\text{O}_{3-\delta}$ Films, *Key Eng. Mater.* 462–463 (2011) 148–153.
<https://doi.org/10.4028/www.scientific.net/KEM.462-463.148>.
- [11] A. Nakamura, S. Ishihara, S. Nakamura, Syntheses and Evaluation of Porous ZrO_2 Ceramics by Electrophoretic Deposition Method, *J. Ceram. Soc. Japan*. 115 (2007) 383–387.
- [12] S. Hayashi, F. Oguri, F. Kagaya, Preparation of Composite Film by Simultaneous Electrophoretic Deposition Using Titanium Oxide Nanoparticles and Submicron-sized Aluminium Oxide Particles, *J. Soc. Powder Technol., Japan*. 51 (2014) 686–693.
- [13] T. Yoshioka, A. Chávez-Valdez, J.A. Roether, D.W. Schubert, A.R. Boccaccini, AC electrophoretic deposition of organic-inorganic composite coatings, *J. Colloid Interface Sci.* 392 (2013) 167–171. <https://doi.org/10.1016/j.jcis.2012.09.087>.
- [14] B. Ferrari, A. Bartret, C. Baudín, Sandwich materials formed by thick alumina tapes and thin-layered alumina-aluminium titanate structures shaped by EPD, *J. Eur. Ceram. Soc.* 29 (2009) 1083–1092.
<https://doi.org/10.1016/j.jeurceramsoc.2008.07.048>.
- [15] B. Kieback, A. Neubrand, H. Riedel, Processing techniques for functionally graded materials, *Mater. Sci. Eng. A*. 362 (2003) 81–105.

[https://doi.org/10.1016/S0921-5093\(03\)00578-1](https://doi.org/10.1016/S0921-5093(03)00578-1).

- [16] S. Bonnas, H.J. Ritzhaupt-Kleissl, J. Haußelt, Fabrication of particle and composition gradients by systematic interaction of sedimentation and electrical field in electrophoretic deposition, *J. Eur. Ceram. Soc.* 30 (2010) 1177–1185.
<https://doi.org/10.1016/j.jeurceramsoc.2009.08.007>.
- [17] T. Uchikoshi, Fabrication of Inorganic Nano-Material by Electrophoretic Deposition, *J. Soc. Inorg. Mater. Japan.* 8 (2001) 478–483.
- [18] I. Corni, M.P. Ryan, A.R. Boccaccini, Electrophoretic deposition: From traditional ceramics to nanotechnology, *J. Eur. Ceram. Soc.* 28 (2008) 1353–1367. <https://doi.org/10.1016/j.jeurceramsoc.2007.12.011>.
- [19] Y. Fukada, N. Nagarajan, W. Mekky, Y. Bao, H. Kim, P.S. Nicholson, ELECTROPHORETIC DEPOSITION : FUNDAMENTALS AND APPLICATIONS Electrophoretic deposition — mechanisms , myths and materials, *J. Mater. Sci.* 39 (2004) 787–801.
- [20] J. Cihlar, D. Drdlik, Z. Cihlarova, H. Hadraba, Effect of acids and bases on electrophoretic deposition of alumina and zirconia particles in 2-propanol, *J. Eur. Ceram. Soc.* 33 (2013) 1885–1892.
<https://doi.org/10.1016/j.jeurceramsoc.2013.02.017>.
- [21] L. Besra, M. Liu, A review on fundamentals and applications of electrophoretic deposition (EPD), *Prog. Mater. Sci.* 52 (2007) 1–61.
<https://doi.org/10.1016/j.pmatsci.2006.07.001>.

Chapter 4 | Fabrication of BSCF porous body with excellent pore connectivity

Preface

The porous support prepared by the conventional sacrificial template method has a problem that the open porosity is not always sufficiently high for the supply gas to permeate to the dense layer. The formed closed pores would not contribute to the surface exchange reaction. To fabricate a porous body having high open porosity, the gelatinization-retrogradation phenomenon of starch has been to produce a porous body with high air permeability. In this chapter, a novel production method using the gelatinization-retrogradation phenomenon of starch as a pore-forming material has been demonstrated in order to develop a porous material with excellent connectivity that can be applied to porous support of the oxygen separation membrane.

1. Introduction

Porous ceramics are often used in various applications such as thermal insulation, adsorbents, filters, gas sensors, and catalyst supports [1]. In particular, a porous body using a mixed ionic-electronic conductor (MIEC) is used as an electrode of solid oxide electrochemical cells such as a solid oxide fuel cell or a porous support of an oxygen separation membrane. In these porous ceramics, it is very important to design the porosity, microstructure and mechanical properties according to the applications. In order to sufficiently promote the electrode reaction, the MIEC porous body must have a percolated network structure in which raw materials, such as a reaction gas, can easily reach the surface of the electrolyte or separation membrane layer [2–4]. Moreover, it

must have a large specific surface area as a reaction field. Typical fabrication processes for macroporous ceramics include partial sintering, sacrificial templates, replica templates and direct foaming. In addition to these fabrication processes, many new approaches for macroporous ceramics, such as phase separation and three-dimensional printing (3D printing), have been developed [1,5–9]. In particular, sacrificial template method [3,10–13], tape casting method [2,4,14–17], phase inversion method [18], and freeze-drying method [19] have been reported for the fabrication method of porous BSCF.

For the fabrication of a conventional porous body, like the sacrificial template method, a mixed powder in which pore-forming agent particles are uniformly dispersed in a matrix material, is shaped, followed by removal of the pore-forming agent before, during or after sintering of the matrix material. A wide variety of sacrificial materials have been used as pore formers, including natural and synthetic organics, salts, liquids, metals, and ceramic compounds [9]. However, even if the pore forming agent material is uniformly dispersed in the matrix material, closed pores are generally formed if the amount of the pore-forming material is not sufficient as shown in Fig. 4-1(a).

Many porous ceramics using starch powders as a pore forming agent have been reported [4,20-30]. In the conventional method, various plant-derived starch particles suitable for the target pore shape have been used in their original states. By using starch particles as a pore-forming material, a good porous body without any residue can be obtained by firing at about 500 °C. However, simply using starch powder as a substitute for polymer beads, such as polystyrene and PMMA, is not always a good method to form a percolated pore network.

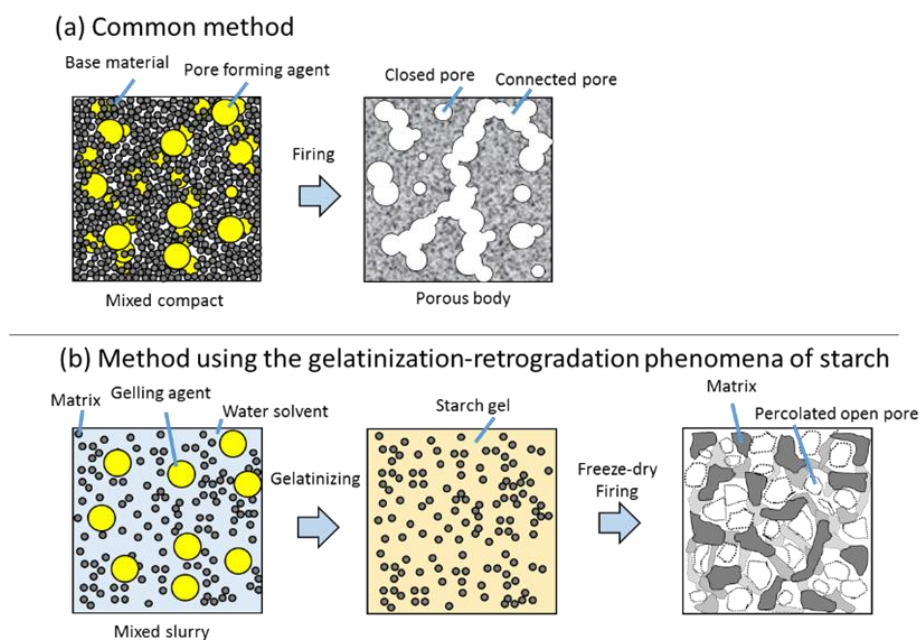


Fig. 4-1 Schematic illustrations showing the preparation of a porous body by the sacrificial template method

Starch is a polysaccharide composed of amylose and amylopectin produced by the photosynthesis of plants, and is a granular solid, and the ratio and shape of the particles differ depending on the type of plant. Figure 4-2 shows a schematic illustration of the gelatinization and retrogradation of starch [31–36]. The amylose and amylopectin fractions become loose during heating and in the presence of excess water, and these fractions start to solubilize at 70 °C and 90 °C, respectively. Starch granules initially absorb water causing them to gradually swell and form a viscous slurry. As heating continues and the temperature increases, the granules start losing their crystallinity and become amorphous. Subsequent heating causes the granules size to increase until they can no longer absorb more water and burst. As molecules making up the granule start to leach out from the swollen granules and disperse/solubilize in the aqueous

medium, they yield a gel or paste whose properties depend on the concentration and type of the starch. Retrogradation begins immediately after stopping the heating. Retrogradation of the amylopectin is a slow process, on the other hand, amylose retrogrades very quickly during cooling. The gelatinized starch then starts to cool to ambient temperature and solidifies, leading to water separation and molecular realignment. Retrogradation is associated with recrystallization of the starch molecules.

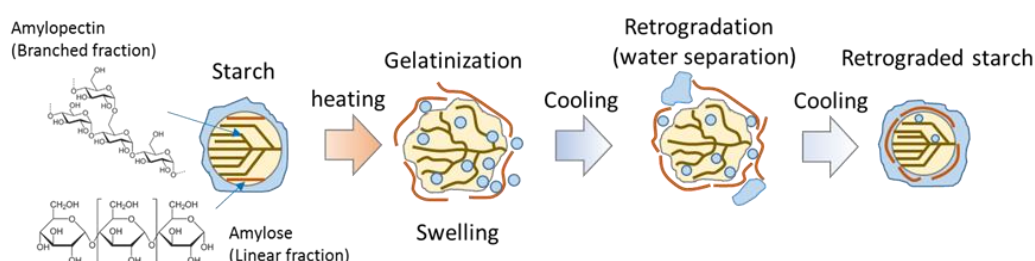


Fig. 4-2 Phenomena of starch gelatinization and retrogradation

When an aqueous slurry in which starch powder, which is a pore-forming agent, and the matrix material powder are dispersed, is heated, the starch is gelatinized and connected to each other. This starch consolidation technique has been reported in which the starch powder is swollen by heating a mixture of starch and matrix material in an aqueous slurry to form a connected pore network [37–43]. We have recently devised a method for fabricating a porous support using the gelatinization and successive retrogradation phenomena of starch. We postulated that it would be possible to produce porous materials with an excellent pore connectivity using these phenomena as shown in Fig. 4-1(b). The purpose of this study is to produce a porous material with an excellent pore connectivity and electrical conductivity based on the $(\text{Ba,Sr})(\text{Co,Fe})\text{O}_{3-\delta}$ (BSCF) mixed conductor by utilizing the gelatinization-retrogradation phenomena of starch.

2. Materials and methods

Figure 4-3 shows a schematic illustration explaining the preparation procedure of the porous bodies. Five vol% of $\text{Ba}_{0.5}\text{Sr}_{0.5}\text{Co}_{0.8}\text{Fe}_{0.2}\text{O}_{3-\delta}$ (BSCF) powder (Kusaka Rare Metal Products Co., Ltd.) with an average particle size of $0.5\ \mu\text{m}$ was added to distilled water. Next, rice starch powder (Sigma-Aldrich Co. LLC) with the particle size range of $2.0\text{--}8.0\ \mu\text{m}$ was added to the slurry in an amount of 25 wt% versus the BSCF powder. The mixed slurry was deflocculated using an ultrasonic homogenizer. Next, the resulting slurry was heated and stirred at about $65\ ^\circ\text{C}$ for 1 h using a hot stirrer to gelatinize the rice starch in the slurry. This slurry was poured into an acrylic cylindrical container standing on a metal plate, then the sample was cooled in a refrigerator at $0\pm 2\ ^\circ\text{C}$ for 2h to accelerate the retrogradation and the exudation of moisture in the gelatinized starch. Furthermore, the sample was gradually frozen at $-18\ ^\circ\text{C}$ or rapidly frozen at $-196\ ^\circ\text{C}$ with liquid nitrogen, then freeze-dried under a reduced pressure of 10 Pa to obtain green bodies.

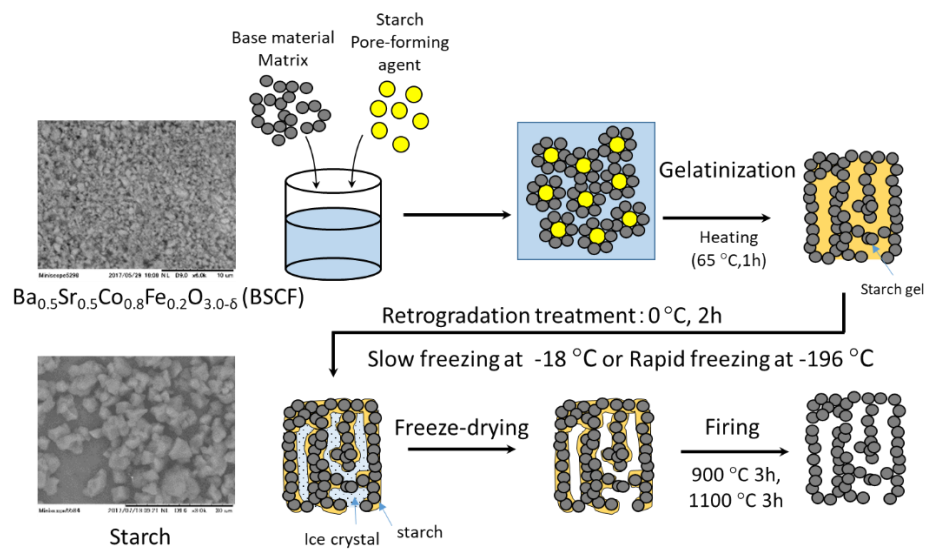


Fig. 4-3 Preparation procedure of porous body of BSCF using rice starch as the pore forming agent.

Figure 4-4 shows SEM micrographs of (a) the as-received starch powder, (b) the gelatinized starch after freeze-drying, and (c) retrograded starch after freeze-drying. The sacrificial templates of the starch, like these images, would be formed. Thereafter, the green bodies were fired at 900 °C or 1100 °C for 3 hours to produce the BSCF porous bodies. The porosity of the green bodies and porous bodies were measured by the Archimedes' method in kerosene. The microstructures of the sample were observed by scanning electron microscopy (SEM) using a field-emission SEM (JEOL, JSM-6510) and a tabletop-SEM (Hitachi, TM-3000). The electrical conductivity of the porous bodies sintered at 1100 °C was evaluated by the DC 2-terminal method using a source meter (Keithley, model 2400).

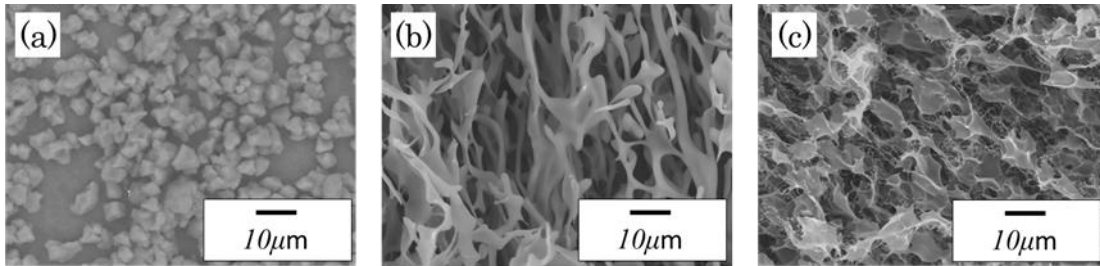


Fig. 4-4. SEM images of (a) as-received rice starch powder, (b) freeze-dried gelatinized starch and (c) freeze-dried retrograded starch.

3. Results and discussion

Fig. 4-5 shows the microstructure of the green bodies after freeze-drying. Table 4-1 shows the retrogradation progress, porosity and the apparent pore size of each sample. The green body (Fig. 4-5(a)), which was rapidly frozen at -196 °C and vacuum freeze-dried with no retrogradation treatment, showed an open porosity of 57.6%. The green body (Fig. 4-5(b)),

which was rapidly frozen at $-196\text{ }^{\circ}\text{C}$ and vacuum freeze-dried with the retrogradation treatment, showed an open porosity of 77.6%, and the pore size range was $5.0\text{--}10.0\text{ }\mu\text{m}$. The green body (Fig. 4-5(c)), which was slowly frozen at $-18\text{ }^{\circ}\text{C}$ and vacuum freeze-dried with the retrogradation treatment, showed an open porosity of 87.8%, and the pore size range was $10.0\text{--}50.0\text{ }\mu\text{m}$.

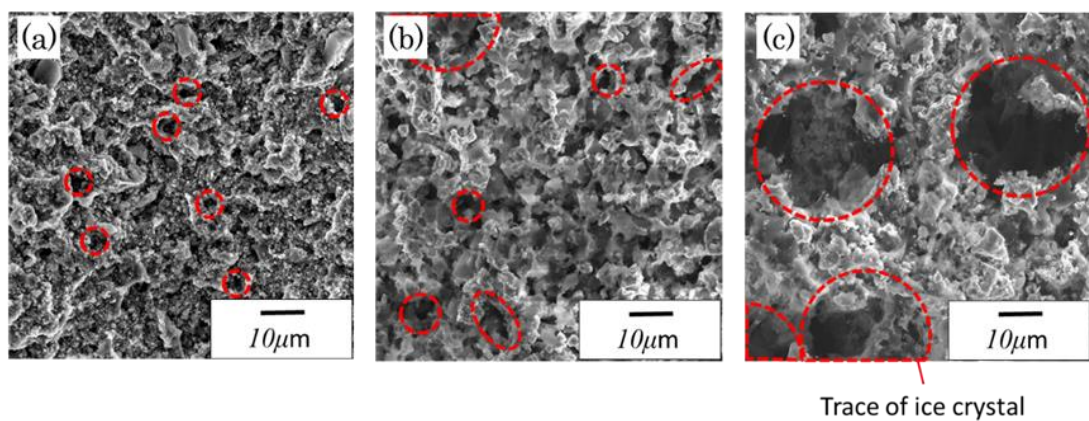


Fig. 4-5 Microstructures of the green bodies after freeze-drying (a-c): (a) no retrogradation treatment + rapid freezing, (b) retrogradation treatment + rapid freezing, and (c) retrogradation treatment + slow freezing.

Table 4-1 The degree of retrogradation progress, porosity and the pore size of green bodies after freeze-drying: (a) no retrogradation treatment + rapid freezing, (b) retrogradation treatment + rapid freezing, and (c) retrogradation treatment + slow freezing.

| Sample | (a) | (b) | (c) |
|-----------------------------------|-------|------------|-------------|
| Degree of retrogradation progress | small | medium | Large |
| Porosity (%) | 57.6 | 77.6 | 87.8 |
| Pore size (μm) | $5 <$ | $5\sim 25$ | $10\sim 50$ |

In the rapidly frozen and then freeze-dried samples (Figure 4-5 (a) and (b)), a difference in the microstructure of the green bodies was observed depending on whether aging was promoted. This is probably because the exuded water from the gelatinized starch was frozen during the retrogradation process, and voids were formed by the ice crystals sublimating by the freeze drying. In addition, in the rapidly frozen and slowly frozen samples followed by the retrogradation treatment (Figure 4-5 (b) and (c)), a difference in the microstructure of the green bodies was also observed depending on whether aging was promoted. This is likely because in the case of the slow freeze, not only the exudate during the retrogradation treatment, but more water will be exuded during the subsequent freezing process. When the sample is rapidly frozen at liquid nitrogen temperature, the time for water exudation from the gelatinized tissue is extremely short, and the amount of water to be exuded is relatively small, resulting in the formation of fine ice crystals, thus smaller pores. On the other hand, the freezing rate of water at -18°C is slow, therefore, there is sufficient time for more water to exudate out, resulting in the formation of large ice crystals and consequently coarse pores.

Figures 4-6 (a-c) and (A-C) show SEM images of the fractured surfaces of the porous bodies produced by firing the green bodies of Figs. 4-5 (a) to (c) at 900°C or 1100°C , respectively. Figure 6 (A'-C') are the wide-area images of Figure 6 (A-C). The sample prepared by firing the green body at 900°C is not shown here because the sample was too brittle to observe the microstructure. When the porous body shown in Fig. 4-5 (c) was fired at 1100°C (Fig. 4-6 (C)), a high open porosity was obtained, but the brittleness was not improved. When the rapidly frozen compacts shown in Figs. 4-6 (a) and (b) were fired at 900°C , the pores were uniformly distributed and favorably connected regardless of

the retrogradation treatment as shown in Figs. 4-6 (a) and (b). In the porous bodies fired at 1100 °C, it was observed that the sample with the non-retrogradation treatment (Fig. 4-6 (A)) had a significantly reduced porosity compared to the other samples (Fig. 4-6 (B) and (C)). This is probably because the sintering between the particles progressed as the firing temperature increased, and the pores of 0.5–5.0 μm in size, which were observed in the porous body fired at 900 °C, shrunk, and the connected structure was lost. On the other hand, in the porous body that was retrograded, then fired at 900 °C, the pores of 5.0–10 μm size were maintained as shown in Fig. 4-6 (b). Furthermore, even at the 1100 °C firing, connected pores having a range of 2.0–8.0 μm were retained as shown in Figs. 4-6 (B) and (C). Based on these results, it is considered that the pore size of the retrograded sample increased due to the more exuding from the gelatinized starch, resulting in the formation of coarse pores as compared to the non-gelatinized sample.

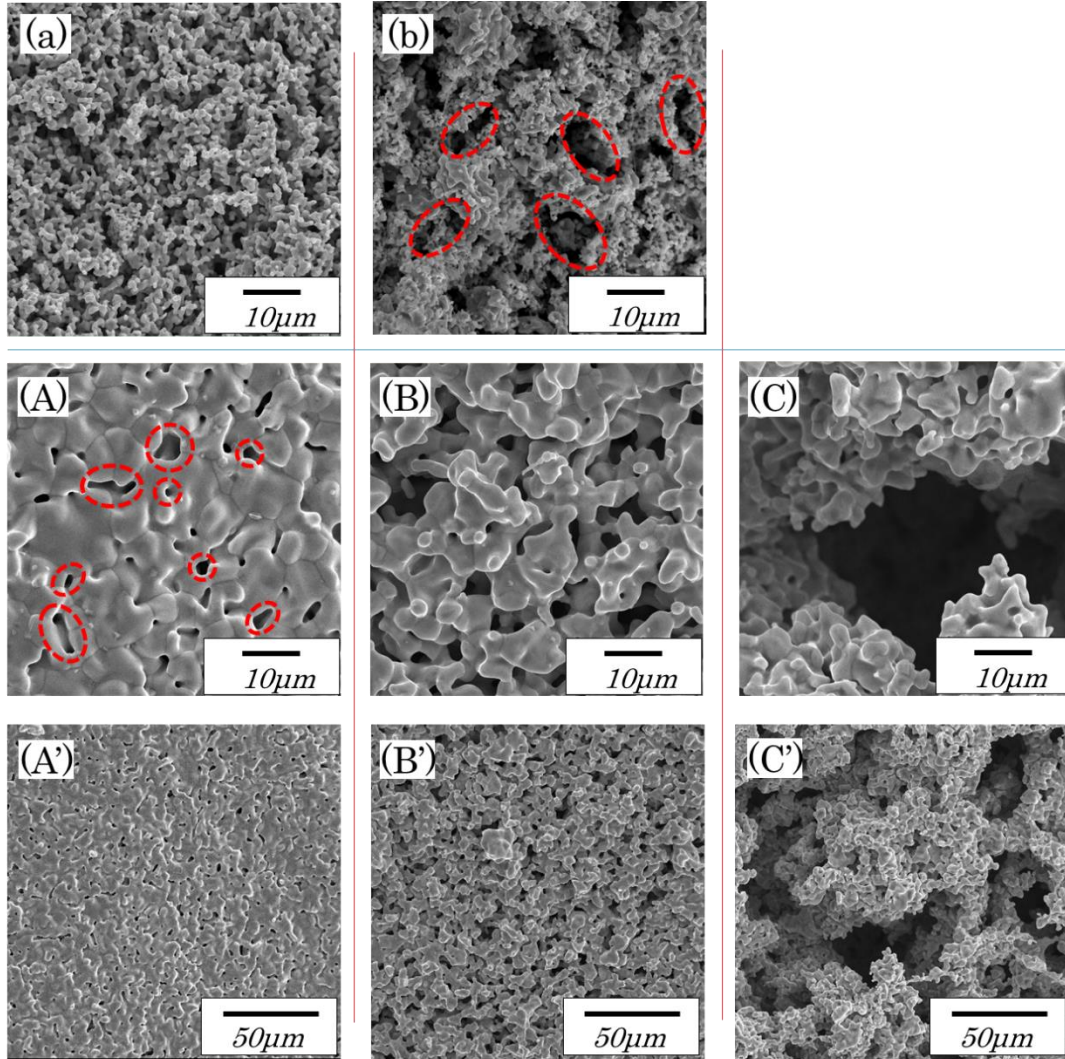


Fig. 4-6 Microstructures of the porous bodies fired at 900 °C (a-b) and 1100 °C (A-C): (a, A) no retrogradation treatment + rapid freezing, (b, B) retrogradation treatment + rapid freezing, and (c, C) retrogradation treatment + slow freezing. (A'-C') are the wide-area images of (A-C).

Figure 4-7 shows the microstructure of (a) the dense body produced by the uniaxial pressure molding method, (b) the porous body by the conventional method, and (c) the porous body by freeze drying followed by firing at 1100 °C. Table 4-2 shows the porosity, apparent pore size, and electrical conductivity of each sample. Porous bodies prepared by this technique have a pore size similar to that of the conventional methods, but have a higher porosity, and 99% of the total pores are open pores. The electrical conductivity of the porous body obtained by this method was similar to that of the porous body prepared by the conventional method, and the connectivity of the matrix was sufficiently high as well as the connectivity of the pores.

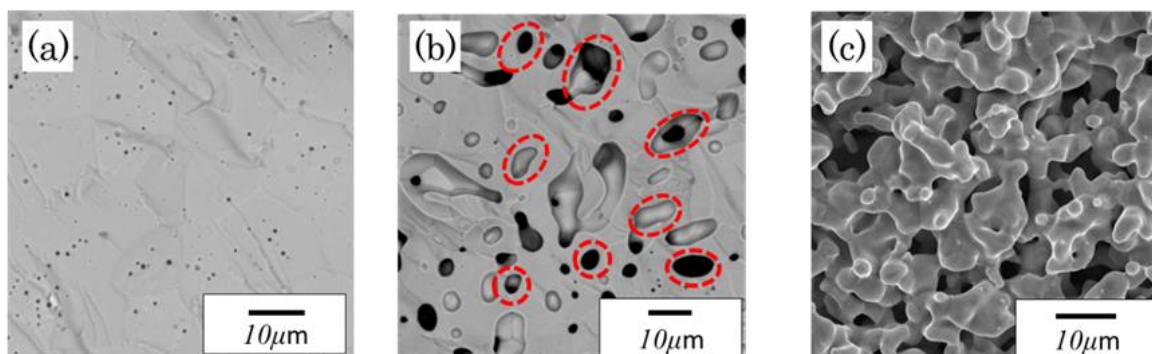


Fig. 4-7 Microstructures of the BSCFs sintered at 1100 °C via different preparation methods: (a) uniaxial pressing without pore forming agent, (b) common sacrificial template method, and (c) method using the gelatinization-retrogradation phenomena of starch (retrogradation treatment + rapid freezing). The added amounts of starch in (b) and (c) are both 25 wt%.

Table 4-2 Porosity, open porosity, pore size, electrical conductivity of the BSCFs sintered at 1100 °C via different preparation methods: (a)uniaxial pressing without pore forming agent, (b) common sacrificial template method, and (c) method using the gelatinization-retrogradation phenomena of starch (retrogradation treatment + rapid freezing). The added amounts of starch in (b) and (c) are both 25 wt%.

| Sample | (a) | (b) | (c) |
|--------------------------------|---------------------|-----------------------|-----------------------|
| Porosity (%) | 2.8 | 21.8 | 48.4 |
| Open porosity (%) | 0 | 7.9 | 48.3 |
| Pore size (μm) | < 5.0 | 5.0 ~ 10.0 | 5.0 ~ 10.0 |
| Electrical conductivity (S/cm) | 26×10^{-3} | 1.42×10^{-3} | 1.97×10^{-3} |

In general, the pore structure is evaluated by gas adsorption, mercury intrusion, and X-ray CT. In the pore distribution measurement by the gas adsorption method, the range in which the pores can be measured is 0.1 to 100 nm, which is not suitable for the measurement of the pore diameter of the porous BSCF prepared in this study. In the mercury intrusion method, pores with a diameter of several nm to several hundred μm are measured. However, in this method, a cylindrical pore is a measurement target and is not suitable for the measurement of a three-dimensional network structure in which many pores are connected. Therefore, we tried to observe the pore structure of the sample by X-ray CT. Although the maximum measurable resolution of the instrument was 5 μm, observation of the pore structure of this sample was difficult, and visualization of the pore shape and three-dimensional network structure was not possible.

To confirm that the fabricated porous BSCF has excellent pore connectivity, a high-precision specific surface area measurement using krypton gas was performed. The specific surface area measurement results were: 0.24 m²/g for rapidly frozen samples

without retrogradation treatment (Fig.6 (A)), 0.27 m²/g for rapidly frozen samples with retrogradation treatment (Fig.6(B)), 0.07 m²/g for samples prepared by the sacrificial template method (Fig.7 (c)), 8.6 m²/g for BSCF raw powder. The specific surface area in which the porous bodies produced by utilizing the gelatinization and retrogradation phenomena after sintering (Fig.6 (A and B)) were smaller than that of the raw powder. However, the specific surface area of these porous bodies was 3 to 4 times higher than that of the porous body prepared by the sacrificial template method (Fig.7 (c)). Further, the sample of Fig.6 (B) with retrogradation treatment had a higher specific surface area than the sample of Fig.6 (A) without no retrogradation treatment. This suggests that the sample in Fig. 6(B) has a high open porosity, which is consistent with the porosity measurements. The wide-area SEM image shown in Fig. 6 (A'-C') exhibits that the porous bodies produced by utilizing the gelatinization and retrogradation phenomena have a highly connective pore structure. These results of specific surface area measurement, porosity measurement, and SEM observation show that the porous body formed by using the gelatinization and retrogradation phenomena forms a network structure with a highly connective pore structure.

Figure 4-8 shows the relationship between the porosity and the firing temperature of the porous materials prepared under different conditions. The porosity of the non-retrograded sample increased due to the 900 °C firing and decreased at 1100 °C. Considering that the burnout temperature of starch is around 500 °C and the starting temperature of the sintering of BSCF is around 900 °C, the reason why the porosity increased by firing at 900 °C is probably because the densification does not significantly progress. At the firing temperatures of 1000 °C or higher, the densification further proceeds, so that the pores diminish and the porosity decreases. On the other hand, the

porosity of the retrograded sample slightly decreased at 900 °C, and further decreased by firing to 1100 °C. This is probably because the coarse pores hinder the sintering progress of the matrix.

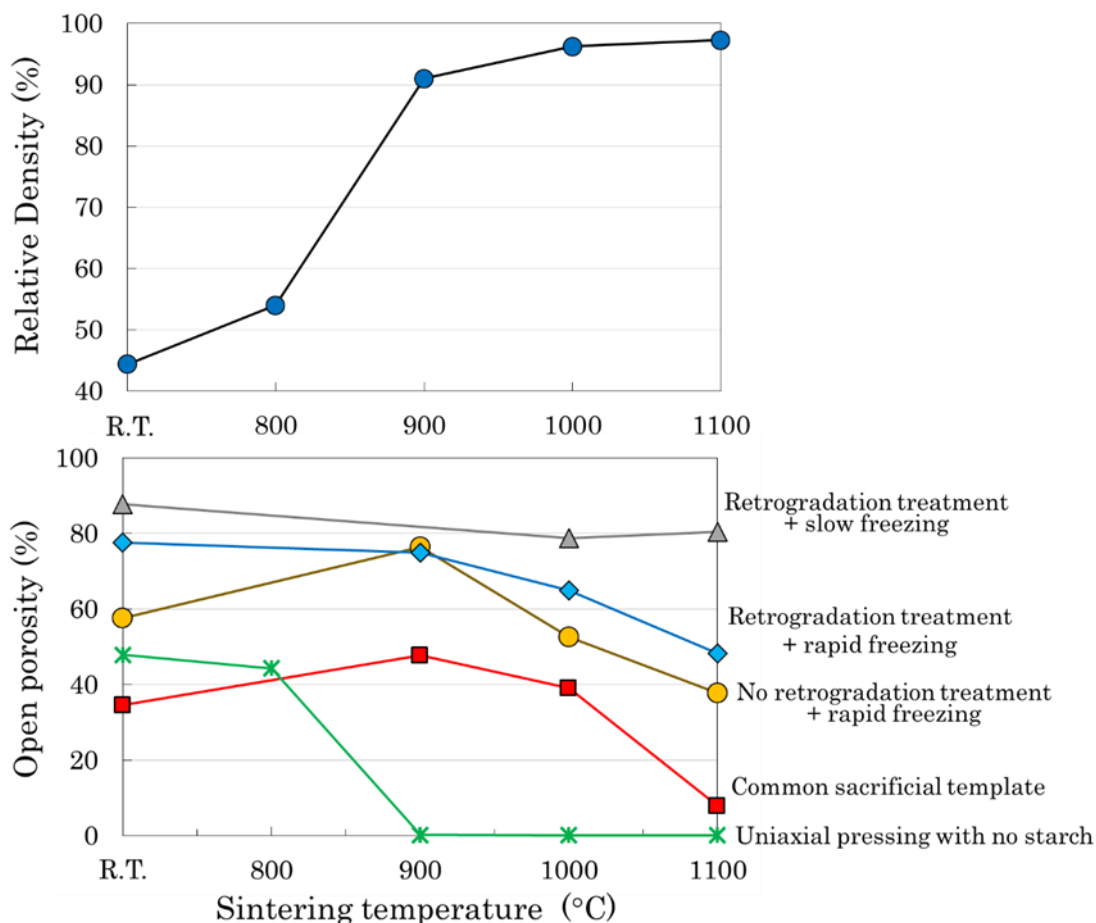


Fig. 4-8 Sintering properties of the BSCFs: (upper side) Relative density of BSCF with no starch prepared by uniaxial pressing; (lower side) open porosity of the sintered bodies prepared by different methods and conditions.

In this study, rice-derived starch was used, but using starch from other plants with different ratios of amylose and amylopectin would result in the formation of pores with different tissue structures. The method of producing a porous body using the

gelatinization-retrogradation phenomena of starch is a promising method with excellent environmental compatibility for producing a porous body with excellent connectivity, which can be applied to other matrix materials.

4. Conclusions

A new processing method for producing porous materials has been proposed by selecting the combination of rice starch and BSCF; i.e., starch powder as a pore-forming agent is gelatinized to connect them together and promote the appropriate retrogradation phenomenon to freeze the exuded water, and subsequent vacuum freeze-drying the ice crystal and firing. Consequently, connected pores having a pore diameter such that pores formed later would not disappear due to heat shrinkage are formed, and a porous body of BSCF having an excellent open porosity is produced.

References

- [1] T. Ohji, M. Fukushima, Macro-porous ceramics : processing and properties, *Int. Mater. Rev.* **57** (2012) 115–131. doi:10.1179/1743280411Y.0000000006.
- [2] P. Niehoff, S. Baumann, F. Schulze-Küppers, R.S. Bradley, I. Shapiro, W.A. Meulenbergh, P.J. Withers, R. Vaßen, Oxygen transport through supported $\text{Ba}_{0.5}\text{Sr}_{0.5}\text{Co}_{0.8}\text{Fe}_{0.2}\text{O}_{3-\delta}$ membranes, *Sep. Purif. Technol.* **121** (2014) 60–67. doi:10.1016/j.seppur.2013.07.002.
- [3] P.L. Rachadel, J. Motuzas, G. Ji, D. Hotza, J.C. Diniz da Costa, The effect of non-ionic porous domains on supported $\text{Ba}_{0.5}\text{Sr}_{0.5}\text{Co}_{0.8}\text{Fe}_{0.2}\text{O}_{3-\delta}$ membranes for O_2 separation, *J. Memb. Sci.* **454** (2014) 382–389. doi:10.1016/j.memsci.2013.11.054.
- [4] F. Schulze-Küppers, S. Baumann, W.A. Meulenbergh, D. Stöver, H.P. Buchkremer, Manufacturing and performance of advanced supported $\text{Ba}_{0.5}\text{Sr}_{0.5}\text{Co}_{0.8}\text{Fe}_{0.2}\text{O}_{3-\delta}$ (BSCF) oxygen transport membranes, *J. Memb. Sci.* **433** (2013) 121–125. doi:10.1016/j.memsci.2013.01.028.
- [5] D.D. Athayde, D.F. Souza, A.M.A. Silva et. al., Review of perovskite ceramic synthesis and membrane preparation methods, *Ceram. Int.* **42** (2016) 6555–6571. doi:10.1016/j.ceramint.2016.01.130.
- [6] R.K. Nishihora, P.L. Rachadel, M.G.N. Quadri, D. Hotza, Manufacturing porous ceramic materials by tape casting—A review, *J. Eur. Ceram. Soc.* **38** (2018) 988–1001. doi:10.1016/j.jeurceramsoc.2017.11.047.
- [7] N. Sarkar, I.J. Kim, Porous Ceramics, in: A.M.. Mohamed (Ed.), *Adv. Ceram. Process.*, IntechOpen, 2015: pp. 55–84.
- [8] U.M. Basheer, A Brief Introduction to Porous Ceramic, in: U.M. Basheer (Ed.),

- Recent Adv. Porous Ceram., IntechOpen, 2018: pp. 1–10. doi:10.5772/68104.
- [9] R. Studart, U.T. Gonzenbach, E. Tervoort, L.J. Gauckler, Processing Routes to Macroporous Ceramics: A Review, *J. Am. Ceram. Soc.* 89 (2006) 1771–1789. doi:10.1111/j.1551-2916.2006.01044.x.
- [10] D.A. Slade, Q. Jiang, K.J. Nordheden, S.M. Staggs-Williams, A comparison of mixed-conducting oxygen-permeable membranes for CO₂ reforming, *Catal. Today*. 148 (2009) 290–297. doi:10.1016/j.cattod.2009.08.016.
- [11] A. V. Kovalevsky, A.A. Yaremchenko, V.A. Kolotygin, A.L. Shaula, V. V. Kharton, F.M.M. Snijders, A. Buekenhoudt, J.R. Frade, E.N. Naumovich, Processing and oxygen permeation studies of asymmetric multilayer Ba_{0.5}Sr_{0.5}Co_{0.8}Fe_{0.2}O_{3-δ} membranes, *J. Memb. Sci.* 380 (2011) 68–80. doi:10.1016/j.memsci.2011.06.034.
- [12] X. Cui, R. O'Hayre, S. Pylypenko, L. Zhang, L. Zeng, X. Zhang, Z. Hua, H. Chen, J. Shi, Fabrication of a mesoporous Ba_{0.5}Sr_{0.5}Co_{0.8}Fe_{0.2}O_{3-δ} perovskite as a low-cost and efficient catalyst for oxygen reduction, *Dalt. Trans.* 46 (2017) 13903–13911. doi:10.1039/c7dt03082g.
- [13] B. He, D. Ding, Y. Ling, J. Xu, L. Zhao, Efficient modification for enhancing surface activity of Ba_{0.5}Sr_{0.5}Co_{0.8}Fe_{0.2}O_{3-δ} oxygen permeation membrane, *J. Memb. Sci.* 477 (2015) 7–13. doi:10.1016/j.memsci.2014.12.020.
- [14] M. Lipinska-Chwalek, J. Malzbender, A. Chanda, S. Baumann, R.W. Steinbrech, Mechanical characterization of porous Ba_{0.5}Sr_{0.5}Co_{0.8}Fe_{0.2}O_{3-δ}, *J. Eur. Ceram. Soc.* 31 (2011) 2997–3002. doi:10.1016/j.jeurceramsoc.2011.07.002.
- [15] S. Baumann, J.M. Serra, M.P. Lobera, S. Escolástico, F. Schulze-Küppers, W.A. Meulenbergh, Ultrahigh oxygen permeation flux through supported

- Ba_{0.5}Sr_{0.5}Co_{0.8}Fe_{0.2}O_{3-δ} membranes, *J. Memb. Sci.* 377 (2011) 198–205.
doi:10.1016/j.memsci.2011.04.050.
- [16] X. Li, T. Kerstiens, T. Markus, Oxygen permeability and phase stability of Ba_{0.5}Sr_{0.5}Co_{0.8}Fe_{0.2}O_{3-δ} perovskite at intermediate temperatures, *J. Memb. Sci.* 438 (2013) 83–89. doi:10.1016/j.memsci.2013.03.017.
- [17] M. Lipinska-Chwalek, F. Schulze-Küppers, J. Malzbender, Stability aspects of porous Ba_{0.5}Sr_{0.5}Co_{0.8}Fe_{0.2}O_{3-δ}, *Ceram. Int.* 40 (2014) 7395–7399.
doi:10.1016/j.ceramint.2013.12.085.
- [18] A. Kovalevsky, C. Buysse, F. Snijkers, A. Buekenhoudt, J. Luyten, J. Kretzschmar, S. Lenaerts, Oxygen exchange-limited transport and surface activation of Ba_{0.5}Sr_{0.5}Co_{0.8}Fe_{0.2}O_{3-δ} capillary membranes, *J. Memb. Sci.* 368 (2011) 223–232. doi:10.1016/j.memsci.2010.11.034.
- [19] P.L. Rachadel, D.F. Souza, E.H.M. Nunes, J.C.D. da Costa, W.L. Vasconcelos, D. Hotza, A novel route for manufacturing asymmetric BSCF-based perovskite structures by a combined tape and freeze casting method, *J. Eur. Ceram. Soc.* 37 (2017) 5249–5257. doi:10.1016/j.jeurceramsoc.2017.04.035.
- [20] M.M. Lorente-Ayza, M.J. Orts, V. Pérez-Herranz, S. Mestre, Role of starch characteristics in the properties of low-cost ceramic membranes, *J. Eur. Ceram. Soc.* 35 (2015) 2333–2341. doi:10.1016/j.jeurceramsoc.2015.02.026.
- [21] M.N. Islam, W. Araki, Y. Arai, Ferroelastic mechanical behavior of porous La_{0.6}Sr_{0.4}Co_{0.2}Fe_{0.8}O_{3-δ} prepared using corn starch as a pore former, *Int. J. Mech. Prod. Eng.* 6 (2018) 37–40.
- [22] H. Itoh, H. Asano, M. Nagata, H. Iwahara, Preparation of CaTiO₃ Porous Substrate by Foam-Burning Method, *J. Ceram. Soc. Japan.* 105 (1997) 1022–

1026.

- [23] E. Gregorová, Z. Živcová, W. Pabst, Porosity and pore space characteristics of starch-processed porous ceramics, *J. Mater. Sci.* 41 (2006) 6119–6122.
doi:10.1007/s10853-006-0475-z.
- [24] Z. He, K.B. Andersen, L. Keel, F.B. Nygaard, M. Menon, K.K. Hansen, Processing and characterization of porous electrochemical cells for flue gas purification, *Ionics (Kiel)*. 15 (2009) 427–431. doi:10.1007/s11581-008-0286-0.
- [25] R. Ahmad, M.S. Anwar, J. Kim, I.H. Song, S.Z. Abbas, S.A. Ali, F. Ali, J. Ahmad, H. Bin Awais, M. Mehmood, Porosity features and gas permeability analysis of bi-modal porous alumina and mullite for filtration applications, *Ceram. Int.* 42 (2016) 18711–18717. doi:10.1016/j.ceramint.2016.09.009.
- [26] P. Albano, L.B. Garrido, K. Plucknett, L.A. Genova, Processing of porous yttria-stabilized zirconia tapes : Influence of starch content and sintering temperature, *Ceram. Int.* 35 (2009) 1783–1791. doi:10.1016/j.ceramint.2008.10.003.
- [27] E. Gregorová, Z. Živcová, W. Pabst, Porous Ceramics Made Using Potato Starch as a Pore-forming Agent, *Fruit, Veg. Ceram. Sci. Biotechnol.* 3 (2009) 115–127.
- [28] L. Nie, J. Liu, Y. Zhang, M. Liu, Effects of pore formers on microstructure and performance of cathode membranes for solid oxide fuel cells, *J. Power Sources.* 196 (2011) 9975–9979. doi:10.1016/j.jpowsour.2011.08.036.
- [29] B. Qifu, D. Weixia, Z. Jianer, W. Yongqing, L. Yang, Effects of Pore Former on Properties of Alumina Porous Ceramic for Application in Micro-Filtration Membrane Supports, *Key Eng. Mater.* 655 (2015) 97–102.
doi:10.4028/www.scientific.net/KEM.655.97.
- [30] Y. Zhang, J. Zhu, H. Ren, Y. Bi, L. Zhang, Synthesis and properties of

- melamine–starch hybrid aerogels cross-linked with formaldehyde, *J. Sol-Gel Sci. Technol.* 83 (2017) 44–52. doi:10.1007/s10971-017-4375-2.
- [31] T.J. Schoch, Mechano-chemistry of Starch, *Mechano-Chemistry of Starch*. 14 (1967) 53–78.
- [32] T. Kuge, On the Physicochemical Properties of Starch, *Denpun Kagaku*. 39 (1992) 51–56.
- [33] T. Harada, A. Harada, Gel Formation and Ultrastructure in Food Polysaccharides, MARCEL DEKKER, 1998.
- [34] P. Taggart, Starch as an ingredient: manufacture and applications, in: A. - C ELIASSON (Ed.), *Starch Food*, Woodhead Publishing Limited, CRC Press LLC, 2004.
- [35] H.F. Zobel, S. M., Starch: Structure, Analysis, and Application, in: A.M. Stephen, G.O. Phillips, P.A. Williams (Eds.), *Food Polysaccharides Their Appl.*, Second Edi, Taylor & Francis, 2006: pp. 25–86.
- [36] E. Gregorová, W. Pabst, I. Boháček, Characterization of different starch types for their application in ceramic processing, *J. Eur. Ceram. Soc.* 26 (2006) 1301–1309. doi:10.1016/j.jeurceramsoc.2005.02.015.
- [37] Z. Nie, Y. Lin, Fabrication of porous alumina ceramics with corn starch in an easy and low-cost way, *Ceram. - Silikaty*. 50 (2015) 348–352. doi:10.1115/DETC2012-71473.
- [38] E. Gregorová, W. Pabst, Porosity and pore size control in starch consolidation casting of oxide ceramics-Achievements and problems, *J. Eur. Ceram. Soc.* 27 (2007) 669–672. doi:10.1016/j.jeurceramsoc.2006.04.048.
- [39] L.B. Garrido, M.P. Albano, L.A. Genova, K.P. Plucknett, Influence of starch type

- on characteristics of porous 3Y-ZrO₂ prepared from a direct consolidation casting method, *Mater. Res.* 14 (2011) 39–45. doi:10.1590/S1516-14392011005000016.
- [40] M.L. Sandoval, M.H. Talou, P.M. De Souto, R.H.G.A. Kiminami, M.A. Camerucci, Microwave sintering of cordierite precursor green bodies prepared by starch consolidation, *Ceram. Int.* 37 (2011) 1237–1243. doi:10.1016/j.ceramint.2010.11.041.
- [41] S. Li, C. Wang, J. Zhou, Effect of starch addition on microstructure and properties of highly porous alumina ceramics, *Ceram. Int.* 39 (2013) 8833–8839. doi:10.1016/j.ceramint.2013.04.072.
- [42] Z. Živcová, E. Gregorová, W. Pabst, Alumina ceramics prepared with new pore-forming agents, *Process. Appl. Ceram.* 2 (2008) 1–8. doi:10.2298/PAC0801001Z.
- [43] O. Lyckfeldt, J.M.F. Ferreira, Processing of porous ceramics by ‘starch consolidation,’ *J. Eur. Ceram. Soc.* 18 (1998) 131–140. doi:10.1016/S0955-2219(97)00101-5.

Chapter 5 | Development of novel materials for dual-phase membrane

Preface

Utilization of dual-phase membranes composed of ionic and electronic conducting phases would be another approach to further improve oxygen separation characteristics, because single component MIEC has insufficient oxide ion conductivity for practical application. In order to compensate for this, an oxide ion conductor has been added to the electron conductor and MIEC, and has been studied as a technique for improving the characteristics. CeO_2 is an oxide ion conductor and is frequently used in the ion conduction phase of a dual-phase membrane because it exhibits high electronic conductivity above 700 °C depending on conditions. Numerous oxygen separation properties have been reported for materials combining CeO_2 -based oxides with metals and Co-, Fe-, and Mn-based perovskite oxides as the electronic conduction phase. However, no dual-phase membrane materials have been reported yet that exceed the oxygen separation performance of existing single-phase MIECs. The reason is that the composite material does not exhibit the characteristics of each phase as expected because a by-product is generated at the interface by a reaction between different materials during the sintering process. In order to fundamentally solve such problems, it is necessary to control the defect structure of materials and understand the interface reaction mechanism in material development. In this chapter, an attempt has been made to develop an oxide ion conductor having low interfacial reactivity with different materials during the sintering process.

1. Introduction

The recent studies focusing on electrochemical devices, such as the solid oxide fuel cell (SOFC) and solid oxide electrolysis cell (SOEC), have been of increasing importance in modern society [1–10]. The SOFC can directly convert chemical energy, such as hydrogen, and hydrocarbon energy of a reaction into electric energy. The SOEC can store the electricity as hydrogen and hydrocarbon energy. The reversible system having both the SOFC/SOEC properties are especially attracting widespread attention [11–19]. The materials and fabrication technologies, which are used for SOFCs, are directly applicable to SOEC devices. During the past years, the question of lowering the operating temperature of the SOFCs has become a fundamental issue for improving materials compatibility, reducing energy consumption and startup time, and enhancing the durability and reliability over the long-term [9]. Considering that the material selection of the cell components and the stack design are mainly determined by the properties of the solid electrolyte, because the oxide ion conductivity strongly depends on the operating temperature. The electrolyte material selection is a crucial step in the development of suitable devices. In addition, this purpose is further complicated because the attention must also be focused on many other parameters such as gas-tightness, electronically non-conducting, chemical stability over a wide oxygen partial pressure and temperature range, good mechanical properties, chemical and thermal expansion compatibility with electrodes and other components [9,20,21].

In the literature, many studies can be found about the improvement of the ionic conductivity for the different ceramic-based oxide electrolyte materials, such as zirconia, ceria, lanthanum gallate and bismuth-based oxides. Zirconia-based electrolytes, such as

yttria-stabilized zirconia (YSZ), are the most popular materials employed as the electrolyte in SOFCs, because of their attractive ionic conductivity, stability in both oxidizing and reducing environments, and compatibility with the electrode materials. However, the ionic conductivity of YSZ at low and intermediate temperatures (450–800 °C) is much lower than that of ceria-based electrolytes such as gadolinium-doped ceria (GDC) or lanthanum gallate-based electrolytes such as $\text{La}_{0.8}\text{Sr}_{0.2}\text{Ga}_{0.8}\text{Mg}_{0.2}\text{O}_{3-\delta}$ (LSGM8282). $\text{La}_{1-x}\text{Sr}_x\text{Ga}_{1-y}\text{Mg}_y\text{O}_{3-\delta}$ (LSGM), in which Sr is replaced with the La site and Mg with the Ga site, is one of the most interesting systems [22–26]. Both dopants generate oxygen vacancies to compensate their lower valences. However, one of the problems is the high chemical reactivity of LSGM at the temperatures required for cell manufacturing, which makes the preparation of the LSGM-based IT-SOFCs difficult. Generally, the densification of LSGM to a gas impermeable level requires a very high sintering temperature (around 1400–1500 °C) [21,27–29]. The advantage of the LSGM electrolyte is its compatibility with the Mn- and Co-based perovskite-type cathode materials [30–36]. It has been reported that a small amount of Co doping in the LSGM structure is not detrimental to its oxide ion-conduction properties and thus enables a lower temperature operation [37].

However, the incompatibility with the other electrode materials, such as the Ni- and Zr- based anode materials, is well known to form the insulating $\text{La}_2\text{Zr}_2\text{O}_7$ pyrochlore and SrZrO_3 perovskite phases [38–40]. Furthermore, it creates thermal stress at the interface between the electrode and electrolyte due to the big difference in the thermal expansion coefficient. Cermet anodes, such as Ni- and Ce- based materials, which are usually selected for the LSGM electrolyte, can react with LSGM during sintering at high temperatures; La^{3+} ions diffuse into the anode through the electrolyte–anode interface,

resulting in the formation of LaNiO_3 at the interface, and highly-resistive $\text{LaSrGa}_3\text{O}_7$ phases in the electrolyte bulk [21].

Many authors have reported that ceria-based interlayers can suppress the reaction between the LSGM and the electrodes during the sintering process [21,41–48]. Kim et al. reported that GDC could significantly relax the interfacial reactions between the LSGM electrolyte and Ni-GDC anode even through the partially formed $\text{LaSrGa}_3\text{O}_7$ phase [45,46]. The Cation non-stoichiometry has been recognized to have a significant influence on the properties of the perovskite-type oxides. The A-site cation deficiency in the perovskite systems is a widely adopted strategy for endeavoring to engineer the defect chemistry, which affects the physicochemical properties of the perovskite oxides [35,49–61]. Some A-site deficient perovskites exhibit a high thermal stability and chemical compatibility while maintaining good electrochemical characteristics. For example, the introduction of a La deficiency in the Sr-doped LaMnO_3 (LSM) electrode suppresses the formation of the $\text{La}_2\text{Zr}_2\text{O}_7$ pyrochlore phase at the interface with the YSZ electrolyte at temperatures higher than 1000 °C [49,54]. A similar effect of the suppression of the high temperature reactivity of an A-site deficient perovskite has been reported for the La-deficient $\text{La}_{1-x}\text{CoO}_{3-\delta}$ with alumina [55]. Based on these results, the high temperature reactivity between the perovskite LSGM8282 electrolyte and ceria-based interlayer material could also be suppressed by introducing an A-site deficiency in the LSGM. In our previous study, LSGM powders with various A-site deficiencies were synthesized, and their reactivity to $\text{Ce}_{0.9}\text{Gd}_{0.1}\text{O}_{3-\delta}$ was compared. The reaction-suppressed effect is much more remarkable by keeping the oxygen amount the same as LSGM8282 (oxygen amount= 2.8). The best composition was $\text{La}_{0.9}\text{Sr}_{0.05}\text{Ga}_{0.8}\text{Mg}_{0.2}\text{O}_{2.8}$ (A-site = 0.95, O = 2.8) [50]. However, the conductivity of the $\text{LaSrGa}_3\text{O}_7$ phase, which is

inevitably formed at the interface, has not been considered; it decreases by increasing the substitution amount of Sr to the La site [62].

In this study, to further investigate the interfacial reaction between the LSGM and GDC electrolytes, we focused on the Sr doping dependence on the La^{3+} diffusion from LSGM, which results in the forming of the $\text{LaSrGa}_3\text{O}_7$ phase from LSGM. The screening of the most stable LSGM was performed using the thermally-treated LSGM powders mixed with GDC by X-ray diffraction (XRD). The reactivity of the selected LSGM with GDC was further investigated by energy dispersive X-ray spectroscopy (EDS) and electric conductivity measurements.

2. Experimental procedure

2.1. Preparation and characterization of Sr-ion deficient LSGM8282

LSGM powders were prepared by a conventional solid state reaction method. Reagent grade chemicals of La_2O_3 , SrCO_3 , Ga_2O_3 , and MgO (99.9% purity, Kojundo Chemical Lab. Co., Ltd.) were weighed for a series of LSGMs: $\text{La}_{0.8}\text{Sr}_{0.2-x}\text{Ga}_{0.8}\text{Mg}_{0.2}\text{O}_{2.8-\delta}$ (LSGM8282, $x=0.00, 0.05, 0.10, 0.15, 0.20$). The La_2O_3 powder was pre-calcined at 1000 °C for 2h prior to the weighing in order to remove the hydroxide impurities. The weighed powders were mixed in an agate mortar with a small amount of ethanol. The powder mixtures were compacted at 50MPa, calcined at 1250 °C for 5h, then reground. The ground powders were recompacted at 50MPa, thermally treated at 1400 °C for 10h, and reground.

GDC used in this study was a commercially-available powder (Anan Kasei Co., Ltd., CGO90/10 ULSA, $D=0.3\mu\text{m}$). The phase purity of the final products was examined by a powder XRD analysis (Bruker AXS, D8 ADVANCE). The diffraction patterns were

collected at room temperature over the range of $2\theta = 20-80^\circ$ using Cu K α radiation. Electric conductivity measurements were performed for the sintered specimens. The as-synthesized LSGMs were characterized by the electric conductivity measurements using the sintered specimens. The as-synthesized powders were pressed into cuboid bars (5mm \times 15mm \times 4-5mm in length) and sintered at 1400 °C for 2h. The electric conductivity of the sintered bar samples was measured by the DC four-terminal method in air. Commercial silver paste (DuPont, 4922N) and Pt wire were used for the electrode and conducting wire, respectively. The measurement was performed in the temperature range from 800 to 400 °C during cooling.

2.2. Reactivity tests between LSGM and GDC

Comparison of the reactivity of the various LSGMs and GDC was performed by three methods: i.e., XRD analysis, SEM-EDS analysis and electric conductivity measurements. The LSGM and GDC powders were mixed in the weight ratio of 1:1 using an agate mortar. The powder mixtures were lightly compacted, thermally treated in air at 1400 °C for 2h, then ground. The temperature of 1400 °C was selected for sintering since it is the maximum temperature required for the co-firing temperature of the LSGM and GDC. The phase composition of the ground powders was characterized by a powder XRD analysis.

The LSGM and GDC were separately dispersed in ethanol with a dispersing agent to prepare their stable suspensions. Bi-layers of the LSGM/GDC were prepared by the sequential electrophoretic deposition (EPD) method on a palladium substrate. After drying at room temperature in air, the deposit was separated from the substrate, then

sintered at 1400 °C for 2h. Cross-sectional microstructure observations and EDS line mappings at the interface of the LSGM/GDC layers were performed by an field emission scanning electron microscope (FE-SEM) equipped with an energy dispersive X-ray spectrometry (EDS) analyzer (JEOL, JSM-6500F). The LSGM and GDC powders were mixed in the weight ratio of 1:1 using an agate mortar. The powder mixtures were pressed into cuboid bars (5mm×15mm×4-5mm in length) and sintered at 1400 °C for 2h. The electric conductivity of the sintered bar samples was measured by the DC four-terminal method in air.

3. Results and discussion

3.1. XRD examination and microstructural observation

Figure 5-1 shows the XRD patterns of the prepared LSGM8282 powders. All the XRD patterns were mainly assigned as the perovskite phase with small peaks from LaSrGaO_4 and $\text{LaSrGa}_3\text{O}_7$. Though slight impurity phase peaks are observed, their main peaks were very similar to each other. The slight peak shift to a higher diffraction angle and the peak split due to the lattice shrinkage and distortion of the perovskite structure were observed for the $x=0.1, 0.15, 0.2$ specimens. This suggests that the cubic phase of LSGM8282 changes to the asymmetric phase such as the orthorhombic phase. Figure 5-2 shows the unit cell volume calculated from the lattice constants of the LSGMs evaluated from the XRD measurements. The unit cell volume decreased with the increasing amount of the A-site Sr-ion deficiency followed by the lattice shrinkage.

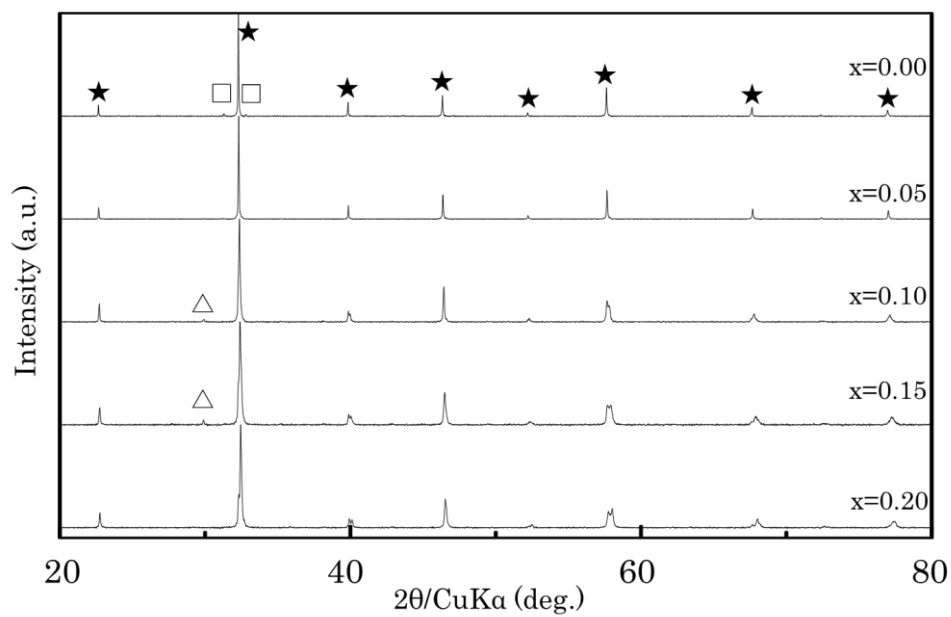


Fig. 5-1 XRD patterns of $\text{La}_{0.8}\text{Sr}_{0.2-x}\text{Ga}_{0.8}\text{Mg}_{0.2}\text{O}_{2.8-\delta}$ ($x=0.00, 0.05, 0.10, 0.15, 0.20$). Secondary phase are indicated by the symbol ★ for LSGM, △ for LaSrGaO_4 , □ for $\text{LaSrGa}_3\text{O}_7$.

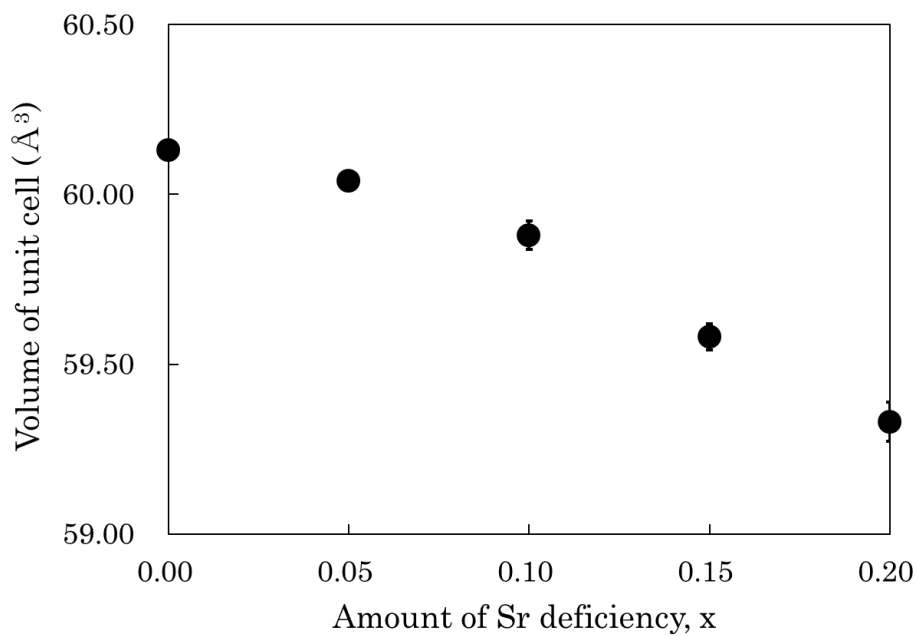


Fig. 5-2 Unit cell volume of $\text{La}_{0.8}\text{Sr}_{0.2-x}\text{Ga}_{0.8}\text{Mg}_{0.2}\text{O}_{2.8-\delta}$ ($x=0.00, 0.05, 0.10, 0.15, 0.20$).

3.2. Electric properties

Figure 5-3 shows the total conductivity and the activation energy of the LSGM8282 with different Sr-ion deficiencies. The total conductivity at $x=0.00$ was almost unchanged from that at $x=0.05$. The conductivity gradually decreased with the increasing deficiencies at $x=0.10\sim 0.20$. The activation energy changed at around 600 °C. It has reported that the change in the activation energy around 600 °C in the LSGM-based oxide is due to the change in the association state of the oxygen vacancies [22]. Generally, it is considered that an increase in the amount of the Sr-ion deficiency changes the amount of oxygen vacancies and contributes to improvement of the oxide ion conductivity. However, it seems that the influence of the inhibition of diffusion of oxide ions by the influence of the structure distortion is superior. Therefore, the electric conductivity decreased. The reason could be explained by the dopant-vacancy interaction mechanisms, e.g., $V_{La}''' - V_O''$, forming a trap (or associate), to the oxide-ion vacancies migration and thus reducing the total conductivity [63,64]. Another possible mechanism is the formation of a Ga, Mg-enriched second phase at the intragrain and grain-boundaries [65,66]. However, strong peaks attributed to the second phase are not observed in the XRD pattern shown in Figure 5-1, therefore, the influence of the latter is considered to be low.

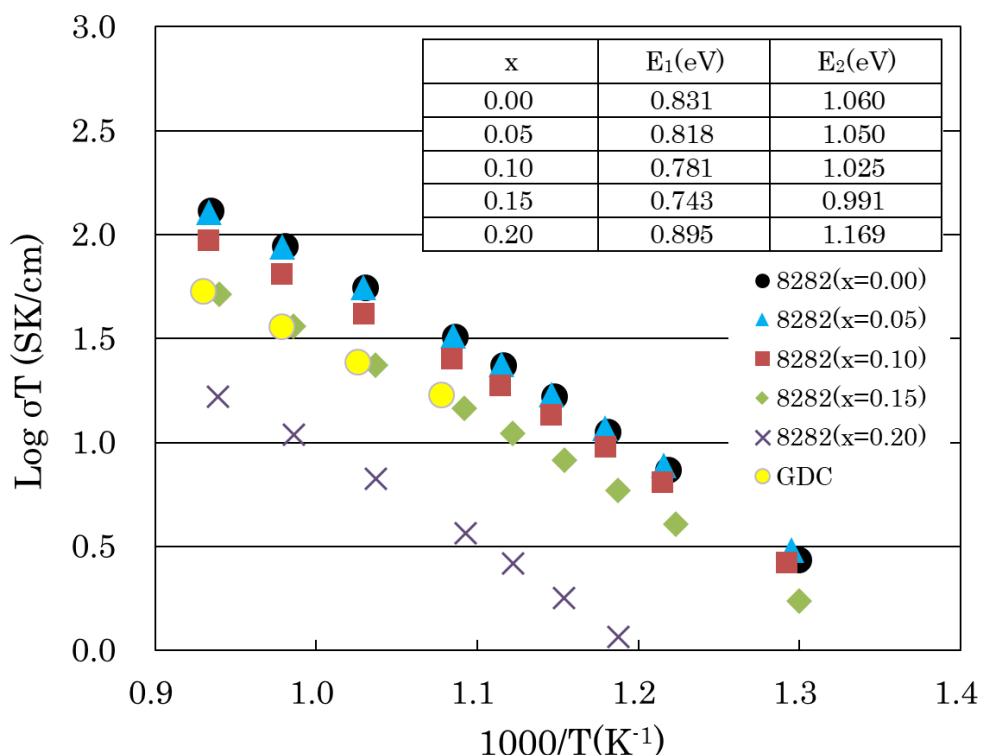


Fig. 5-3 Arrhenius plots of the electric conductivity of $\text{La}_{0.8}\text{Sr}_{0.2-x}\text{Ga}_{0.8}\text{Mg}_{0.2}\text{O}_{2.8-x}$ ($x=0.00, 0.05, 0.10, 0.15, 0.20$) and the evaluated activation energies at 600-800 °C (E_1) and 400-600 °C (E_2).

3.3. Interaction between LSGM and GDC

Figure 5-4 shows the XRD pattern change of the mixed powder of LSGM and GDC by the heat treatment at 1400 °C for 2 hours in air. The black and red lines show the spectra before and after the heat treatment, respectively. The peak positions of the stoichiometric ($x = 0.00$) LSGM 8282 and GDC powders before the heat treatment are also indicated by the dotted lines. The peaks of LSGM and GDC shifted after the thermal treatment, suggesting the mutual diffusion of cations at the interface between the LSGM and GDC. The peaks of LSGM shifted to higher diffraction angles, suggesting the occurrence of lattice shrinkage. On the other hand, the peaks of GDC shifted to lower diffraction angles,

suggesting lattice expansion. The peak shifts of the LSGM are probably due to the diffusion of the A-site-located La^{3+} and Sr^{2+} ions from the LSGM to GDC [41,46,50]. The peak shifts of the GDC are probably due to the diffusion of the Ce^{4+} and Gd^{3+} ions from the GDC to LSGM. The LSGM 110 and GDC 200 diffraction peaks near $2\theta = 32.5^\circ$ shifted less by the increasing Sr deficiency due to the difference in the ionic radius ($\text{Sr}^{2+} > \text{La}^{3+} > \text{Ce}^{4+}, \text{Gd}^{3+}$). This means that the A-site cation diffusion of the A-site deficient LSGM is less likely to occur than that of the stoichiometric ($x=0.00$) LSGM. This result suggests that the stability of the LSGM phase at high temperatures can be improved by making the A-site-located Sr ions partially insufficient; the effect is especially prominent at $x=0.15$. However, the mutual diffusion of the cation between the LSGM and the GDC is still implied from the GDC peaks shifts.

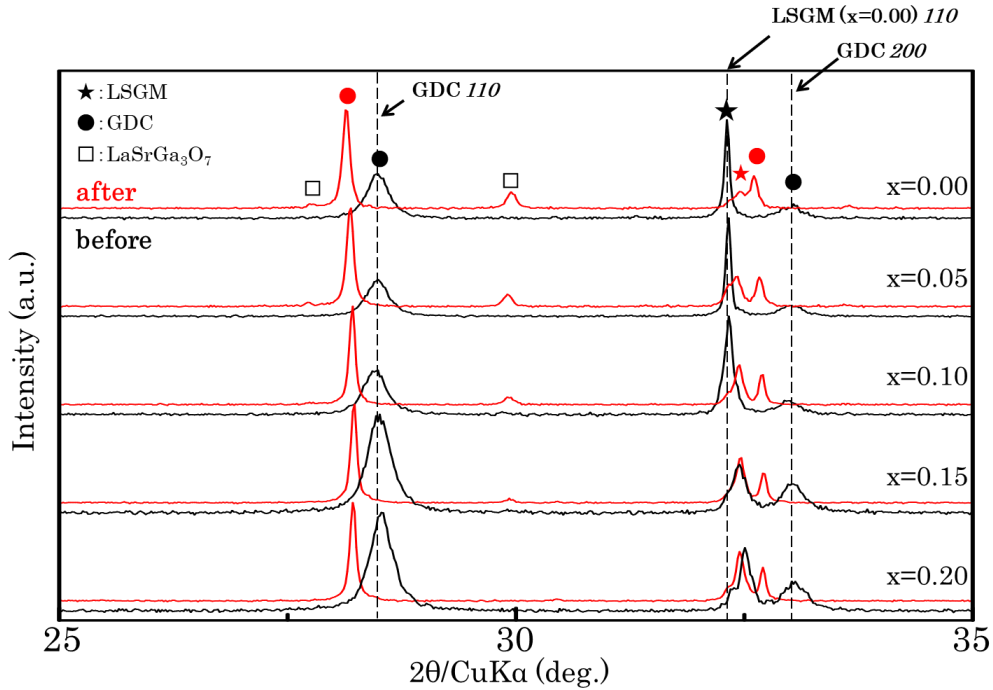


Fig. 5-4. Comparison of the XRD patterns of the mixed powders of the LSGM and GDC after the thermal treatment at 1400 °C in the air. The black line denotes the state before the thermal treatment. The red line indicates the reacted LSGM and GDC.

Figure 5-5 shows the relation between the thermal treatment temperature and the cell volume of the various the Sr-ion deficient LSGMs. The cell volume of the $x=0.00-0.10$ samples decreased after the thermal treatment at the higher temperatures, however, this change is not notable for the $x=0.15-0.20$ samples. The cell volume of the stoichiometric ($x=0.00$) LSGM significantly decreased after the thermal treatment. The effect of the reactivity suppression of the LSGM with GDC by the Sr-ion deficiency is also confirmed from the formation of the reacted $\text{LaSrGa}_3\text{O}_7$ phase.

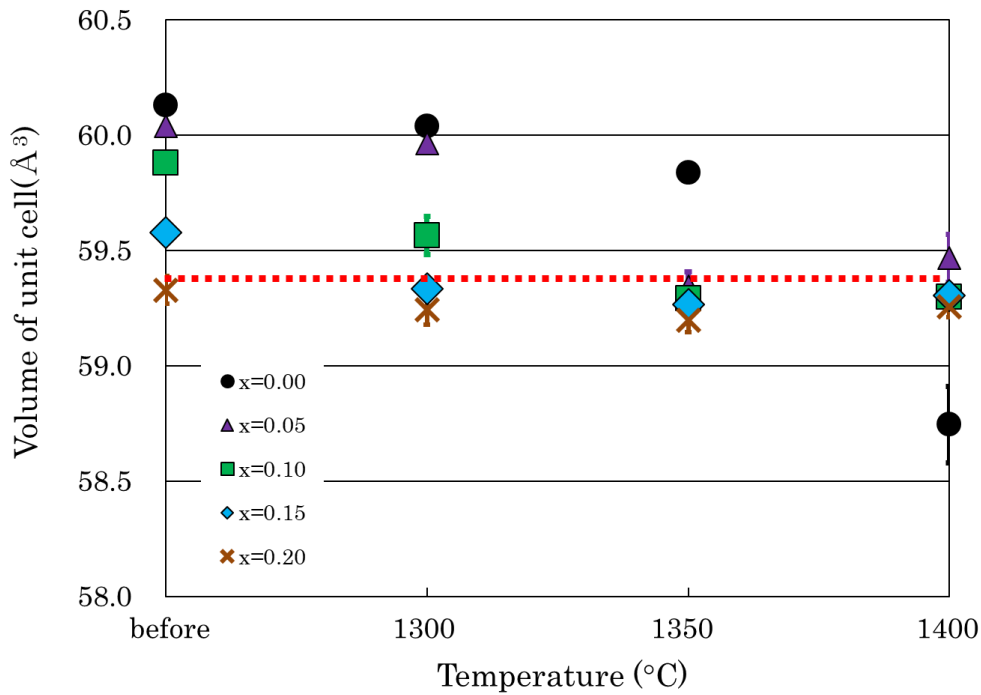


Fig. 5-5 The relation between the amount of the temperature of thermal treatment and the cell volume of Sr-site deficiency prepared LSGMs.

The ratio of the relative intensities of the $\text{LaSrGa}_3\text{O}_7$ 211 diffraction peak and the LSGM 110 diffraction peak is shown in Fig. 5-6 as a function of the amount of the Sr-ion deficiency. It is difficult to identify what phase is formed only by interface line analysis.

So, in this study, the contact area of LSGM and GDC phase was increased by mixing those powders. As a result, the amount of phases formed at the interface by heat treatment was sufficient for identification by XRD. The $\text{LaSrGa}_3\text{O}_7$ is known as a high resistivity phase of which its formation should be suppressed. The most reaction-suppressed powder was at $x=0.20$, however, the LSGM of $x=0.20$ is not suitable for use as an electrolyte due to its very low electric conductivity as shown in Fig. 5-3. Based on these results, it is considered that $x=0.15$ is the optimal among all the samples.

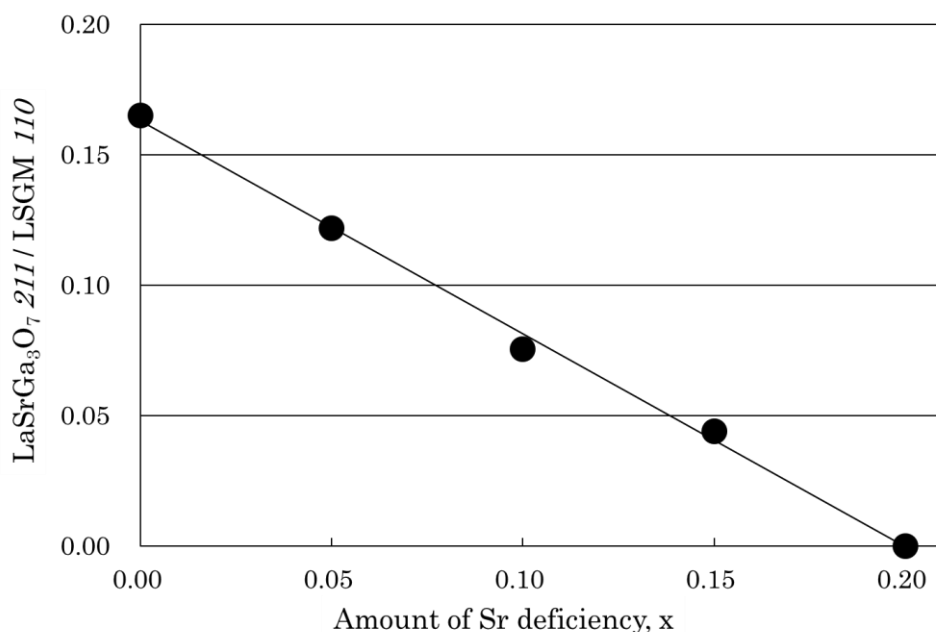


Fig. 5-6 The relative intensity of the $\text{LaSrGa}_3\text{O}_7$ 211 peak compared to the LSGM 110 peak calculated for all the LSGM–GDC mixtures as a function of the amount of A-site deficiency.

Figure 5-7 shows the SEM images and the EDS elemental profiling of La, Sr, Ga, Mg, Ce and Gd around the interfaces of the LSGM/GDC after the thermal treatment at 1400 °C. The LSGM is on the left and GDC is on the right of the SEM images. As shown

in [Figure 5-7](#), the La and Sr ions exist on the GDC side, and the Ce and Gd ions exist on the LSGM side, indicating the mutual diffusion of the cations at the interface. The elemental ratio at the interface "spot A" of LSGM ($x = 0.00$) and GDC analyzed by EDX is shown in [Table 5-1](#). The ratio of (La and Sr) and the Ga was close to 2:3. The thickness of the reacted layer of $x=0.15$ is smaller than that of $x=0.00$, the thicknesses for the LSGM($x=0.00$)/GDC interface and LSGM($x=0.15$)/GDC interface are about 7 μm and 3 μm , respectively.

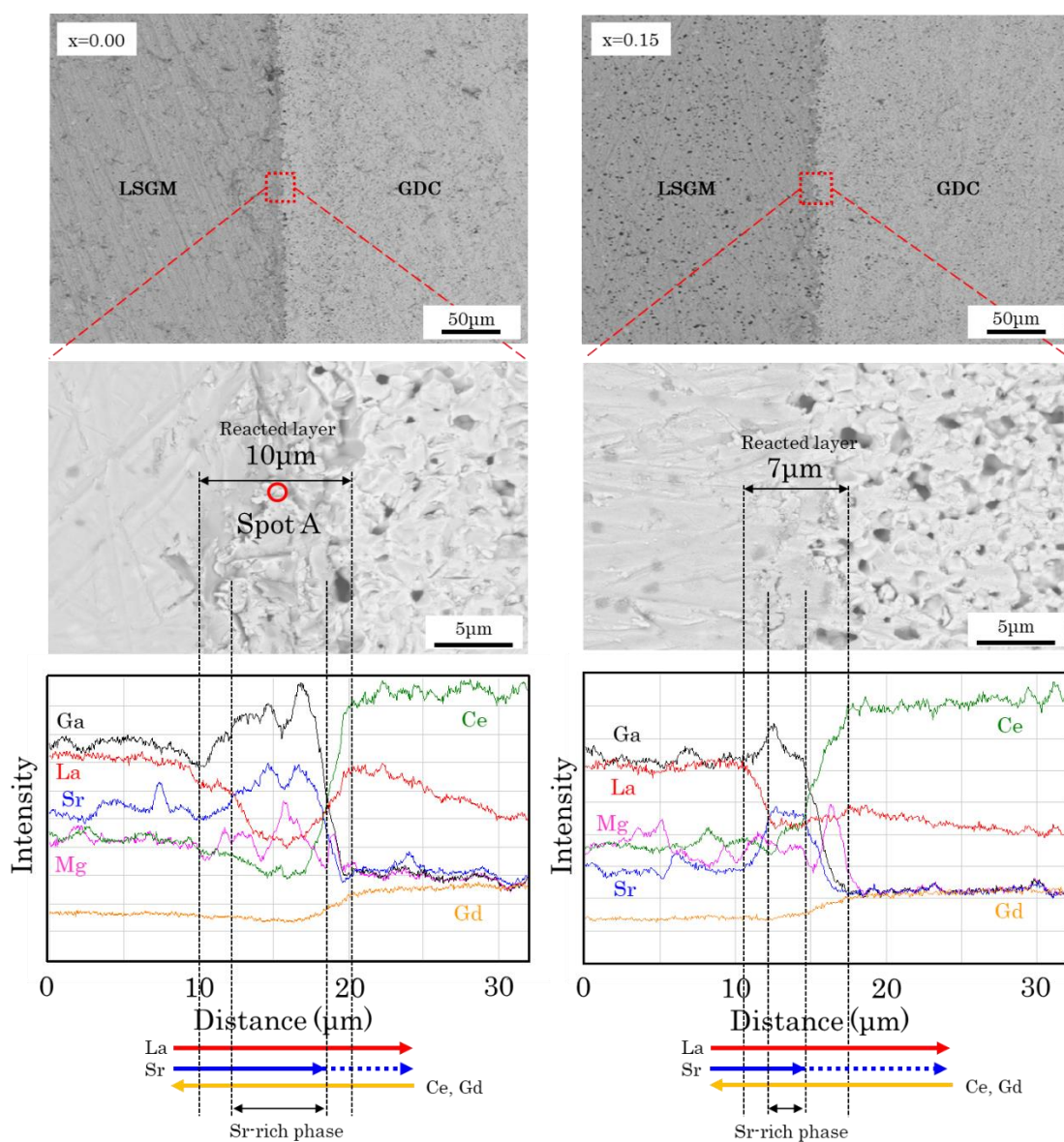


Fig. 5-7 SEM image and EDS elemental profiling of La, Sr, Ga, Mg, Ce and Gd near the interface of the LSGM/GDC after the thermal treatment at 1400 °C. The LSGM is on the left and GDC is on the right of the SEM image. (Left side: $x=0.00$, light side: $x=0.15$)

Table 5-1 EDX analysis of the reacted layer at the spot A of the LSGM ($x= 0.00$)

| Spot | La | Sr | Ga | Mg | Ce | Gd |
|------|------|------|------|------|------|------|
| A | 1.14 | 0.59 | 3.82 | 0.29 | 0.45 | 0.08 |

Figure 5-8 show the electric conductivity of the LSGM and GDC mixture compacts after the thermal treatment at 1400 °C. The A site-deficient LSGM of $x = 0.05$ to 0.20 showed almost the same conductivity after the heat treatment, and its value was higher than in the case of stoichiometric ($x = 0.00$) LSGM. This suggests that the formation of the highly resistive phase in the Sr-ion deficient LSGM is suppressed.

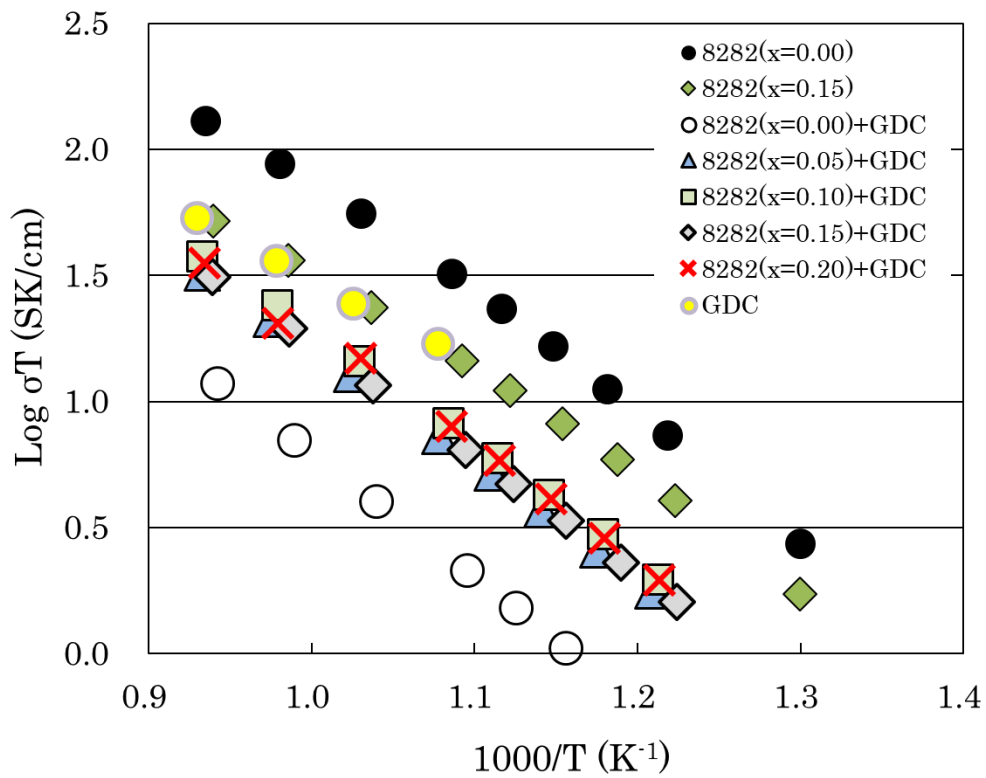
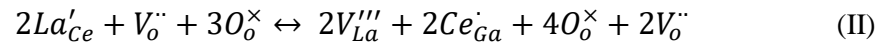
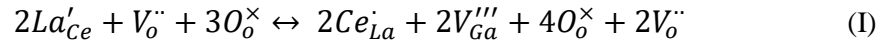


Fig.5-8 Arrhenius plots of the electric conductivity of $\text{La}_{0.8}\text{Sr}_{0.2-x}\text{Ga}_{0.8}\text{Mg}_{0.2}\text{O}_{2.8-\delta}$ ($x=0.00, 0.05, 0.10, 0.15, 0.20$) after thermal treatment with GDC.

Comparing the Shannon ion radii La^{3+} (1.36 Å), Sr^{2+} (1.44 Å), Ga^{3+} (0.62 Å), O^{2-} (1.40 Å) in the perovskite structure with the ion radii Ce^{4+} (0.97 Å), Gd^{3+} (1.053 Å), O^{2-} (1.42 Å) in the fluorite structure, the size of the La^{3+} is considerably larger than that of the Ce^{4+} . However, the diffusion of La ions in the interface reaction of LSGM / electrode has been reported in many papers, and it is probable that La ions substitutionally dissolve in Ce sites.

Considering only the base materials LaGaO_3 and CeO_2 , mutual substitution of the cations at the $\text{LaGaO}_3/\text{CeO}_2$ interface can be expressed as the following two equations using the Kröger-Vink notation:



The Ce ion has a larger ion radius than the Ga ion, and in order to substitute the Ce ion for the Ga ion located at the center of the oxygen octahedron, the O-O bond must be heavily distorted. On the other hand, since the ion radius of the La ion is larger than that of the Ga ion, it is considered that the Ce ion is more likely to substitutionally dissolve in the La site than in the Ga site. Therefore, the mutual substitution at the $\text{LaGaO}_3/\text{CeO}_2$ interface would occur according to the reaction (I) rather than the reaction (II).

The reaction layer can be classified as the I-V layers: Layer I: $(\text{La}_{0.8}\text{Sr}_{0.2-x})_{1-y}(\text{Ga}_{0.8}\text{Mg}_{0.2})\text{O}_{2.8-6}$, Layer II: $(\text{La}_{0.8}\text{Sr}_{0.2-x}\text{Ce}_a\text{Gd}_b)\text{Ga}_{0.8}\text{Mg}_{0.2}\text{O}_{2.8-6}$, Layer III: $[(\text{La}_{1+x}\text{Sr}_{1-x})_{1-a-b}\text{Ce}_a\text{Gd}_b]\text{Ga}_3\text{O}_{7-6}$, Layer IV: $\text{Ce}_{0.9-x}(\text{Gd}_{0.1-y}\text{La}_a\text{Sr}_b)\text{O}_{1.95-6}$, Layer V: $\text{Ce}_{0.9}(\text{Gd}_{0.1}\text{La}_a\text{Sr}_b)\text{O}_{1.95-6}$. The reacted layer I-V between LSGM and GDC are schematically shown in [Figure 5-9](#).

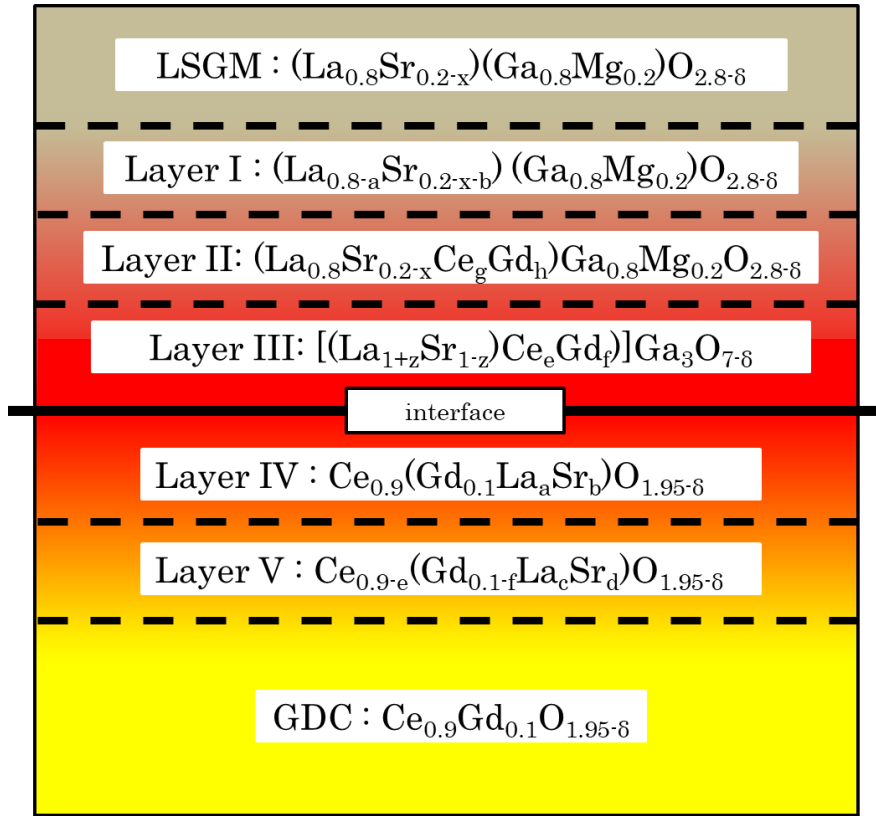
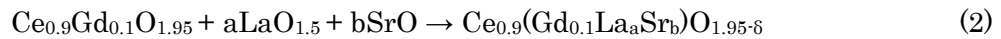
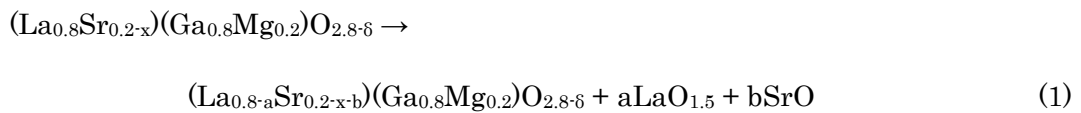
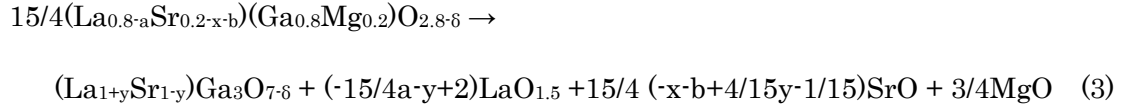


Fig. 5-9 Reacted layer I-V in LSGM/GDC interface

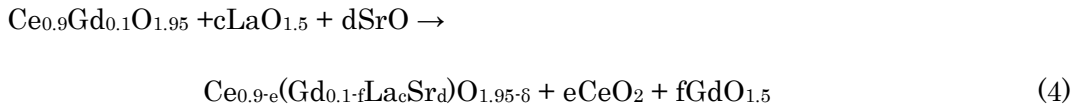
The formation of the above-mentioned reaction layers between the LSGM and GDC could be explained as follows: The first step of the LSGM/GDC interaction is triggered by the diffusion of the La and Sr ions in the LSGM, The amount of the A-site ion deficiency of the LSGM increases by diffusion of the La ion and Sr ion; that is, ABO_3 to $A_{1-x}BO_{3-\delta}$ is expressed by [Reaction \(1\)](#). The La and Sr ions are dissolved in the GDC by [Reaction \(2\)](#).



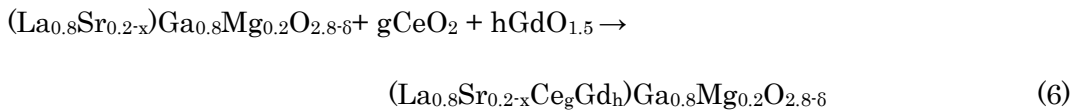
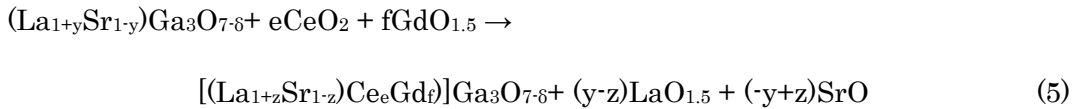
In the second step, the LSGM further becomes an A-site deficient composition, such as $A_2B_3O_7$, resulting in the formation of the highly resistive $(La,Sr)_2Ga_3O_7$ phase according [Reaction \(3\)](#).



In the third step, when the solution of the La and Sr ions in the GDC reaches the limit, the diffusion of the Ce and Gd ions in the GDC to LSGM occurs according to the [Reaction \(4\)](#).



In the fourth step, the Ce and Gd ions diffuse into the A-site of the LSGM via the 237 phase according to [Reactions \(5\) and \(6\)](#) [67,68].



Otherwise, the Ce ion may preferentially substitute for the B site ions of LSGM and produce $LaCeO_3$ and/or $SrCeO_3$.

In order to verify the validity of the reaction mechanism, the single phases of

$(\text{La}_{0.8}\text{Sr}_{0.1}\text{Ce}_{0.1})\text{Ga}_{0.8}\text{Mg}_{0.2}\text{O}_{2.8-\delta}$ (LCSGM) and $(\text{La}_{0.8}\text{Sr}_{0.1}\text{Gd}_{0.1})\text{Ga}_{0.8}\text{Mg}_{0.2}\text{O}_{2.8-\delta}$ (LGSGM), whose compositions correspond to that of layer II, were prepared by the same preparation method of the LSGM and their electric conductivities were then evaluated. Figure 5-10 shows the measured electric conductivities of LCSGM and LGSGM of which compositions are correspond to the layer II phase (so called 113 phase). The reported electric conductivities of $(\text{La}_{1+x}\text{Sr}_{1-x})\text{Ga}_3\text{O}_{7-\delta}$ [62] of which the compositions correspond to the layer III phase (the so-called 237 phase) are also shown in Fig. 5-10. The electric conductivity of the 237 phase ($x = 0.15\text{-}0.60$) shows a lower value as the Sr content increases.

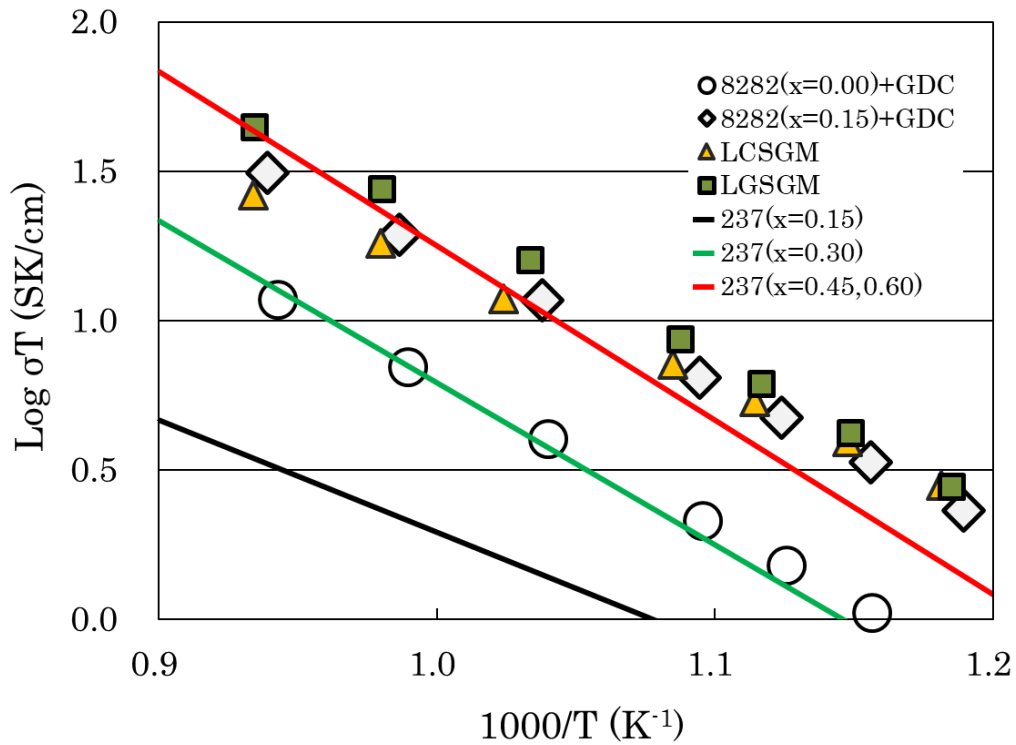


Fig. 5-10. Arrhenius plots of the electric conductivities of the LCSGM, LGSGM sintered compacts. The reported electric conductivities of $(\text{La}_{1+x}\text{Sr}_{1-x})\text{Ga}_3\text{O}_{7-\delta}$ are also shown in solid lines in the figure [62].

The conductivity after the reaction shows values similar to the 237 phase ($x = 0.30$) in the case of the stoichiometric LSGM and the activation energy is similar, thus the electric conductivity of the 237 phase will be dominant. On the other hand, for the A-site ion deficient LSGM sample, the electric conductivity after the reaction showed a value similar to the Sr-poor 237 phase ($x = 0.45, 0.60$). It is probable that generation of the low conducting Sr-rich 237 phase is suppressed even though the 237 phase is formed. On the other hand, the conductivities of the 113 phases also show values similar to those of the Sr-ion deficient LSGM samples after the reaction. Based on these results, it is considered that in the LSGM in which the A site ion is deficient, the influence of the layer II and layer III is dominant regarding the electric conductivity at the reaction interface with the GDC.

In previous studies, it has been reported that the solid solution of La and Sr rather enhances the electric conductivity of GDC [69]. In this study, we focus on the formation of the high-resistance phase and its suppression, therefore we do not make a deep discussion on the rather improved conductivity of GDC.

4. Conclusions

A series of Sr-ion deficient LSGMs ($\text{La}_{0.8}\text{Sr}_{0.2-x}\text{Ga}_{0.8}\text{Mg}_{0.2}\text{O}_{2.8-\delta}$ (LSGM8282, $x=0.00, 0.05, 0.10, 0.15, 0.20$)) exhibited a decrease in the unit cell volume with the increasing amount of the A-site Sr-ion deficiency. The electric conductivity of all the samples gradually decreased with an increase in the Sr-ion deficiencies by the influence of the structure distortion and the dopant-vacancy interaction. The Sr-ion deficient LSGMs showed less reactivity at the high temperatures than the stoichiometric ($x=0.00$) LSGM

against the GDC interlayer material. The reaction layer formed at the interface of the LSGM and GDC during the sintering process due to the mutual diffusion of the cations can be classified by the I-V layers: Layer I: $(\text{La}_{0.8}\text{Sr}_{0.2-x})_{1-y}(\text{Ga}_{0.8}\text{Mg}_{0.2})\text{O}_{2.8-\delta}$, Layer II: $(\text{La}_{0.8}\text{Sr}_{0.2-x}\text{Ce}_a\text{Gd}_b)\text{Ga}_{0.8}\text{Mg}_{0.2}\text{O}_{2.8-\delta}$ (so called 113 phase), Layer III: $[(\text{La}_{1+x}\text{Sr}_{1-x})_{1-a-b}\text{Ce}_a\text{Gd}_b]\text{Ga}_3\text{O}_{7-\delta}$ (so called 237 phase), Layer IV: $\text{Ce}_{0.9-x}(\text{Gd}_{0.1-y}\text{La}_a\text{Sr}_b)\text{O}_{1.95-\delta}$ and Layer V: $\text{Ce}_{0.9}(\text{Gd}_{0.1}\text{La}_a\text{Sr}_b)\text{O}_{1.95-\delta}$. It was considered that layers II and III were dominant as the reacted layers, however the generation of the low conducting Sr-rich 237 phase was suppressed even though the 237 phase was formed by introducing a Sr-ion deficiency to LSGM. It was suggested that the Sr-ion deficient LSGM $(\text{La}_{0.8}\text{Sr}_{0.2-x}\text{Ga}_{0.8}\text{Mg}_{0.2}\text{O}_{2.8-\delta})$ of $x=0.15$ was the best composition for suppressing the reaction with the GDC interlayer while retaining a relatively good electric conductivity.

References

- [1] F. Ramadhani, M.A. Hussain, H. Mokhlis, S. Hajimolana, Optimization strategies for Solid Oxide Fuel Cell (SOFC) application: A literature survey, *Renew. Sustain. Energy Rev.* 76 (2017) 460–484.
<https://doi.org/10.1016/j.rser.2017.03.052>.
- [2] R. Bove, S. Ubertini, eds., *Modelling Solid Oxide Fuel Cells*, Springer US, 2008.
- [3] N. Brandon, D. Thompsett, eds., *Fuel Cells Compendium*, Elsevier Ltd, 2005.
<https://doi.org/10.1016/j.ssi.2004.06.015>.
- [4] S.C. Singhal, K. Kendall, eds., *High Temperature Solid Oxide Fuel Cells : Fundamentals , Design and Applications*, Elsevier, n.d.
- [5] A.B. Stambouli, E. Traversa, Solid oxide fuel cells (SOFCs): A review of an environmentally clean and efficient source of energy, *Renew. Sustain. Energy Rev.* 6 (2002) 433–455. [https://doi.org/10.1016/S1364-0321\(02\)00014-X](https://doi.org/10.1016/S1364-0321(02)00014-X).
- [6] M.A. Laguna-Bercero, Recent advances in high temperature electrolysis using solid oxide fuel cells: A review, *J. Power Sources.* 203 (2012) 4–16.
<https://doi.org/10.1016/j.jpowsour.2011.12.019>.
- [7] L. van Biert, M. Godjevac, K. Visser, P. V. Aravind, A review of fuel cell systems for maritime applications, *J. Power Sources.* 327 (2016) 345–364.
<https://doi.org/10.1016/j.jpowsour.2016.07.007>.
- [8] S.P.S. Badwal, K. Foger, Solid Oxide Electrolyte Fuel Cell Review, *Ceram. Int.* 22 (1996) 257–265. [https://doi.org/10.1016/0272-8842\(95\)00101-8](https://doi.org/10.1016/0272-8842(95)00101-8).
- [9] N. Mahato, A. Banerjee, A. Gupta, S. Omar, K. Balani, Progress in material selection for solid oxide fuel cell technology: A review, *Prog. Mater. Sci.* 72 (2015)

- 141–337. <https://doi.org/10.1016/j.pmatsci.2015.01.001>.
- [10] N.Q. Minh, Ceramic Fuel Cells, *J. Am. Ceram. Soc.* 76 (1993) 563–88.
- [11] A. Tarancón, Strategies for lowering solid oxide fuel cells operating temperature, *Energies*. 2 (2009) 1130–1150. <https://doi.org/10.3390/en20401130>.
- [12] S. Elangovan, J.J. Hartvigsen, L.J. Frost, Intermediate temperature reversible fuel cells, *Int. J. Appl. Ceram. Technol.* 4 (2007) 109–118.
<https://doi.org/10.1111/j.1744-7402.2007.02132.x>.
- [13] D. Ferrero, A. Lanzini, P. Leone, M. Santarelli, Reversible operation of solid oxide cells under electrolysis and fuel cell modes: Experimental study and model validation, *Chem. Eng. J.* 274 (2015) 143–155.
<https://doi.org/10.1016/j.cej.2015.03.096>.
- [14] N.Q. Minh, M.B. Mogensen, Reversible Solid Oxide Fuel Cell Technology for Green Fuel and Power Production, *Electrochem. Soc. Interfacel Soc. Interface*. (2013) 55–62.
- [15] C.H. Wendel, Z. Gao, S.A. Barnett, R.J. Braun, Modeling and experimental performance of an intermediate temperature reversible solid oxide cell for high-efficiency, distributed-scale electrical energy storage, *J. Power Sources*. 283 (2015) 329–342. <https://doi.org/10.1016/j.jpowsour.2015.02.113>.
- [16] V. Menon, Q. Fu, V.M. Janardhanan, O. Deutschmann, A model-based understanding of solid-oxide electrolysis cells (SOECs) for syngas production by H_2 O/ CO_2 co-electrolysis, *J. Power Sources*. 274 (2015) 768–781.
<https://doi.org/10.1016/j.jpowsour.2014.09.158>.
- [17] A. Perna, M. Minutillo, S.P. Cicconardi, E. Jannelli, S. Scarfogliero, Performance Assessment of Electric Energy Storage (EES) systems based on reversible solid

- oxide cell, *Energy Procedia*. 101 (2016) 1087–1094.
<https://doi.org/10.1016/j.egypro.2016.11.148>.
- [18] J.C. Ruiz-morales, D. Marrero-lopez, J. Canales-Vazquez, J.T.S. Irvine, *Symmetric and reversible solid oxide fuel cells*, 2011.
<https://doi.org/10.1039/c1ra00284h>.
- [19] J. Mermelstein, O. Posdziech, Development and Demonstration of a Novel Reversible SOFC System for Utility and Micro Grid Energy Storage ~, (2017) 562–570. <https://doi.org/10.1002/fuce.201600185>.
- [20] S.M. Haile, Fuel cell materials and components, *Acta Mater.* 51 (2003) 5981–6000. <https://doi.org/10.1016/j.actamat.2003.08.004>.
- [21] M. Morales, J.J. Roa, J. Tartaj, M. Segarra, A review of doped lanthanum gallates as electrolytes for intermediate temperature solid oxides fuel cells: From materials processing to electrical and thermo-mechanical properties, *J. Eur. Ceram. Soc.* 36 (2016) 1–16. <https://doi.org/10.1016/j.jeurceramsoc.2015.09.025>.
- [22] K. Huang, R.S. Tichy, J.B. Goodenough, Superior perovskite oxide-Ion Conductor; Strontium- and magnesium-Doped LaGaO₃: I, Phase Relationships and Electrical properties, *J. Am. Ceram. Soc.* 81 (1998) 2565–2575.
- [23] P. Huang, A. Petric, Superior Oxygen Ion Conductivity of Lanthanum Gallate Doped with Strontium and Magnesium, *J. Electrochem. Soc.* 143 (1996) 1644–1648. <https://doi.org/10.1149/1.1836692>.
- [24] T. Ishihara, H. Matsuda, Y. Takita, Doped LaGaO₃ Perovskite Type Oxide as a New Oxide Ionic Conductor, *J. Am. Chem. Soc.* 116 (1994) 3801–3803.
<https://doi.org/10.1021/ja00088a016>.
- [25] H. Hayashi, H. Inaba, M. Matsuyama, N.G. Lan, M. Dokiya, H. Tagawa,

- Structural consideration on the ionic conductivity of perovskite-type oxides, Solid State Ionics. 122 (1999) 1–15. [https://doi.org/10.1016/S0167-2738\(99\)00066-1](https://doi.org/10.1016/S0167-2738(99)00066-1).
- [26] V. V. Kharton, F.M.B. Marques, A. Atkinson, Transport properties of solid oxide electrolyte ceramics: A brief review, Solid State Ionics. 174 (2004) 135–149. <https://doi.org/10.1016/j.ssi.2004.06.015>.
- [27] Y.C. Wu, M.Z. Lee, Properties and microstructural analysis of $\text{La}_{1-x}\text{Sr}_x\text{Ga}_{1-y}\text{Mg}_y\text{O}_{3-\delta}$ solid electrolyte ceramic, Ceram. Int. 39 (2013) 9331–9341. <https://doi.org/10.1016/j.ceramint.2013.05.050>.
- [28] F. Zheng, R.K. Bordia, L.R. Pederson, Phase constitution in Sr and Mg doped LaGaO_3 system, Mater. Res. Bull. 39 (2004) 141–155. [https://doi.org/10.1016/S0025-5408\(03\)00140-5](https://doi.org/10.1016/S0025-5408(03)00140-5).
- [29] M. Morales, J.J. Roa, J.M. Perez-Falcón, A. Moure, J. Tartaj, F. Espiell, M. Segarra, Correlation between electrical and mechanical properties in $\text{La}_{1-x}\text{Sr}_x\text{Ga}_{1-y}\text{Mg}_y\text{O}_{3-\delta}$ ceramics used as electrolytes for solid oxide fuel cells, J. Power Sources. 246 (2014) 918–925. <https://doi.org/10.1016/j.jpowsour.2013.08.028>.
- [30] K. Huang, M. Feng, J.B. Goodenough, M. Schmerling, SOLID-STATE SCIENCE AND TECHNOLOGY Characterization of Sr-Doped LaMnO_3 and LaCoO_3 as Cathode Materials for a Doped LaGaO_3 Ceramic Fuel Cell, J. Electrochem. Soc. 143 (1996) 3630–3636.
- [31] G. Dotelli, C.M. Mari, R. Ruffo, R. Pelosato, I.N. Sora, Electrical behaviour of LSGM-LSM composite cathode materials, Solid State Ionics. 177 (2006) 1991–1996. <https://doi.org/10.1016/j.ssi.2006.05.033>.
- [32] N. Sakai, T. Horita, H. Yokokawa, K. Yamaji, A. Weber, E. Ivers-Tiffée,

- Electrode Reaction of $\text{La}_{1-x}\text{Sr}_x\text{CoO}_{3-d}$ Cathodes on $\text{La}_{0.8}\text{Sr}_{0.2}\text{Ga}_{0.8}\text{Mg}_{0.2}\text{O}_{3-d}$ Electrolyte in Solid Oxide Fuel Cells, *J. Electrochem. Soc.* 148 (2002) A456.
<https://doi.org/10.1149/1.1362540>.
- [33] K. Yamaji, S. Matsuoka, A. Kawakami, N. Watanabe, N. Sakai, T. Horita, M.E. Brito, A. Ueno, H. Yokokawa, Interface Stability among Solid Oxide Fuel Cell Materials with Perovskite Structures, *J. Electrochem. Soc.* 153 (2006) A621.
<https://doi.org/10.1149/1.2165770>.
- [34] Y. Lin, S.A. Barnett, $\text{La}_{0.9}\text{Sr}_{0.1}\text{Ga}_{0.8}\text{Mg}_{0.2}\text{O}_{3-\delta}$ - $\text{La}_{0.6}\text{Sr}_{0.4}\text{Co}_{0.2}\text{Fe}_{0.8}\text{O}_{3-\delta}$ composite cathodes for intermediate-temperature solid oxide fuel cells, *Solid State Ionics*. 179 (2008) 420–427. <https://doi.org/10.1016/j.ssi.2008.02.063>.
- [35] A.L. Shaula, V. V. Kharton, F.M.B. Marques, Phase interaction and oxygen transport in $\text{La}_{0.8}\text{Sr}_{0.2}\text{Fe}_{0.8}\text{Co}_{0.2}\text{O}_{3-\delta}$ - $(\text{La}_{0.9}\text{Sr}_{0.1})_{0.98}\text{Ga}_{0.8}\text{Mg}_{0.2}\text{O}_{3-\delta}$ composites, *J. Eur. Ceram. Soc.* 24 (2004) 2631–2639.
<https://doi.org/10.1016/j.jeurceramsoc.2003.09.021>.
- [36] R. Ruffo, I.N. Sora, R. Pelosato, G. Dotelli, C.M. Mari, Characterization of $(1-x)\text{La}_{0.83}\text{Sr}_{0.17}\text{Ga}_{0.83}\text{Mg}_{0.17}\text{O}_{2.83-x}\text{La}_{0.8}\text{Sr}_{0.2}\text{MnO}_{3-\delta}$ ($0 \leq x \leq 1$) composite cathodes, *J. Eur. Ceram. Soc.* 25 (2005) 2587–2591.
<https://doi.org/10.1016/j.jeurceramsoc.2005.03.107>.
- [37] T. Shibayama, T. Ishihara, H. Nishiguchi, Y. Takita, Miho Honda, Intermediate Temperature Solid Oxide Fuel Cells Using LaGaO_3 Electrolyte II. Improvement of Oxide Ion Conductivity and Power Density by Doping Fe for Ga Site of LaGaO_3 , *J. Electrochem. Soc.* 147 (2002) 1332. <https://doi.org/10.1149/1.1393358>.
- [38] M. Feng, J.B. Goodenough, K. Huang, C. Milliken, Fuel cells with doped lanthanum gallate electrolyte, *J. Power Sources*. 63 (1996) 47–51.

[https://doi.org/10.1016/S0378-7753\(96\)02441-X](https://doi.org/10.1016/S0378-7753(96)02441-X).

- [39] Z. Wang, H. Wu, Y. She, Y. Dong, B. Yi, M. Cheng, Z. Bi, A High-Performance Anode-Supported SOFC with LDC-LSGM Bilayer Electrolytes, *Electrochem. Solid-State Lett.* 7 (2004) A105. <https://doi.org/10.1149/1.1667016>.
- [40] K. Huang, J.-H. Wan, J.B. Goodenough, Increasing Power Density of LSGM-Based Solid Oxide Fuel Cells Using New Anode Materials, *J. Electrochem. Soc.* 148 (2002) A788. <https://doi.org/10.1149/1.1378289>.
- [41] M. Hrovat, A. Ahmad-Khanlou, Z. Samardzija, J. Holc, Interactions between lanthanum gallate based solid electrolyte and ceria, *Mater. Res. Bull.* 34 (1999) 2027–2034. [https://doi.org/10.1016/S0025-5408\(99\)00220-2](https://doi.org/10.1016/S0025-5408(99)00220-2).
- [42] A. Naoumidis, A. Ahmad-Khanlou, Z. Samardzija, D. Kolar, Chemical interaction and diffusion on interface cathode / electrolyte of SOFC, *J Anal Chem.* 365 (1999) 277–281.
- [43] D. Xu, X. Liu, D. Wang, G. Yi, Y. Gao, D. Zhang, W. Su, Fabrication and characterization of SDC – LSGM composite electrolytes material in IT-SOFCs, *J. Alloys Compd.* 429 (2007) 292–295. <https://doi.org/10.1016/j.jallcom.2006.04.009>.
- [44] S.H. Jo, P. Muralidharan, D.K. Kim, Electrical conductivity studies on the LSGM – CGO composite electrolytes, *J. Alloys Compd.* 491 (2010) 416–419. <https://doi.org/10.1016/j.jallcom.2009.10.207>.
- [45] K.N. Kim, B.K. Kim, J.W. Son, J. Kim, H.W. Lee, J.H. Lee, J. Moon, Characterization of the electrode and electrolyte interfaces of LSGM-based SOFCs, *Solid State Ionics.* 177 (2006) 2155–2158. <https://doi.org/10.1016/j.ssi.2006.02.011>.
- [46] K.N. Kim, H.-W. Lee, J. Moon, J.-W.S.J. Kim, B.-K. Kim, J.-H. Lee, An

- investigation of the interfacial stability between the anode and electrolyte layer of LSGM-based SOFCs, *J. Mater. Sci.* 42 (2007) 1866–1871.
<https://doi.org/10.1007/s10853-006-1315-x>.
- [47] G. Hao, X. Liu, H. Wang, H. Be, L. Pei, W. Su, intermediate-temperature solid oxide fuel cells, *Solid State Ionics*. 225 (2012) 81–84.
<https://doi.org/10.1016/j.ssi.2012.03.005>.
- [48] G. Hao, X. Liu, W. Su, B. Li, S. Liu, H. Wang, Study on GDC-LSGM composite electrolytes for intermediate-temperature solid oxide fuel cells, *Int. J. Hydrogen Energy*. 38 (2013) 11392–11397. <https://doi.org/10.1016/j.ijhydene.2013.06.116>.
- [49] H. Yokokawa, N. Sakai, T. Kawada, M. Dokiya, Thermodynamic stabilities of perovskite oxides for electrodes and other electrochemical materials, *Solid State Ionics*. 52 (1992) 43–56. [https://doi.org/10.1016/0167-2738\(92\)90090-C](https://doi.org/10.1016/0167-2738(92)90090-C).
- [50] H.T. Suzuki, C. Matsunaga, T. Uchikoshi, K. Furuya, F. Munakata, Interaction between A-site deficient $\text{La}_{0.8}\text{Sr}_{0.2}\text{Ga}_{0.8}\text{Mg}_{0.2}\text{O}_{3-\delta}$ (LSGM8282) and $\text{Ce}_{0.9}\text{Gd}_{0.1}\text{O}_{3-\delta}$ (GDC) electrolytes, *Solid State Ionics*. 258 (2014) 18–23.
<https://doi.org/10.1016/j.ssi.2014.01.040>.
- [51] A.N. Ulyanov, N.E. Pismenova, D.S. Yang, V.N. Krivoruchko, G.G. Levchenko, Comment on “Local structure, magnetization and Griffiths phase of self-doped $\text{La}_{1-x}\text{MnO}_{3+\delta}$ manganites,” *J. Alloys Compd.* 602 (2014) 40–41.
<https://doi.org/10.1016/j.jallcom.2014.03.003>.
- [52] A. V. Kovalevsky, A.A. Yaremchenko, S. Populoh, A. Weidenkaff, J.R. Frade, Effect of A-site cation deficiency on the thermoelectric performance of donor-substituted strontium titanate, *J. Phys. Chem. C*. 118 (2014) 4596–4606.
<https://doi.org/10.1021/jp409872e>.

- [53] K. Banerjee, J. Mukhopadhyay, M. Barman, R.N. Basu, Effect of 'A'-site non stoichiometry in strontium doped lanthanum ferrite based solid oxide fuel cell cathodes, *Mater. Res. Bull.* 72 (2015) 306–315.
<https://doi.org/10.1016/j.materresbull.2015.08.002>.
- [54] T. Kawada, N. Sakai, H. Yokokawa, M. Dokiya, I. Anzai, Reaction between solid oxide fuel cell materials, *Solid State Ionics.* 50 (1992) 189–196.
[https://doi.org/10.1016/0167-2738\(92\)90218-E](https://doi.org/10.1016/0167-2738(92)90218-E).
- [55] F. Munakata, M. Tanimura, K. Takamoto, H. Kaneko, H. Yamaguchi, Y. Inoue, Y. Akimune, Effects of La-Deficiency and Substitution of Fe for Co in Solid-State Reaction between $\text{LaCoO}_{3-\delta}$ and Al_2O_3 , *J. Ceram. Soc. Japan.* 103 (1995) 1041–1045.
- [56] H. Yokokawa, T. Horita, N. Sakai, M. Dokiya, T. Kawada, Thermodynamic representation of nonstoichiometric lanthanum manganite, *Solid State Ionics.* 86–88 (1996) 1161–1165.
- [57] J.W. Stevenson, T.R. Armstrong, L.R. Pederson, J. Li, C.A. Lewinsohn, S. Baskaran, Effect of A-site cation nonstoichiometry on the properties of doped lanthanum gallate, *Solid State Ionics.* 113–115 (2002) 571–583.
[https://doi.org/10.1016/s0167-2738\(98\)00324-5](https://doi.org/10.1016/s0167-2738(98)00324-5).
- [58] H. Runge, U. Guth, Influence of A-site deficiencies in the system $\text{La}_{0.9}\text{Sr}_{0.1}\text{Ga}_{0.8}\text{Mg}_{0.2}\text{O}_{3-\delta}$ on structure and electrical conductivity, *J. Solid State Electrochem.* 8 (2004) 272–276. <https://doi.org/10.1007/s10008-003-0438-0>.
- [59] M. Nakamura, K. Nigaki, A. Mineshige, T. Yazawa, M. Kobune, J. Abe, J. Izutsu, S. Fujii, Introduction of A-site deficiency into $\text{La}_{0.6}\text{Sr}_{0.4}\text{Co}_{0.2}\text{Fe}_{0.8}\text{O}_{3-\delta}$ and its effect on structure and conductivity, *Solid State Ionics.* 176 (2005) 1145–

1149. <https://doi.org/10.1016/j.ssi.2004.11.021>.
- [60] K.T. Jacob, S. Jain, V.S. Saji, P.V.K. Srikanth, Thermal expansion of doped lanthanum gallates, *Bull. Mater. Sci.* 33 (2010) 407–411.
<https://doi.org/10.1007/s12034-010-0062-4>.
- [61] J. Meng, H. Fu, S.C. Sun, X.P. Wang, Z.H. Li, D.F. Zhou, G.C. Yang, Nonstoichiometric $(\text{La}_{0.95}\text{Sr}_{0.05})_x\text{Ga}_{0.9}\text{Mg}_{0.1}\text{O}_{3-\delta}$ electrolytes and $\text{Ce}_{0.8}\text{Nd}_{0.2}\text{O}_{1.9-(\text{La}_{0.95}\text{Sr}_{0.05})_x\text{Ga}_{0.9}\text{Mg}_{0.1}\text{O}_{3-\delta}}$ composite electrolytes for solid oxide fuel cells, *Int. J. Hydrogen Energy*. 39 (2013) 1005–1013.
<https://doi.org/10.1016/j.ijhydene.2013.10.096>.
- [62] M. Rozumek, P. Majewski, H. Schluckwerder, F. Aldinger, K. Ku, G. Tomandl, Electrical Conduction Behavior of $\text{La}_{1+x}\text{Sr}_{1-x}\text{Ga}_3\text{O}_{7-\delta}$, *J. Am. Ceram. Soc.* 87 (2004) 1795–1798.
- [63] J.A.M. Van Roosmalen, E.H.P. Cordfunke, A new defect model to describe the oxygen deficiency in perovskite-type oxides, *J. Solid State Chem.* 93 (1991) 212–219. [https://doi.org/10.1016/0022-4596\(91\)90290-X](https://doi.org/10.1016/0022-4596(91)90290-X).
- [64] M.S. Khan, M.S. Islam, D.R. Bates, Dopant Substitution and Ion Migration in the LaGaO_3 -Based Oxygen Ion Conductor, *J. Phys. Chem. B.* 102 (2002) 3099–3104. <https://doi.org/10.1021/jp972819d>.
- [65] X. Zhao, X. Li, N. Xu, K. Huang, Beneficial effects of Mg-excess in $\text{La}_{1-x}\text{Sr}_x\text{Ga}_{1-y}\text{Mg}_{y+z}\text{O}_{3-\delta}$ as solid electrolyte, *Solid State Ionics*. 214 (2012) 56–61.
<https://doi.org/10.1016/j.ssi.2012.02.042>.
- [66] A. Ahmad-Khanlou, F. Tietz, D. Stover, Material properties of $\text{La}_{0.8}\text{Sr}_{0.2}\text{Ga}_{0.9+x}\text{Mg}_{0.1}\text{O}_{3-\delta}$ as a function of Ga content, *Solid State Ionics*. 135 (2000) 543–547.

- [67] M. Stan, T.J. Armstrong, D.P. Butt, T.C. Wallace, Y.S. Park, C.L. Haertling, T. Hartmann, R.J. Hanrahan, Stability of the Perovskite Compounds in the Ce-Ga-O and Pu-Ga-O Systems, *J. Am. Ceram. Soc.* 85 (2004) 2811–2816.
<https://doi.org/10.1111/j.1151-2916.2002.tb00533.x>.
- [68] A. Sinha, B.P. Sharma, P. Gopalan, H. Näge, Study on phase evolution of $\text{GdAl}_{1-x}\text{Ga}_x\text{O}_3$ system, *J. Alloys Compd.* 492 (2010) 325–330.
<https://doi.org/10.1016/j.jallcom.2009.11.086>.
- [69] T. Mori, J. Drennan, J. Lee, J. Li, T. Ikegami, Oxide ionic conductivity and microstructures of Sm³⁺ or La-doped CeO₂-based systems, *Solid State Ionics*. 155 (2002) 461–466.

Chapter 6 | Summary

Pure oxygen is mainly produced by separating oxygen from the air, and its use is diverse, such as the industrial and medical fields. An oxygen separation membrane using a mixed oxide ionic-electronic conductors (MIEC) is an electrochemical device that selectively separates high-purity oxygen via oxide ions using the oxygen partial pressure difference on both sides of the membrane as the driving force. The reaction mechanism consists of (i) adsorption and dissociation of oxygen on the air feed side, (ii) diffusion of oxide ions and back diffusion of electrons in the membrane, and (iii) oxygen association and desorption on the permeate side. In order to improve the oxygen separation efficiency, it is important to increase the surface reaction area in (i) and (iii), and increase the bulk diffusion rate in (ii). In this study, a perovskite-type oxide-based MIEC with a high oxygen permeability was used to produce a multi-layered membrane composed of [porous association layer / dense thin film layer / porous dissociation layer (support substrate)]. As the method for forming the multi-layered structure described above, the electrophoretic deposition (EPD) method, which is a film formation method based on the colloidal chemistry of charged particles in a solvent, was applied. By optimizing various conditions, such as the suspension preparation conditions, EPD conditions, co-sintering conditions, etc., and evaluating the oxygen separation performance of the obtained oxygen separation membranes, the importance of the microstructure design and process selection was discussed. The study contents for each chapter are described as follows:

Chapter 1

The background and purpose of this study was explained. In particular, the applicability of MIEC-based oxygen separation membranes was strongly suggested. The superiority of the electrophoretic deposition process, which is a colloidal process in a solvent was emphasized, as a membrane forming method.

Chapter 2

$\text{Ba}_{0.5}\text{Sr}_{0.5}\text{Co}_{0.8}\text{Fe}_{0.2}\text{O}_{3-\delta}$ (BSCF), which exhibits a high mixed oxide ionic-electronic conduction, was used for the fabrication of an oxygen separation membrane. An asymmetric structure, which was a thin and dense BSCF membrane layer supported on a porous BSCF substrate, was fabricated by the electrophoretic deposition method (EPD). Porous BSCF supports were prepared by the uniaxial pressing method using a powder mixture with BSCF and starch as the pore-forming agent (0-50 wt%). The sintering behaviors of the porous support and the thin layer were separately characterized by dilatometry to determine the co-fired temperature at which cracking did not occur. A crack-free and thin dense membrane layer, which had about a 15- μm thickness and >95% relative density, was obtained after optimizing the processes of EPD and sintering. The dense/porous interface was well-bonded and the oxygen permeation flux was 2.5 ml (STP) $\text{min}^{-1}\text{cm}^{-2}$ at 850 °C.

Chapter 3

A porous layer / dense layer on a porous support was fabricated by sequential electrophoretic deposition. For the co-deposition of two components by EPD, the difference between the two zeta potentials and the concentration ratio of BSCF and

PMMA were investigated as process parameters. Based on the electrophoretic velocity equation, it was clarified that the two components can be uniformly deposited by forming a film under the conditions where the zeta potential is sufficiently high and the difference is as low as possible. As a result, it was shown that a porous layer having a uniform pore distribution can be formed by uniformly depositing and firing two components of BSCF as the base material and PMMA as the pore former. Moreover, it was suggested that an EPD layer with a concentration gradient can be formed by using the difference in the zeta potential. It was also suggested that the porosity of the porous layer can be controlled by changing the concentration ratio of BSCF and PMMA under the conditions when the two components are uniformly deposited.

Chapter 4

Porous (Ba,Sr)(Co,Fe)O_{3-δ} (BSCF) ceramics with a high open porosity and good electrical conductivity were fabricated using Ba_{0.5}Sr_{0.5}Co_{0.8}Fe_{0.2}O_{3-δ} (BSCF), which shows a high mixed ionic-electronic conductivity. In general, during the fabrication of porous ceramics by the sacrificial template method using pore former particles, closed pores are easily formed unless sufficient pore former particles are added. In this study, a novel method was proposed using the gelatinization-retrogradation phenomena of starch for producing a porous body with an excellent percolated pore network structure. By dispersing BSCF and starch in an aqueous slurry (0-50% by weight) and heating, gelatinization of the starch occurred and the starch particles adhered to each other. Furthermore, in order to retain the percolated structure, the water solvent was removed by freeze-drying without heating to obtain a dried green body. The sintering behavior of the porous BSCF bodies prepared under various conditions was characterized by microstructural observations and relative density measurements. By

optimizing the process conditions of the gelatinization and retrogradation, a porous body having an open porosity of 48.3% and with 99% of the total pores open was obtained. The matrix was also well connected and showed a sufficiently high conductivity which was similar to the porous bodies made by the traditional sacrificial template method.

Chapter 5

A series of Sr-ion deficient perovskites, $\text{La}_{0.8}\text{Sr}_{0.2-x}\text{Ga}_{0.8}\text{Mg}_{0.2}\text{O}_{2.8-\delta}$ (LSGM8282, $x=0.00, 0.05, 0.10, 0.15, 0.20$), was synthesized by a conventional solid state reaction method and their electric conductivity and chemical reactivity with Gd-doped ceria were investigated. Reactivity tests between the LSGMs and $\text{Ce}_{0.9}\text{Gd}_{0.1}\text{O}_{2-\delta}$ (GDC) were carried out by X-ray diffraction (XRD), SEM-EDS and electric conductivity measurements. The Sr-ion deficient LSGMs have a lower reactivity against the formation of the high-resistivity phases than the stoichiometric ($x=0.00$) LSGM. The reaction layer formed at the interface of LSGM and GDC during the sintering process due to the mutual diffusion of the cations was classified into five layers depending on the composition. The introduction of the Sr-ion deficient LSGM suppressed the formation of the highly-resistive Sr-rich ($\text{La}_{1+x}\text{Sr}_{1-x}\text{Ga}_3\text{O}_{7-\delta}$) phase. It was suggested that the Sr-ion deficient LSGM ($\text{La}_{0.8}\text{Sr}_{0.2-x}\text{Ga}_{0.8}\text{Mg}_{0.2}\text{O}_{2.8-\delta}$) of $x=0.15$ was the best composition for suppressing the reaction with the GDC interlayer while retaining a relatively good electric conductivity.

Appendix

Publications:

1. Kento Ishii, Chika Matsunaga, Fumio Munakata, Tetsuo Uchikoshi : "Effect of A-site ion nonstoichiometry on the chemical stability and electric conductivity of strontium and magnesium-doped lanthanum gallate", Journal of the American Ceramic Society, Vol.103, pp. 790–799 (2020)
2. Kento Ishii, Chika Matsunaga, Kiyoshi Kobayashi, Adam J. Stevenson, Caroline Tardivat, Tetsuo Uchikoshi : "Fabrication of BSCF-based mixed ionic-electronic conducting membrane by electrophoretic deposition for oxygen separation application" Journal of European Ceramic Society, Vol.39, pp. 5292–5297 (2019)
3. Kento Ishii, Makoto Shimizu, Haruki Sameshima, Takamasa Ishigaki, Sadaki Samitsu, Tetsuo Uchikoshi. Fabrication of Porous (Ba,Sr)(Co,Fe)O_{3-δ} (BSCF) Ceramics using Gelatinization and Retrogradation Phenomena of Starch as Pore-Forming Agent. Ceramics International (accepted, DOI: 10.1016/j.ceramint.2020.02.075)

Presentations at international conferences:

1. Kento Ishii, Chika Matsunaga, Adam J. Stevenson, Caroline Tardivat, Tetsuo Uchikoshi, 「Fabrication and Characterization of BSCF-based Mixed Ionic-Electronic Conducting (MIEC) Membrane by Electrophoretic Deposition (EPD)」, 『The 6th Int'l Conf. on the Characterization and Control of Interfaces for High Quality Advanced Materials and the 54th Summer Symposium on Powder Technology (ICCCI 2018)』, P-B-16, Poster, Kurashiki, Japan (July, 2018)
2. Kento Ishii, Chika Matsunaga, Adam J. Stevenson, Caroline Tardivat, Tetsuo Uchikoshi, 「Oxygen Separation Performance of Asymmetric membrane based on Ba_{0.5}Sr_{0.5}Co_{0.8}Fe_{0.2}O_{3-δ} prepared by Sequential Electrophoretic Deposition Process (EPD)」, 『The 11th International Conference on the Science and Technology for Advanced Ceramics (STAC-11)』, 1P-07, Poster, Tsukuba, Japan (July, 2019)
3. Kento Ishii, Chika Matsunaga, Adam J. Stevenson, Caroline Tardivat, Tetsuo Uchikoshi, 「Fabrication of Oxygen Separation Membrane Based on Mixed Ionic-Electronic conductor and Its Air Separation Property」, 『The 13th Pacific Rim

Conference of Ceramic Societies (PACRIM13)』, 28-P-S11-23, Poster, Tsukuba, Japan (October, 2019)

4. Tetsuo Uchikoshi, Kento Ishii, Adam J. Stevenson, Caroline Tardivat,
「Oxygen Separation from air using BSCF-based dense/porous asymmetric membrane fabricated by electrophoretic deposition process」, 『The 9th International Workshop on Advanced Materials Science and Nanotechnology (IWAMSN 2018)』, AWC-O11, Oral, Ninh Binh, Vietnam (November, 2018)

5. Tetsuo Uchikoshi, Kento Ishii, Adam J. Stevenson, Caroline Tardivat,
「Oxygen Separation from air using BSCF-based Mixed Conductor Membrane」, 『2nd Global Forum on Advanced Materials and Technologies for Sustainable Development (GFMAT-2)』, GFMAT-077-2019, Oral, Toronto, Canada (July, 2019)

Presentation at domestic conferences:

1. 石井健斗、松永知佳、Adam J. Stevenson、Caroline Tardivat、打越哲郎
「EPD 法による BSCF 系混合伝導体膜の作製」、『公益社団法人 日本セラミックス協会 第 30 回秋季シンポジウム』、1PJ04、兵庫県、2017 年 9 月(ポスター)

2. 石井健斗、松永知佳、Adam J. Stevenson、Caroline Tardivat、打越哲郎
「Preparation of BSCF-based Mixed Ionic-Electronic Conducting (MIEC) Membrane by Electrophoretic Deposition (EPD)」、『公益社団法人 日本セラミックス協会基礎科学部会 第 56 回セラミックス基礎化学討論会』、2B19、茨城県、2018 年 1 月(口頭発表)

3. 石井健斗、松永知佳、Adam J. Stevenson、Caroline Tardivat、打越哲郎
「電気泳動堆積法(EPD)による BSCF 系混合伝導体を用いた酸素分離膜の作製と酸素透過性の評価」、『公益社団法人 日本セラミックス協会 2018 年年会』、1P220、宮城県、2018 年 3 月(ポスター)

4. 石井健斗、清水真琴、石垣隆正、打越哲郎、”澱粉の糊化-老化現象を利用した Ba-Sr-Co-Fe-O 系多孔質セラミックスの作製”,第 56 回紛体に関する討論会(静岡県、2018 年 9 月)(口頭発表、査読無)

5. 石井健斗、松永知佳、Adam J. Stevenson、Caroline Tardivat、打越哲郎、”電気泳動堆積法によるセラミックス複合膜の微構造制御”,一般社団法人未踏科学技術協会 第 28 回イン

テリジェント・ナノ材料シンポジウム (東京女子医科大学、2019 年 1 月)(口頭発表)

6. 石井健斗、松永知佳、Adam J. Stevenson、Caroline Tardivat、打越哲郎, “逐次電気泳動堆積法(EPD)による BSCF 系混合伝導体を用いた酸素分離積層膜の作製と微構造制御”, 公益社団法人 日本セラミックス協会基礎科学部会 第 57 回セラミックス基礎化学討論会, (仙台国際センター、2019 年 1 月)(口頭発表)

7. 打越哲郎, 石井健斗, “セラミックス粒子の電気泳動堆積法と酸素分離膜作製への応用”, 一般社団法人 日本粉体工業技術協会 国際粉体工業展東 2018 POWTEX TOKYO 2018 (東京ビックサイト、2018 年 11 月) 3-4 (ポスター)

Awards:

1. ポスター発表「Oxygen Separation Performance of Asymmetric membrane based on $\text{Ba}_{0.5}\text{Sr}_{0.5}\text{Co}_{0.8}\text{Fe}_{0.2}\text{O}_{3-\delta}$ prepared by Sequential Electrophoretic Deposition Process (EPD)」により, The 11th International Conference on the Science and Technology for Advanced Ceramics (STAC-11)において「Silver Poster Award」を受賞。2019 年 7 月 9 日

2. ポスター発表「酸化物イオン-電子混合伝導体を用いた酸素分離膜に関する研究」により, 先進セラミックス研究会若手セミナー2019 において「最優秀ポスター賞」を受賞。2019 年 9 月 12 日

Patent:

1. 多孔質セラミックス焼結体、その製造方法およびそれを用いた用途, 特願 2018-092691 出願中, 発明者:石井健斗, 打越哲郎, 他 1 名

Acknowledgments

First of all, I would like to express my sincere gratitude to my supervisor, Professor Tetsuo Uchikoshi, for his encouragement, extensive discussions, and broad mind.

I would like to thank the thesis committee members, Professor Kiyoharu Tadanaga, Professor Toshihiro Shimada, Associate Professor Makoto Wakeshima, and Professor Takashi Takeda for their valuable comments on my PhD work.

Most of the experiments in this thesis were performed at the National Institute for Materials Science (NIMS) under NIMS-Hokkaido University Joint Graduate Program. I sincerely thank all of the NIMS staff concerned, especially the members of the Fine Particles Engineering group of NIMS for giving me many chances for various experiments.

I would like to give my special thanks to Dr. Tohru S. Suzuki (NIMS), Dr. Kiyoshi Kobayashi (NIMS), Dr. Naoto Shirahata (NIMS), Dr. Hiroyo Segawa (NIMS), Dr. Sadaki Samitsu (NIMS), Dr. Chenning Zhang (NIMS), Dr. Thi Kin Ngan Nguyen (NIMS), Dr. Shota Azuma (NIMS), Dr. Hideo Okuyama (NIMS), Dr. Chika Matsunaga (National Institute of Advanced Industrial Science and Technology), Prof. Fumio Munakata (Tokyo City University) and Dr. Harue T. Suzuki (Tokyo Environmental Public Service Corporation), Prof. Takamasa Ishigaki (Hosei University).

I would like to thank the secretary, Ms. Yoko Watanabe, for supporting my student life at NIMS.

I would like to thank the engineers, Mr. Masahiko Kawasaki and Ms. Chiho Togashi, for their technical support in material processing.

I am grateful to the collaborators of Saint-Gobain, Dr. Adam J. Stevenson, Ms. Caroline Tardivat, and Mr. David Lechevalier, for their helpful discussions.

I would like to thank Makoto Shimizu and Haruki Sameshima of Hosei University, and other many members of the lab for their encouragement.

Finally, I would like to give the biggest thanks go to my family for their understanding and support.

March, 2020

Kento Ishii

謝辞

本研究は、北海道大学・NIMS 連携大学院制度により国立研究開発法人物質・材料研究機構における研究で得られた成果をまとめたものです。本博士論文研究の遂行にあたり、3 年間多大なご指導ご鞭撻を賜りました北海道大学総合化学院客員教授 兼国立研究開発法人物質・材料研究機構 機能性材料研究拠点 微粒子工学グループ、グループリーダーの打越哲郎教授に深く感謝申し上げます。また、本論文をまとめるにあたり、有益な御助言ならびにご指導賜りました北海道大学総合化学院・忠永清治教授、島田敏宏教授、分島亮准教授、武田隆史客員教授に厚く感謝申し上げます。本研究に関する数々のご教授賜りました物質・材料研究機構・鈴木達博士、小林清博士、白幡直人博士、瀬川浩代博士、佐光貞樹博士、ZHANG Chenning 博士、NGUYEN Thi Kin Ngan 博士、東翔太博士、奥山秀男博士、産業技術総合研究所・松永知佳博士、東京都市大学理工学部・宗像文男教授、東京都環境公社・鈴木晴絵博士、法政大学生命科学部・石垣隆正教授に厚く御礼申し上げます。本研究を進めるにあたりサンゴバン社、Adam J. Stevenson 博士, Caroline Tardivat 氏, David Lechevalier 氏から多くの御助言賜りましたこと厚く御礼申し上げます。また、機構内の皆様から多くの御助言ならびにご協力賜りましたこと厚く御礼申し上げます。NIMS での学生生活を支えて頂いた事務業務員・渡邊洋子氏に感謝申し上げます。材料加工の技術支援をして頂いたエンジニア・川崎昌彦氏、富樫千穂氏に感謝申し上げます。本研究で苦楽を共にした、清水真琴氏、鮫嶋晴生氏をはじめ、励まし合った学生の皆様に感謝の意を表します。

最後に、本学で学ぶ機会を与えて頂くとともに、常に暖かく励まし応援して下さいった家族に、この場を借りて深謝の意を表します。

令和 2 年 3 月

石井 健斗